technische universität
dortmund

Application of Machine Learning in Glow Curve Deconvolution

Dissertation

zur Erlangung des akademischen Grades

doctor rerum naturalium
(Dr. rer. nat.)

vorgelegt von

Evelin Lienau (geb. Derugin)
geboren in Orenburg

Fakultät Physik
Technischen Universität Dortmund
2023

Diese Dissertation wurde der Fakultät Physik der Technischen Universität Dortmund zur Erlangung des akademischen Grades eines Doktors der Naturwissenschaften vorgelegt.

1. Gutachter:	Prof. Dr. Kevin Kröninger
2. Gutachter:	Prof. Dr. Carsten Westphal
Prüfungsvorsitz:	Jun.-Prof. Dr. Armin Lühr
Prüfungsbeisitz:	Dr. Bärbel Siegmann
Abgabedatum der Dissertation:	20.06.2023
Datum der mündlichen Prüfung:	24.08.2023

Abstract

Routine dosimetry aims to estimate the radiation dose of occupationally exposed persons for a monitoring interval of one month. The Material Prüfungsamt NRW (MPA NRW) provides a thermoluminescence (TL) dosimeter based on LiF:Mg,Ti (TL-DOS). Thermal fading causes a time-dependent signal loss when using a TL dosimeter. This signal change is used to gain information about the irradiation event beyond the dose estimate, which can help to improve the radiation protection concept of occupationally exposed persons.

In this work, multivariate analysis techniques for glow curve analysis using deep learning approaches are developed to estimate the irradiation day within a monitoring interval of 40 days with single-dose irradiation using a Cs-137 source with a prediction uncertainty of two days.

To create a data basis for training the application of deep learning, over 10 000 measurements were performed in cooperation with the MPA NRW and the TL-DOS project. Furthermore, a technique to generate realistic glow curves based on generative adversarial networks (GANs) is presented, which makes it possible to expand the measured data set artificially and thus create a larger database for the deep learning approaches.

Kurzfassung

Das Ziel der Routinedosimetrie ist die Abschätzung der Strahlendosis von beruflich strahlenexponierten Personen für ein Überwachungsintervall von einem Monat. Das Materialprüfungsamt NRW (MPA NRW) verwendet ein Thermolumineszenz (TL)-Dosimeter auf der Basis von LiF:Mg,Ti (TL-DOS). Beim Einsatz eines TL-Dosimeters kommt es durch thermisches Fading zu einem zeitabhängigen Signalverlust. Diese Signaländerung wird genutzt, um über die Dosisabschätzung hinaus Informationen über das Bestrahlungsereignis zu gewinnen, die dazu beitragen können, das Strahlenschutzkonzept für beruflich strahlenexponierte Personen zu verbessern.

In dieser Arbeit werden multivariate Analyseverfahren für die Glühkurvenanalyse unter Verwendung von Deep-Learning-Ansätzen entwickelt, um den Bestrahlungstag innerhalb eines Überwachungsintervalls von 40 Tagen bei Einzeldosisbestrahlungen mit einer Cs-137-Quelle mit einer Vorhersageunsicherheit von zwei Tagen abzuschätzen.

Um eine Datenbasis für das Training eines Deep-Learning-Ansatzes zu schaffen, wurden über 10 000 Messungen in Zusammenarbeit mit dem MPA NRW und dem TL-DOS Projekt durchgeführt. Darüber hinaus wird ein Verfahren zur Generation realistischer Glühkurven auf Basis generative adversarial networks (GANs) vorgestellt, das es ermöglicht, den gemessenen Datensatz künstlich zu erweitern und damit eine größere Datengrundlage für die Deep-Learning-Ansätze zu schaffen.

Publications

1. E. Derugin, K. Kröninger, F. Mentzel, O. Nackenhorst, J. Walbersloh, and J. Weingarten, **Deep TL: progress of a machine learning aided personal dose monitoring system**, *Radiation Protection Dosimetry*, Volume 199, Issue 8-9, June 2023, Pages 767–774

2. F. Mentzel, E. Derugin, H. Jansen, K. Kröninger, O. Nackenhorst, J. Walbersloh, and J. Weingarten **No more glowing in the dark: how deep learning improves exposure date estimation in thermoluminescence dosimetry**, *Journal of Radiological Protection*, 41 S506 (2021)

Conference Contributions

1. E. Derugin, K. Kröninger, F. Mentzel, O. Nackenhorst J. Walbersloh, and J. Weingarten, **Thermoluminescence glow curve generation using generative adversarial networks (GANs)**, DPG Spring Meeting 2023, Dresden, DE (talk)

2. E. Derugin, K. Kröninger, F. Mentzel, O. Nackenhorst J. Walbersloh, and J. Weingarten **Der „rAIdiation protection co-pilot": Ein Machine Learning unterstütztes Bestrahlungsszenario-Vorhersage-Tool**, 53. FS Jahrestagung 2022, Konstanz, DE (talk)

3. E. Derugin, K. Kröninger, F. Mentzel, O. Nackenhorst J. Walbersloh, and J. Weingarten, **rAIdiation protection co-pilot: A Machine Learning aided radiation scenario prediction tool**, 64th Annual Meeting & Exhibition AAPM 2022, Washington, DC, USA (poster)

4. E. Derugin, K. Kröninger, F. Mentzel, O. Nackenhorst J. Walbersloh, and J. Weingarten, **Deep TL: progress of a machine learning aided personal dose monitoring system**, 6th European Congress on Radiation Protection 2022, Budapest, HU (poster)

5. E. Derugin, **Analye von TLD-Dosimetern mittels neuronaler Netzwerke**, LPS: 22. Sommerschule im Strahlenschutz 2022, Berlin, DE (talk)

6. E. Derugin, K. Kröninger, F. Mentzel, O. Nackenhorst J. Walbersloh, and J. Weingarten, **Entwicklung eines „rAIdiation protection co pilot's"**, 95. AKD Sitzung, Peine, DE (talk)

7. E. Derugin, K. Kröninger, F. Mentzel, J. Walbersloh, and J. Weingarten, **Improving information extracted from glow curves of thermoluminescence personal dosemeters using CNNs**, DPG Spring Meeting 2021, online (talk)

8. E. Derugin, H. Jansen, K. Kröninger, F. Mentzel, O. Nackenhorst, J. Walbersloh, and J. Weingarten, **Improving the analysis of TL dosimeter with convolutional neural networks**, Joint Conference of the ÖGMP, DGMP and SGSMP 2021, online (talk)

9. E. Derugin, H. Jansen, K. Kröninger, M. Rempe, J. Walbersloh, and J. Weingarten, **Erweiterung der für die Überwachung der Personendosis relevanten Informationen aus den Glühkurven von Thermolumineszenzdosimetern unter Verwendung generativer neuronaler Netze**, 51. Jahrestagung der DGMP 2020, online (poster)

Supervised and Co-Supervised Theses

1. N. Dönmez, **Entwicklung einer Sonde zur Bestimmung der Detektortemperatur von TL-DOS Dosimetern beim Auslesen**, Bachelor Thesis, 2020

2. M. Maiworm, **Charakterisierung eines optischen Spektrometers**, Bachelor Thesis, 2020

3. A. Fischer, **Statistical comparison of measured and machine learning-generated thermoluminescence glow curves**, Bachelor Thesis, 2021

4. S. Cevic, **Untersuchung des TL Emissionsspektrums in Abhängigkeit der Fadingzeit**, Bachelor Thesis, 2021

5. M. Özdemir, **Studie zur Kalibrierung von TL-DOS Detektoren im Auslesemagazin**, Bachelor Thesis, 2022

6. T. Cremer, **Vorhersage des Bestrahlungstages von TL-DOS Detektoren mittels LSTM's**, Bachelor Thesis, 2022

7. H. Jansen, **Studies on irradiation date estimation using measured and simulated high-statistics glow curve data sets**, Master Thesis, 2020

8. A. Schneider, **Glowcurve simulation using rate equations**, Master Thesis, 2021

9. P. Stecher, **Entwicklung eines Aufbaus zur automatisierten Bestrahlungsfeldvermessung am Materialprüfungsamt NRW**, Master Thesis, 2022

Contents

Introduction

> *"There is no safe amount of radiation.*
> *Even small amounts do harm."*

> Linus Pauling [1]

Handling ionising radiation is accepted due to its crucial use in science, medicine and industry. In Germany it is regulated by the Radiation Protection Act (*Strahlenschutzgesetz (StrlSchG)* [2]). Radiation protection measures are required to protect occupationally exposed persons, including official monitoring of the personal dose by wearing an official personal dosimeter on a representative part of the body [3].

Suppose radiation exposure is detected during monitoring due to an increased dose level. In that case, the radiation protection officer shall investigate this event and its circumstances and report it to the responsible authorities. Based on this, existing safety measures may need to be revised and improved to prevent future exposure [4]. The use of electronic personal dosimeters (EPDs) [5] with real-time alarms can provide an additional level of safety in the handling of ionising radiation. However, direct-display EPDs are not approved as official dose monitors in pulsed radiation fields, such as accelerators, under the StrlSchG [6, 7]. Accordingly, only passive dosimeter technologies that do not provide real-time information to the user are approved for official dose monitoring. These include dosimeters based on films [8], optically stimulated luminescence (OSL) [9] or thermoluminescence (TL) [10], which is the most relevant dosimeter type for this thesis.

Robert Boyle first reported the phenomenon of TL in the mid-17$^{\text{th}}$ century by heating a diamond. Since then, more and more materials have been discovered that exhibit this effect. However, it took a long time before a theoretical description of this phenomenon existed. In 1945, Randall and Wilkins presented the first theory describing the TL effect [11]. The first TL-based dosimeters for measuring the radiation dose were developed in the following years. Since then, TL dosimeters have been used in various areas of dosimetry, including personal and environmental dosimetry. For example, in recent years, the *Material Prüfungsamt Nordrhein-Westfalen (MPA NRW)* has developed a new type of TL personal dosimeter system, called *TL-DOS*, in cooperation with *Kröninger Group at the TU Dortmund University*. The MPA NRW is one of four official personal dose

measurement centres in Germany and monitors up to 120 000 occupationally exposed persons in Germany every month [12].

A TL dosimeter can be considered an all-rounder, as it can be used in radiation fields of both photons and neutrons. Therefore, it is used not only as a whole-body dosimeter but also as a partial or albedo dosimeter. During the development process, several studies and theses (Bachelor, Master and PhD degrees) were performed in cooperation with the MPA NRW and Kröninger Group, investigating the versatile fields of application of the TL-DOS dosimeters. Among them, studies on the influence of thermal stimulation on the TL signal were performed, which showed that although this causes a loss of information on the TL signal, it can still be used to gain additional information about the irradiation event, especially the time of irradiation [13, 14, 15, 16].

The main goal of this thesis is to determine the irradiation day of a TL-DOS dosimeter. For this purpose, multivariate analysis techniques for the deconvolution of the TL signal are developed using machine learning, particularly deep learning. Glow curves (GCs) represent the measured photons as a function of the readout time. They are analysed for their signal change as a function of the time between the preparation of a dosimeter for use and the irradiation time. Since deep learning applications require high statistic data sets, deep learning is also used for generating artificial glow curves in order to be able to study a variety of irradiation scenarios.

This thesis is structured as follows. Chapter 2 introduces the basic concepts of TL dosimetry and the TL-DOS project, which serves as the base for performing this study. Chapter 3 provides a detailed description of the study conducted. The underlying steps and details that motivated the selection of the machine learning approaches are presented. The series of measurements performed in this project's context and the data preparation are presented in Chapter 4. Subsequently, these datasets are used to estimate the irradiation day using machine learning in Chapter 5. The basics of Machine Learning, particularly fully connected Deep Neural Networks (DNN) and Convolutional Neural Networks (CNN), are explained, and the development and training of the models for radiation day estimation are described. Furthermore, the interpretability of the chosen models is analysed and discussed. In Chapter 6, glow curves are generated using generative neural networks and tested for their applicability as training data for irradiation day estimation. Chapter 7 concludes this thesis and summarises the main results. The obtained results are discussed, and their significance for TL dosimetry is highlighted. Furthermore, an outlook on future research work and further developments in the TL-DOS project is given.

Parts of this thesis are already published in Ref. [17, 18].

2   Thermoluminescence Personal Dosimetry

Personal dosimetry is a branch of radiation protection that measures and assesses the amount of ionising radiation to which a person or object has been exposed. Dosimetry ensures that radiation doses are within acceptable limits to prevent adverse health effects. Exposure to limited quantities of ionising radiation is accepted because of its relevance in medical applications, such as imaging and tumour treatment. However, it also poses risks to the people who work with it. The measurement or monitoring of radiation doses to occupationally exposed persons is called personal dosimetry, monitored by one of Germany's personal dose monitoring services.

In Germany, about 420 000 people are monitored for radiation protection, and dosimeters are used in various clinical applications, such as nuclear medicine, radiation therapy or radiology, but also in industry, research and development [19]. Several dosimeter types are used in radiation monitoring, e.g. the thermoluminescence dosimeter (TLD) [20], or optically stimulated luminescence (OSL) [9]. The Materialprüfungsamt NRW is an official personal dose monitoring service in Germany that monitors the dose of about 12 000 companies every month with the novel TLD system thermoluminescence dosimeter system (TL-DOS) [21].

The Radiation Protection Act (Strahlenschutzgesetz (StrlSchG)) [2] is Germany's central legal regulation for personal dosimetry. The measurement of the radiation dose is ensured by using personal dosimeters worn at a representative location on the body, depending on the measurement application. The resulting requirements for personal dosimetry are precisely defined in the StrlSchG and the Radiation Protection Ordinance (Strahlenschutzverordnung (StrlSchV)) [22]. Proper dosimetry practices help to minimise the risk of radiation-induced health effects and ensure that radiation doses are kept as low as reasonably achievable (ALARA).

This chapter aims to provide an understanding of the interaction of radiation with matter, especially the impact of photons and electrons on tissue and the resulting radiation protection quantities. Furthermore, the phenomenon of thermoluminescence (TL) and the novel TL-DOS dosimeter system are presented, including the calibration and measurement procedures of the TL-DOS detectors.
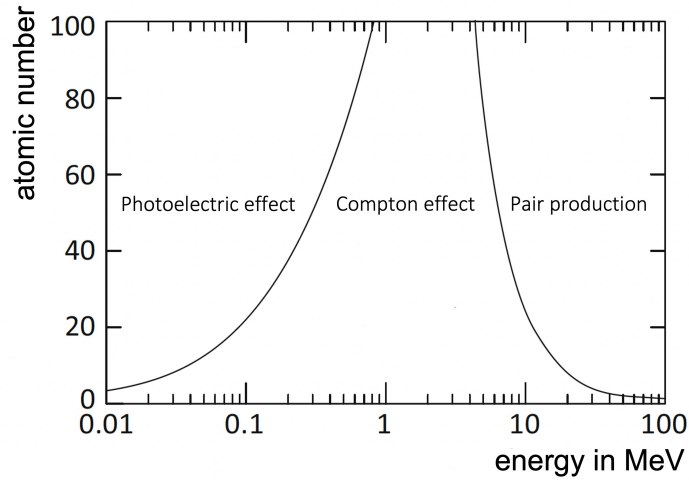
Figure 2.1: Interaction processes for photons as a function of energy and atomic number. Adapted from Ref. [24] with data from Ref. [25].

2.1 Photon Interaction with Matter

Radiation can interact with matter in different ways. A distinction is made between the interaction of electromagnetic radiation (photons) and particle radiation (alpha and beta particles) depending on the respective energy. In the following, reference is made only to the interaction of photons with matter since the dosimeter system used in this work is designed to detect photons.

Depending on the photons' energy and the interaction material's atomic number, the interaction can be described by the photoelectric effect, Compton effect and pair formation. Figure 2.1 depicts the probability of the occurrence of each process. The photoelectric effect dominates in the range of low photon energies up to 1 MeV depending on the atomic number of the medium. The photons transfer the total energy to the atom, resulting in a shell electron emission. The interaction probability for the photoelectric effect falls rapidly with increasing photon energy and increases strongly with the atomic number for fixed photon energy. The photoelectric effect is used in X-ray imaging to better show contrasts due to the different densities of bone and soft tissue. [23]

The Compton effect dominates at photon energies around 0.1 MeV. The incident photon scatters at a shell electron and transfers part of its energy. The figure shows that the interaction probability for the Compton effect is significantly greater for materials with small atomic numbers than those with high atomic numbers. Due to the scattering processes of the Compton effect, a scattered radiation field is created in addition to the primary radiation field, which must be considered when monitoring radiation. Computer

tomography is an application where the Compton effect is dominant, as photons interact with tissue with an atomic number of 7. [23]

Starting from photon energy of 1.022 MeV, the interaction of photons with an electric field can lead to the formation of an electron-positron pair, a phenomenon known as pair production. This particular effect becomes more significant at higher energies exceeding 3 MeV, as depicted in Figure 2.1. [23] However, this effect is mostly neglected due to the energy range considered in this thesis.

2.2 Dosimetric Quantities

Energy is deposited within the material through the interaction of photons with matter. The average energy $\mathrm{d}E$ deposited per mass $\mathrm{d}m$ is referred to as the energy dose D in units of Gray (Gy):

$$D = \frac{\mathrm{d}E}{\mathrm{d}m} \qquad [D] = \mathrm{Gy} = \frac{\mathrm{J}}{\mathrm{kg}} = \frac{\mathrm{m}^2}{\mathrm{s}^2}. \tag{2.1}$$

Since the absorbed dose cannot be measured directly, an additional quantity is defined, referred to as KERMA K ("kinetic energy $\mathrm{d}E_{\mathrm{kin}}$ released per unit mass $\mathrm{d}m$") and which can be measured. This quantity is usually given in a water-equivalent medium, as the human body also consists mainly of water. K can be used as a calibration parameter. The absorbed dose D equals K when a secondary electron equilibrium is reached. [26]

$$K = \frac{\mathrm{d}E_{\mathrm{kin}}}{\mathrm{d}m} \qquad [K] = \mathrm{Gy} \tag{2.2}$$

Radiation protection quantities are defined to consider the biological effects of radiation, irrespective of the type of radiation; see Figure 2.2. These include the equivalent dose H_{T}:

$$H_{\mathrm{T}} = \sum_R \omega_{\mathrm{R}} D_{\mathrm{T,R}} \qquad [H_{\mathrm{T}}] = \mathrm{Sv} \tag{2.3}$$

where ω_{R} is the radiation-dependent weighting factor and $D_{\mathrm{T,R}}$ the deposited dose within an organ T and the radiation type R. ω_{R} of photons and electron radiation is the same and is therefore set to 1 as a reference. Furthermore, α-radiation, neutrons and heavy ions have a ω_{R} value of up to 20. If the effect of ionising radiation on individual body organs is also considered, each organ can be assigned an individual organ weighting factor ω_{T}, which provides information about the sensitivity of the corresponding organ, e.g. the eye lens has a low weighting factor of 0.04 [27]. In contrast, the lung is more sensitive to ionising radiation with a factor of 0.12. The sum of all organic weighting factors is 1.

The effective dose E is defined as the sum of the product of all equivalent organ doses

and the respective organ weighting factors.

$$E = \sum_T \omega_T H_T \qquad [E] = \text{Sv} \qquad (2.4)$$

This quantity can be used to estimate the radiation risks to human tissue. The radiation exposure of each person from natural radioactivity averages about $2\,\text{mSv}$ per year, although this value can vary depending on the region. In addition, the annual radiation exposure from medical sources, e.g. imaging procedures such as X-rays or computer tomography, can add up to another $2\,\text{mSv}$.
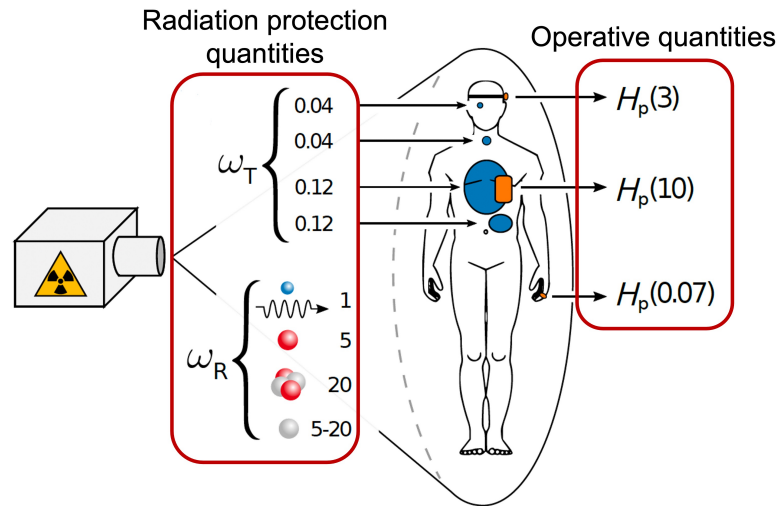
Figure 2.2: Radiation protection quantities and operational quantities, adapted from Ref. [13], Data from Ref. [27]

.

Since the radiation protection quantities cannot be measured directly, but the radiation protection of occupationally exposed persons must be ensured, operational quantities $H_\text{p}(d)$ are introduced, which estimate the effective dose E at a representative position and a depth d in soft tissue using passive dosimeters. It can be divided into whole-body dose measurement and partial-body dose measurement. The whole-body dosimeter is usually worn at chest level and estimates the dose deposited in the human body at a depth of $10\,\text{mm}$, defined as $H_\text{p}(10)$. Partial body dosimeters include finger ring dosimeters, which estimate a skin dose at $3\,\text{mm}$ depth ($H_\text{p}(3)$), and eye lens dosimeters, which estimate a dose at $0.07\,\text{mm}$ ($H_\text{p}(0.07)$). The operative quantities are depicted in Figure 2.2. In the following, reference is made exclusively to the whole-body dose quantity $H_\text{p}(10)$.

2.3 Thermoluminescence

The phenomenon of TL belongs to a subgroup of luminescence and describes the emission of photons after excitation with thermal energy. The emission of TL is always associated with a previous energy deposition caused mainly by ionising irradiation. This effect is used to determine the age of fossils [28] or as a detector material in the field of radiation protection since 1953 [29]. However, not every solid is suitable for TL emission. The primary condition requires metastable energy states within the band gap of an insulator or semiconductor, which are shallow enough to be emptied by excitation using thermal energy.

2.3.1 Band Model

The solid-state band model can be used to explain the principle of the energy deposition and emission of the TL, see Figure 2.3. Several independent atoms next to each other form energy bands with a width depending on the bonding of the electrons to the atom. The topmost occupied electron energy band is called the valence band, while the next higher band with the lowest unoccupied states is called the conduction band.
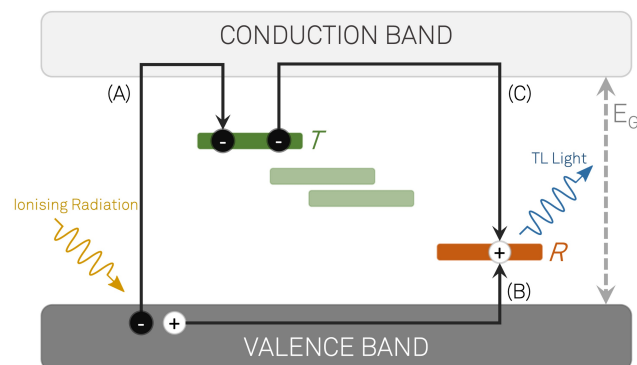
Figure 2.3: Schematic representation of the band structure consisting of the valence band and conduction band separated by the energy band gap E_G; **(A)** & **(B)**: Ionisation and excitation of an electron (black circle)/hole (white circle) and binding by a trap T (green) or recombination centre R (orange); **(C)**: Electron release after thermal excitation, direct recombination with a hole in a recombination centre and emission of TL light.

In the case of insulators or intrinsic semiconductors, a band gap E_G in which no electron states exist separates the valence band and the conduction band. The excitation of an electron from the valence band to the conduction band is only possible if the received energy is higher than the energy of the band gap. Electrons in a filled valence band form strong bonds that are difficult to break between neighbouring atoms. These electrons can not move freely because only two electrons with an opposite spin on one energy level

are allowed and thus cannot contribute to conduction. A considerable amount of energy is required to break the bond between the valence electrons to allow a transition of the valence electrons into the conduction band. The energy gap of LiF:Mg,Ti is $E_G = 13\,\text{eV}$ [30], corresponding to an insulator.

Lithium fluoride (LiF) is a commonly used TL material in routine dosimetry. Doping the LiF with foreign atoms, like magnesium (Mg) and titanium (Ti), leads to the formation of metastable states within the band gap of the LiF.

The interaction of ionising radiation with matter via the photoelectric effect, Compton effect or pair production deposit energy within the TL material [29]. This causes electrons to be excited from the valence band and lifted into the conduction band by leaving a positive charge behind in the valence band, referred to as a *hole*. Electrons and holes move freely in the crystal lattice with a probability of falling back into their initial state, where they can recombine with a hole, which emits photons to the crystal lattice with an energy corresponding to the energy difference of the valence and conduction band. Considering a pure crystal, the electron/hole pair recombination happens instantaneously after excitation, which refers to *radioluminescence*. With this process, no energy is stored in the crystal, meaning no TL can occur.

However, the doped crystal, e.g. LiF doped with Mg and Ti, allows additional localised metastable energy levels within the band gap called traps (green). These traps are located beneath the conduction band at a ΔE distance. Metastable states near the valence band are called recombination centres (orange). Traps or recombination centres can bind excited electrons or holes that do not directly recombine, see steps **(A)** and **(B)** in Figure 2.3. Thermal or optical excitation can extract the localised electrons/holes in the traps/recombination centres. Classifying the metastable state as a trap or recombination centre depends on the relative probabilities of thermal excitation and recombination. Assuming that the transition of an electron from a trap into the conduction band is more probable than lifting a hole from the valence band into a trap, then the state can be classified as a trap and vice versa as a recombination centre.

The trapped electrons are elevated into the conduction band by supplying additional thermal energy higher than the trap's binding energy to the crystal. Due to the different traps and, thus, the different energies of the traps, different thermal energies are required to release the electrons. The Boltzmann distribution determines the probability p to release an electron from a trap with a specific energy ΔE, which depends on the temperature T:

$$p = \tau^{-1} = \exp\left(-\frac{\Delta E}{k_B T}\right), \tag{2.5}$$

k_B is the Boltzmann constant and τ the mean half-life time of the trap. In addition,

the coefficient p is defined as the probability of releasing electrons in a unit of time. Higher temperatures can release more electrons from deeper traps. Nevertheless, also the mean lifetime τ gets shortened. The released electron can recombine directly with a trapped hole, see step **(C)** in Figure 2.3, resulting in the emission of photons and thus to TL light. The emitted photons can be counted and plotted as a function of the measurement time, resulting in a so-called TL Glow Curve (GC), see Figure 2.4. The number of emitted photons is proportional to the deposited dose of the ionising irradiation and, therefore, can be used in personal dosimetry for dose estimation. The GC's shape depends on the TL material and the heating temperature. According to equation 2.5, each trap has a different lifetime depending on its trap energy and the thermal energy applied to the material. Peaks four and five are the most persistent, e.g. peak 5 has a half-life of approximately 80 years and peak 4 of 8 years if the material is stored at room temperature [20].

2.3.2 Glow Curve and Thermal Fading

The TL GC is essential for determining the radiation dose. Therefore, the emitted photons are detected using a photomultiplier and plotted as a function of the measurement time. A typical GC of photon irradiation of LiF:Mg,Ti is shown in Figure 2.4.
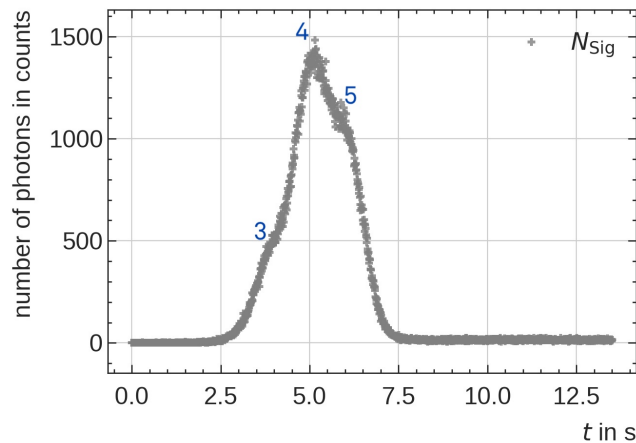
Figure 2.4: Exemplary pre-tempered glow curve in time-space with characteristic glow curve peaks 3, 4 and 5.

Several peaks generally characterise the GC, each approximated by a complex model function depending on the material and the thermal heating; for more detail, see Reference [13]. The GC is measured by heating the TL material exponentially at approximately $380\,°\mathrm{C}$ ($653\,\mathrm{K}$) or even higher, e.g. for neutron dosimetry. A GC of LiF:Mg,Ti consists of five peaks when irradiated with photons. However, because of the short distance between the location of the first trap and the conduction band, a room

temperature of $19\,°C$ $(292\,K)$ is sufficient to empty the first trap, which is referred to as the *post-irradiation fading effect* or just *thermal fading.* The second peak is eliminated due additional pre-heating step during the read-out measurement. Therefore the first and second peak is not shown in the GC.

Thus, the shape of the GC depends on the temperature to which the material is exposed and on the time that has elapsed between the excitation of the material and the read-out of the TL signal, which can be used to characterise the irradiation event better. The impact of the thermal fading effect is significant for the dose estimation. The material is pre-heated at a specific temperature to overcome the thermal fading, eliminating unstable peaks like peaks one and two. Only the stable long-life peaks remain. However, eliminating the unstable peaks leads to losing part of the signal, making it difficult to reconstruct the day of excitation. Nevertheless, there are differences in the pre-heated GCs, as early heating also lifts electrons from lower traps to higher ones, where they are recaptured.
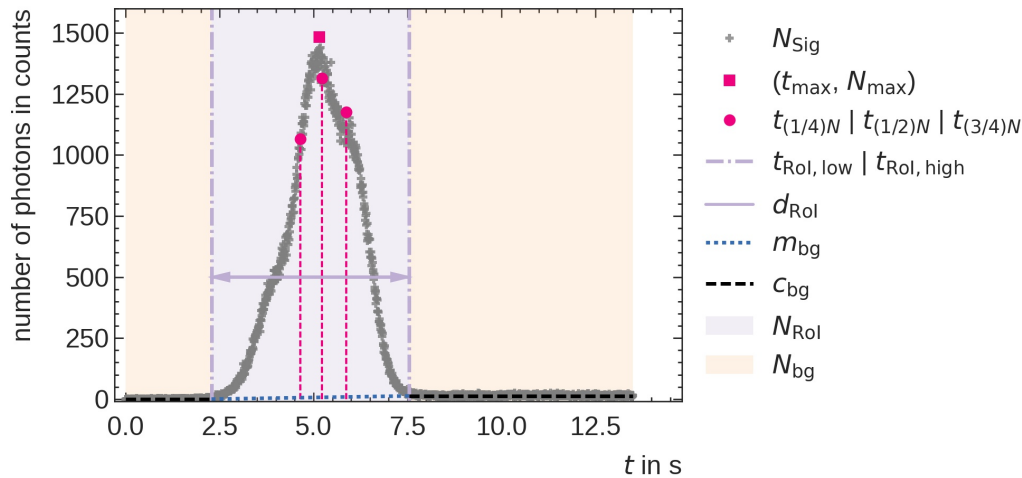
2.3.3 Glow Curve Parameters

The shape of the GC is characteristic depending on the irradiation scenario. Due to thermal fading, the shape changes depending on the time after the irradiation event. The shape of the GC allows for the derivation of multiple parameters, providing information besides the deposited dose within the material.

The photon counts N_{RoI} within a region of interest (RoI) are used to determine the deposited dose and photon counts outside the RoI are assigned to the background noise N_{bg}. The background is approximated using a linear function with m_{bg} as the slope of the function and c_{bg} as the averaged background photon counts. [17]

The RoI is limited by $t_{\mathrm{RoI,\ low}}$ and $t_{\mathrm{RoI,\ high}}$. These limits describe when the relevant TL signal begins and ends, whereas the distance between these two boundaries defines the duration of the RoI. N_{mean} and N_{tot} represent the GC's average and total photon number. The maximum of the GC N_{max} is reached after the time t_{max}. The signal within the RoI can be divided into quartiles $t_{1/4\mathrm{N}}$, $t_{1/2\mathrm{N}}$ and $t_{3/4\mathrm{N}}$. [17]

All parameters are depicted in Figure 2.5. These GC parameters will be used in this project to predict the irradiation day based on the time dependencies of the parameters. For this purpose, correlations between the individual parameters are analysed as a function of the irradiation day and learned to distinguish using ML.

Figure 2.5: Extracted glow curve parameters in time-space. Reproduced from Ref. [17].

2.4 The TL-DOS Project

The TL-DOS project is a dosimeter system newly developed by the Materialprüfungsamt Nordrhein-Westfalen (MPA NRW) in cooperation with the TU-Dortmund University for whole-body dose monitoring. The TL-DOS detector uses the TL principle for dose detection. Lithium fluoride doped with Magnesium and Titanium (LiF:Mg, Ti) is deposited as a thin layer, forming the sensitive detector material. The following section describes the design of the TL-DOS detector and the corresponding read-out apparatus.

2.4.1 The TL-DOS Detector and Dosimeter Design

The schematic structure of the detector is shown in Figure 2.6 and consists of two components, a thin layer component and a base component. The sensitive LiF:Mg,Ti layer is sintered onto an aluminium carrier plate. The carrier plate is connected to the base frame with an engraved code for identification. A data matrix is located on the underside of the detector for identification during the read-out process. [31]

The TL-DOS personal dosimeter, shown in Figure 2.7, is a whole-body dosimeter for the determination of the personal dose $H_\mathrm{p}(10)$ of photon radiation, according to § 66 para. 1 StrlSchV [22]. The dosimeter probe consists of a cassette, a protective and filter material for the detectors. The cassette contains a blister pack with two TL-DOS detectors. The packaging of the detectors enables safe and correct placement of the detectors in the cassette and protects the detectors from external influences. The TL-DOS dosimeter is approved for a monitoring period of 1 month up to 6 months. [32]
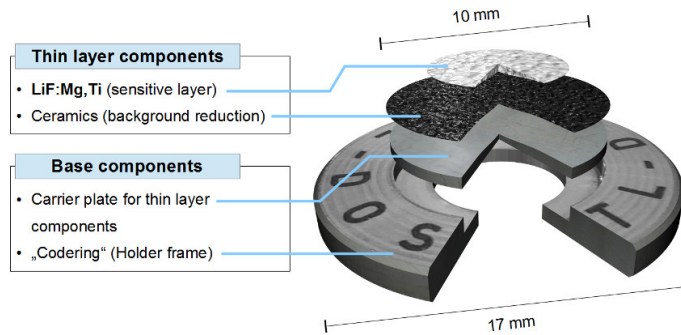
Figure 2.6: Schematic of the TL-DOS detector components, consisting of base components and the thin layer detector material. Adapted from Ref. [14].


Figure 2.7: TL-DOS cassette with two blistered TL-DOS detectors to measure the irradiation quantities $H_p(10)$ and $H_p(0.07)$ (Image courtesy: MPA NRW).

2.4.2 TL-DOS Routine Cycle

In addition to the high sensitivity of the LiF to ionising radiation, the reusability is another advantage of the TL-DOS system. The TL-DOS detector goes through a recurring cycle to be used repeatedly in routine dosimetry (see Figure 2.8). In preparation for use by the radiation-monitored person, the detector is exponentially heated at 663 K for 9 seconds and then rapidly cooled to eliminate any possible residual signal on the detector.

After the detector regeneration, it is paired with another detector. After both detectors are packed in a blister, they can be assigned to a monitoring person who carries the dosimeter cassette for one month. At the end of the monitoring period, the blister is removed from the cassette and returned to the monitoring service. It is unpacked from the blister and evaluated in the designated readout device. The detector passes through 3 stations in the readout device. First, the detector is preheated at 427 K to eliminate thermal fading. Then it is exponentially heated at 653 K for 14 seconds at the readout

station, and the resulting TL signal is detected with a photomultiplier and saved in the system. The resulting TL GC is used to estimate the exposure dose. The last station in the readout corresponds to the first step in the routine cycle. The detector is heated for 9 seconds at $663\,\text{K}$ to eliminate the residual signal and is ready for the next monitoring step.
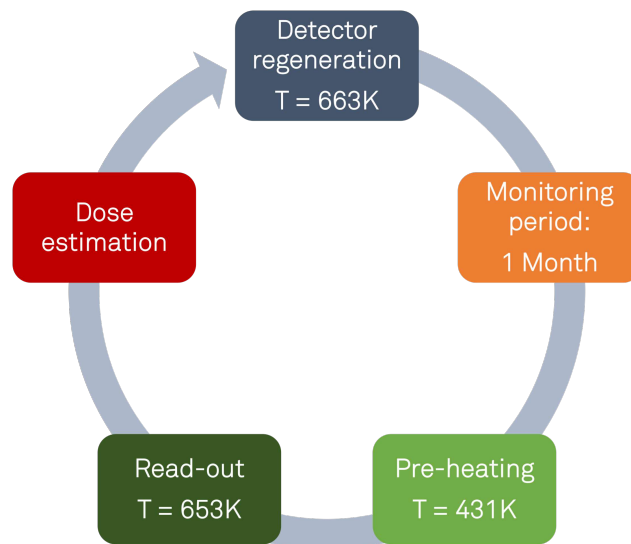
Figure 2.8: Typical cycle of a TL-DOS detector in a routine operation.

During routine operations, it is standard practice to calibrate each individual detector to ensure accurate dose estimation based on its specific sensitivity derived from the production process. To achieve this, the detectors undergo irradiation with a known dose, followed by evaluation. The measured intensity of photons is divided by the known radiation dose, resulting in a calibration factor unique to each detector. This calibration factor is then multiplied by the measured photon intensities during subsequent readouts, enabling the estimation of the corresponding dose.

In this work, the focus is on the analysis of the raw measured TL signal. Therefore, no detectors are calibrated. The information about the intensity of the individual TL signals is neglected by normalising all GCs to their respective maximum to reduce the variation of the measured GCs and to enable the comparison of the individual GCs. Furthermore, the evaluation algorithms commonly utilised for determining the deposited dose during routine operations are disregarded in this study.

3 Study Strategies

Current TL dosimeter systems commonly employ the integration of the GC and background subtraction to estimate the radiation dose. While this approach provides a reasonable estimate, it is associated with several issues. Firstly, the thermoluminescent material consists of various traps with different half-lives, ranging from minutes to years. Traps that depopulate rapidly do not emit photons during readout, reducing the intensity of the glow peaks as a function of the time between irradiation and reheating.

This phenomenon, known as fading, introduces a dependence of the measured dose on the time interval between irradiation and readout. One possible solution to this problem is pre-heating the detector to lower readout temperatures like $T \approx 427\,\mathrm{K}$, which promotes the depopulation of short-lived traps [33]. This step ensures that each detector in the read-out process fulfils the same requirements for dose estimation, regardless of how much time has passed since the dosimeter was used. However, this approach has the drawback of reduced photon emission and decreased sensitivity. Secondly, the time gap between detector preparation and irradiation causes time-dependent alterations in the GC, known as pre-irradiation fading, which can impact dose estimation accuracy. Thirdly, current dosimeter systems lack information about the radiation type and precise exposure time of the dosimeter.

This project aims to develop comprehensive strategies to address these challenges in TL dosimeters and extract more detailed information beyond current capabilities. Advanced statistical methods, particularly ML algorithms, will be employed to analyse measured GCs. The focus will be on cases involving lithium fluoride irradiated with photons. By leveraging state-of-the-art ML algorithms and incorporating additional information about the irradiation process, this project aims to explore the potential of GC deconvolution fully. Successful completion of this project holds promise for advancing applications in personal dosimetry by introducing a new dimension of analysis.

The project comprises two main parts: (1) the estimation of irradiation day using deep learning approaches and (2) the generation of GCs using generative adversarial neural networks.

Irradiation Day Estimation

The first part of the project builds on previous theses [13, 34, 35] that focuses on information extraction from GCs using deconvolution processes based on modelling GC according to the one-trap-one-recombination (OTOR) model [29]. The GC is first transformed from time-space into temperature-space and then analysed. The resulting modelled GC peaks are used to provide both a dose estimate and an irradiation day estimate based on the ratios of the GC peak intensities. This method provides an irradiation day estimate with an uncertainty of 10 days, which is unsatisfactory for reliable radiation protection. Consequently, in this project, ML algorithms were employed for the first time to develop an improved method for irradiation day prediction, which has shown promising results [14, 13, 16].

However, a GC transformation into temperature-space is associated with many uncertainties amplified by the choice of the reconstruction model. A possible uncertainty is the reconstruction of the temperature of the detectors during the readout process, which can be estimated due to exponential heating but cannot be measured during the read-out process. Additionally, the fit function used to describe individual peaks is subject to a simplified model that may not adequately represent the TL signal.

The GC in time-space is considered and analysed in Chapter 5 to overcome the uncertainties arising with the GC transformation into temperature-space. Since much information can be extracted from a GC, which depends on the irradiation event, this work uses the application of ML for the irradiation day estimation of TL detectors with single dose irradiation for a monitoring interval of up to 40 days. The method is tested on idealised measurement data sets described in detail in the following Chapter 4. All measurements were performed with regulated storage and temperature conditions to enable the most accurate reconstruction of the irradiation day. All preparation, irradiation and evaluation stages of the detectors were precisely documented.

The first proof of concept study uses measured GCs not pre-heated in the readout process and irradiated with a single dose of 10 mGy. These GCs thus contain more time-dependent information in the TL signal. This study investigates whether an ML approach can assign these GCs to a specific irradiation day. Since the pre-heating step cannot be neglected in the routine operation of dosimetry at the MPA NRW, two other series of measurements are tested as an extension and approximation to the real-world application. These series involve pre-heated GCs, where the dose of individual detectors varies between 0.3 mGy and 10 mGy.

Initially, GCs with a dose of 10 mGy are tested because a high irradiation dose produces a high photon yield in the readout process. This high signal yield is important for the

proof-of-concept study to detect even small changes in the GC shape depending on the storage time. Further irradiation doses are then used to test the potential of the final model and thus move a step closer to a real-world application.

Glow Curve Generation

The implementation of a ML application requires large datasets, which currently cannot be sufficiently covered by measured GC. The second part of this project focuses on the generation of artificial GC to enable the simulation of various irradiation scenarios based, for example, on kinetic parameters according to Ref. [36, 37, 38, 39]. For this purpose, the different TL models and simulations of the TL phenomenon according to Ref. [40, 41] are used.

In the context of a master's thesis, A. Schneider developed a simulation based on Ref. [42], adapting the model from linear heating of the detector to exponential heating [43]. The large number of parameters to be simulated, which describe the recombination process within the lithium fluoride for each GC peak, leads to some challenges and problems. Firstly, it turned out that there are discrepancies between the individual recombination channels according to the model by Ref. [42], which makes it impossible to recreate an entire GC of LiF:Mg,Ti without modifying the model. Furthermore, the composition of peak 5 in the GC does not seem to be fully explained by Ref. [42]. Since modelling the TL phenomenon is a very complex problem, direct mathematical modelling of the GC is not possible. [43]

Therefore, this work aims to generate GC based on multivariate analysis techniques. The theses of F. Mentzel [34] and M. Rempe [44] provide the foundation for the results shown in Chapter 6. These two theses use the temperature-reconstructed GC as a base for two different ways of generating GCs. In one approach, the parameters describing the GC in temperature space were simulated by interpolation as a function of the irradiation day. The second method utilises a generative neural network to generate artificial GC parameters corresponding to a specific irradiation day. Both approaches hold potential for GC generation. However, both studies were conducted on non-tempered GCs, and their applicability to real-world scenarios has yet to be demonstrated. The GCs generated by these models are also subject to uncertainties arising from temperature reconstruction, which is not included in the GC generation process in this project.

In Chapter 6, a ML approach is employed to generate irradiation-day-dependent GCs using the entire TL signal. This method enables interpolation to irradiation days without measured GCs, thereby reducing the effort involved in planning and conducting measurement campaigns and enhancing the prediction performance of irradiation day estimation.

A high level of statistics is required to analyse the influence of the time since irradiation of the TL signal. This statistic is represented by the number of TL GCs and the high variation of exposure times within a monitoring interval of one month. At the beginning of the study, a proof-of-concept is first conducted to show that the ML approach for determining the exposure date is feasible for an idealised data set with single-dose irradiation of $D = 10\,\mathrm{mGy}$ and no pre-heating applied. The high dose was chosen to realise a high photon yield and thus reduce the signal-to-noise ratio of the measurement, which allows a more apparent GC shape depending on the readout time.

The data set measured for this purpose was described for the first time in Ref. [16]. Since this data set contains GCs that have not been pre-heated in the read-out process, this data set is referred to as a *Non-Tempered Data Set.*

In addition, two other series of measurements were performed within the scope of this work, which is intended to approximate an actual real-world application. Firstly, a data set was measured and analysed with single-dose irradiation of $D = 10\,\mathrm{mGy}$. In addition, the pre-heating step was also included in the read-out process. This data set was presented for the first time in Ref. [18].

In order to also take into account the influence of the dose, the dose to be irradiated was varied in a range from $0.3\,\mathrm{mGy}$ to $8\,\mathrm{mGy}$ in a further series of measurements in addition to varying the irradiation times. These two additional data sets are referred to in the following as *Data Set 1* and *Data Set 2*. The following first describes the experimental procedure of irradiation with photons. The measured data set is then presented in its entirety.

4.1 Experimental Setup

In preparation for the individual measurement series, the TL-DOS detectors (non-tempered data set: 554 detectors; data set 1: 4200 detectors; data set 2: 6050 detectors) were regenerated on the same day by heating them at $653\,\mathrm{K}$ to delete any possible residual signal on the detectors. Subsequently, the detectors are divided into groups assigned to a specific irradiation date. In the time between regeneration and irradiation, as well as the time after irradiation until read-out, the detectors are stored under controlled conditions

in a light-proof box in the same room to create the same thermal fading conditions for all detectors and to reduce the impact of optical stimulation. The storage temperature of the detectors is about $292\,\mathrm{K}$. Therefore, it is expected that during storage after irradiation, the unstable traps will be deleted and thus change the shape of the TL signal.

Every irradiation for this thesis was performed using the Caesium (Cs-137) irradiation facility of the MPA NRW, one of two gamma-ray irradiation facilities used for characterising and calibrating the TL-DOS detectors. The facility has a control system and a lead-coated irradiation apparatus containing the Cs-137 radiation source. Cs-137 decays to Barium Ba-137m by beta decay with a half-life of $30.17\,\mathrm{a}$, releasing an electron with an energy of up to $1.174\,\mathrm{MeV}$. The excited Ba-137m then releases its excess energy in the form of gamma radiation with an energy of $0.662\,\mathrm{MeV}$ and a half-life of $2.55\,\mathrm{min}$ to reach a stable state of Ba-137. [45] The resulting beta radiation is neglected because the electrons are absorbed in the collimator of the irradiation apparatus. Figure 4.1 depicts the decay scheme of Cs-137.
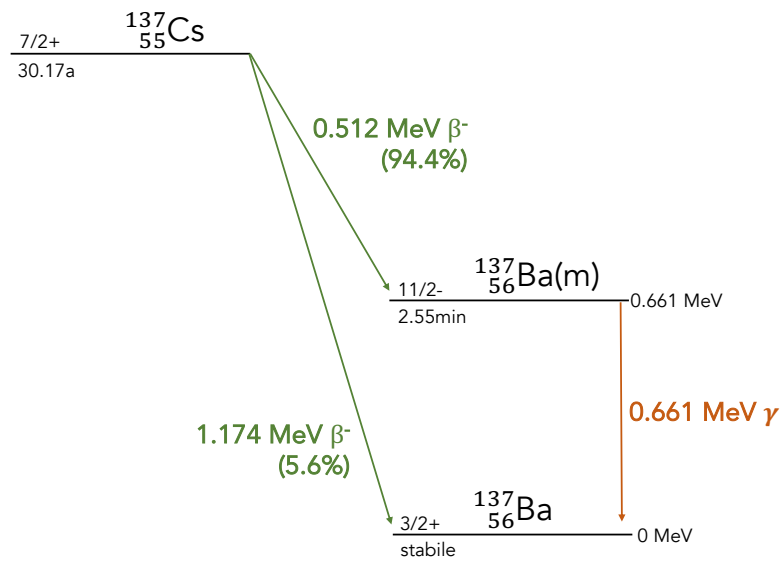
Figure 4.1: Decay scheme: Caesium-137 showing half-life, daughter nuclides and the type and energy of the emitted radiation. Adapted from Ref. [45].

There are two different ways to position the detectors for irradiation. On the one hand, in an irradiation frame, see Figure 4.2, in which up to 25 detectors can be positioned. On the other hand, in a stacked form in a transport magazine of the readout device, see Figure 4.3. 150 detectors can be stored and irradiated in the magazine.

Figure 4.2: Irradiation frame provided by the MPA NRW for TL-DOS detector calibration.

The irradiation frame and the magazine are made of plastic, which is used for the dose build-up of the photons. Therefore an additional dose build-up plate is no longer necessary to generate the secondary electron equilibrium. The difference between these two methods is the number of detectors that can be irradiated simultaneously and the direction in which the photons are irradiated onto the detector surface. The detectors in the frame are irradiated at a radiation incidence angle of 0° onto the frontal detector. On the other hand, the stacked detectors in the magazine can only be irradiated with an irradiation angle of 90°.


Figure 4.3: Filled detector magazine provided by the MPA NRW for storage and transportation of the TL-DOS detectors.

The influence of irradiation in the magazine was investigated as part of a bachelor's thesis by M. Özdemir [46]. It was shown that the aluminium ring of the detector has an attenuating effect of up to $10\,\%$ on the deposited dose. Furthermore, the dose is not dependent on the position of the detectors in the magazine. Only the dose of the top detector in the magazine shows a more substantial deviation than the other detectors since there is less scattering material around this detector. A dummy detector with no

detector material is placed before the top detector to avoid this dose drop. [46] This procedure is performed in the following for all magazine irradiations.

Before irradiation, the Cs-137 source is located in the safe of the irradiation facility and is hydraulically transported to the collimator at the beginning of irradiation. The time the source remains at the opening determines the applied dose at a predefined distance. All irradiations were carried out at a distance of 1.60 m from the source. The isocentre of the radiation field was displayed in the beam path with the help of a fixed laser. Thus, the irradiation positions can be reproduced very precisely. The irradiation dose is calibrated by determining the time it takes to measure a specific dose with an ionisation chamber at the irradiation position. The dose indication of the ionisation chamber is additionally corrected for temperature and air pressure.
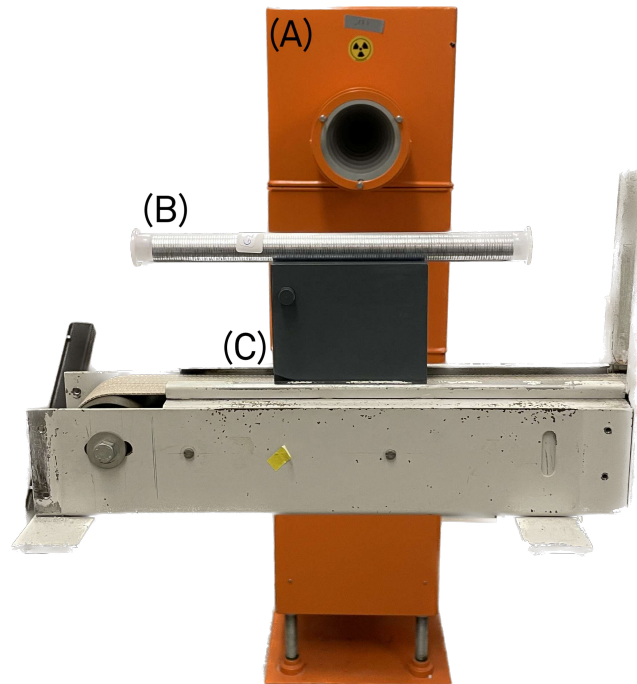
Figure 4.4: Cs-137 Irradiation apparatus at the MPA NRW **(A)** with the placed full detector magazine **(B)** on a holder **(C)** at irradiation position.

Figure 4.4 depicts the positioning of the magazine. The magazine is also placed on a holder that lifts the magazine to the height of the isocentre. Not only filled magazines are irradiated, but also partially filled magazines, as a number of 150 detectors per irradiation group is not always selected. For this purpose, the detectors in the magazine are positioned in the centre of the magazine using placeholders made of cotton wool, as shown in Figure 4.5. A dummy detector is also placed on the top detector to compensate for the scattered aluminium. M. Özdemir showed that without an additional dummy

detector, the dose deviation on the top detector compared to the other detectors in the magazine could be up to $20\,\%$ since the sensitive surface of the detector is not surrounded by additional scattering material, as is the case for the other detectors [46].

Figure 4.5: Partially filled detector magazine with 50 detectors on the holder. The detectors are centred within the magazine using cotton wool placeholders.

4.2 Read-out Procedure

A distinction is made between the two read-out methods for the read-out of the detectors. Method 1 is performed on a second-generation prototype read-out device, and method 2 on an officially approved read-out device used for routine operation at the MPA NRW. The choice of temperatures for the individual read-out steps of the readout process results from early studies of the TL-DOS project. The temperatures needed to empty certain traps were investigated based on (2.5). The heating behaviour of the detectors during exponential heating was investigated as part of multiple bachelor and master theses by J. Egert [47], A. Lütfring [48], O. Lynnyk [49] and H. Rotgeri [50], resulting in the certain temperatures of the individual stations. The differences in the temperatures of the two methods are due to the different heating technologies installed in both systems. Despite the different readout temperatures, no further change in the GC shape is expected except the one resulting from the pre-heating omission. The differences between the two methods are explained in more detail below.

Method 1:

A second-generation prototype was used to measure the non-tempered data set, explained in detail in Ref. [31]. The detectors are exponentially heated by a contact heater for $t_{\text{read-out}} = 10\,\text{s}$. The maximum heating temperature of the read-out station is $T_{\text{read-out}} = 573\,\text{K}$. During heating, the emitted photons are detected using a photomultiplier. The detectors are then heated in an additional heat-out step for a further $t_{\text{heat-out}} = 10\,\text{s}$ at

$T_{\text{heat-out}} = 673\,\text{K}$ to eliminate residual TL signal and prepare them for use again. This series of measurements only includes the read-out and heat-out steps.

Method 2:

For the read-out of TL-DOS detectors in routine operation at the MPA NRW, a new, improved generation of the read-out device, depicted in Figure 4.6, was developed by the MPA NRW and approved by the Physikalisch-Technische Bundesanstalt (PTB). The difference between the prototype and the approved read-out device is mainly in the logistics of the detectors and the temperatures at which the detectors are heated. The read-out device consists of four main components. Two magazine carousels are used to store and transport the TL-DOS detectors. The detectors from the input magazine pass through the pre-heating station, the read-out station and the heat-out station before they are sorted into the output magazine. The detectors are pre-heated at a temperature of $T_{\text{pre-heat}} = 427\,\text{K}$ for $t_{\text{pre-heat}} = 9\,\text{s}$ before they are exponentially heated in the read-out station for $t_{\text{read-out}} = 15\,\text{s}$ at $T_{\text{read-out}} = 653\,\text{K}$, and the photons are detected simultaneously. An active cooling system cools the detectors to room temperature between the heating steps. The temperature of the heat-out station was reduced to $T_{\text{heat-out}} = 673\,\text{K}$ and the heating time to $t_{\text{heat-out}} = 9\,\text{s}$ because most of the signal was already deleted by the high read-out temperature. Detectors from data set 1 and 2 run through this read-out process.
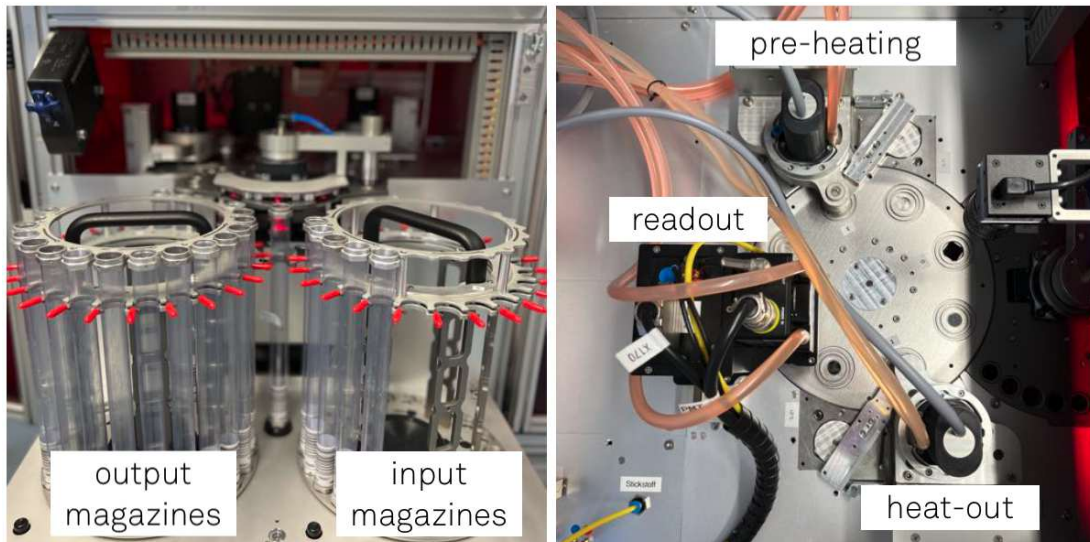
Figure 4.6: Read-out device of the TL-DOS system. Left: Frontal view with the input and output magazines for transportation of the detectors; Right: Inside view with the pre-heating, readout and heat-out stations. Adapted from Ref. [46].

4.3 Measured Data Sets

In the following section, the individual measurement series are characterised.

4.3.1 Non-Tempered Data Set

The non-tempered data set was measured by F. Mentzel and described for the first time in Ref. [16]. This data set consists of 554 GCs measured in prototype 2 of the read-out apparatus according to Ref. [31]. The detectors were irradiated with a single dose of $D = 10\,\mathrm{mGy}$ in the Cs-137 irradiation facility using the irradiation frame, with about 25 detectors per frame, see Figure 4.2 (right). Twelve different pre-irradiation times t_{pre} are chosen between the regeneration and irradiation of the detectors, and each t_{pre} up to 50 detectors, as shown in Figure 4.7. The investigated time interval is $40\,\mathrm{d}$.

$$t_{\mathrm{pre}} = [1, 4, 8, 11, 15, 18, 22, 25, 29, 32, 36, 39]\,\mathrm{d}$$

For $t_{\mathrm{pre}} = 15\,\mathrm{d}$, the number of detectors is smaller than for the other times due to technical problems during the read-out process.
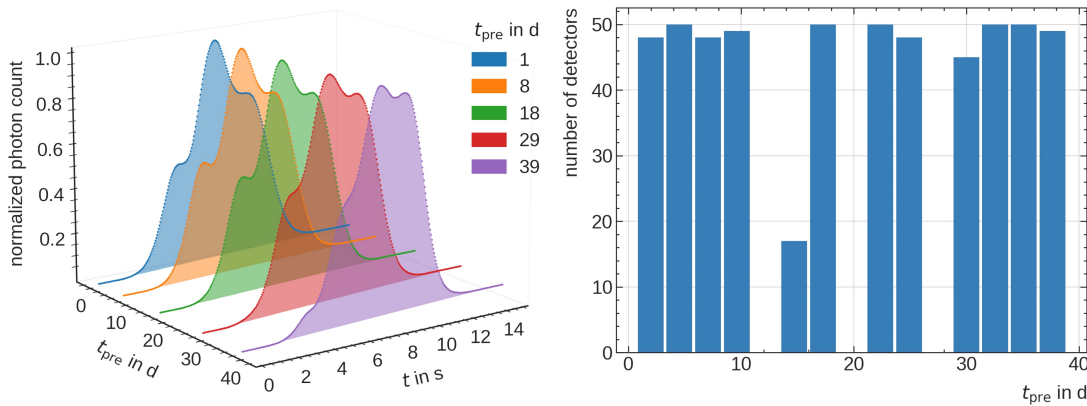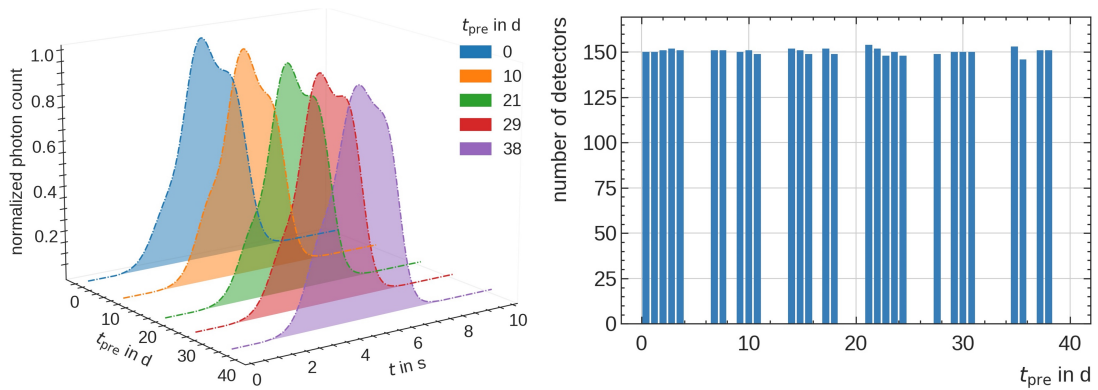

Figure 4.7: Depiction of the non-tempered data set. Left: Glow curve shape in dependence of the pre-irradiation time t_{pre} normalised by the glow curve maximum. Reproduced from [17]; Right: Distribution of the number of detectors per t_{pre}.

The Figure on the left in 4.7 shows five average GCs for different t_{pre} normalised by their respective maximum. There are apparent differences in the shape of the GCs as a function of the pre-irradiation time. The blue curve represents the GC with approximately one day of the shortest storage period between regeneration and irradiation. In contrast, the purple GC has the most extended period of 39 days. Compared to the others, the curve at $t_{\mathrm{pre}} = 39\,\mathrm{d}$ shows a hint of peak 2, which is otherwise eliminated by pre-heating the detectors. Furthermore, the change in the ratio of peaks 4 and 5 depends on t_{pre}.

For this data set, the differentiability of the GCs for the different irradiation times is apparent by eye. However, GC parameters are extracted from the measured GCs using the *gcpy* analysis tool as described in section 2.3.3 to estimate the irradiation day accurately.

4.3.2 Data Set 1 - Single-Dose Irradiation

The implementation of an officially approved read-out device for routine operation enables the measurement of detectors with a high capacity. Compared to the prototype, up to 3600 detectors can now be read out in one run. In this course, a series of measurements are performed with 4200 detectors, which are read out using method 2. Compared to the non-tempered data set, pre-heating is added to correspond to a routine evaluation.

Figure 4.8: Depiction of the pre-heated data set 1. Left: Pre-heated Glow curve shape in dependence of the pre-irradiation storage time $t$pre normalised by the glow curve maximum; Right: Distribution of the number of detectors.

The high dose of $D = 10\,\mathrm{mGy}$ is maintained to keep the photon yield high. The irradiation of the detectors was performed in the magazine as described in the previous section. For this purpose, the approximately 150 detectors assigned to an irradiation day were first stored in a magazine, then irradiated in this magazine, and then stored again until read out. The number of irradiation times is increased to 28 different days, with the number of detectors per irradiation time averaging about 150; see Figure 4.8.

$$t_{\mathrm{pre}} = [0, 1, 2, 3, 4, 7, 8, 9, 10, 11, 14, 15, 16, 17, 18,$$
$$21, 22, 23, 24, 25, 28, 29, 30, 31, 35, 36, 37, 38]\,\mathrm{d}$$

Similar to the left Figure 4.7, average GCs normalised by their respective maximum for five different pre-irradiation times are displayed in Figure 4.8. However, there is a clear difference in the GCs compared to the non-tempered ones. Again, the blue GC represents

the group of detectors with the shortest time between regeneration and irradiation event and the purple GC with the most extended storage period. The pre-heating process has the effect that, in addition to the unstable trap states of peaks 1 and 2, peak 3 is almost eliminated. As a result, the differentiability of the GCs as a function of the t_{pre} is hardly possible with the bare eye. Only differences in the ratio of peaks 4 and 5 as a function of t_{pre} can be determined. Furthermore, as the pre-irradiation time increases, peak 3 tends to merge with the central one, and the height of peak 5 changes over time. The apparent increase in peak 5's height results from the decrease of peak 4, which is utilised for normalising the GC.

4.3.3 Data Set 2 - Irradiation with varying Doses

As an extension to data set 1, a series of measurements is performed under the same storage and irradiation conditions. However, the irradiation dose varies per irradiation event in addition to the pre-irradiation time. On each irradiation day, detectors are irradiated with doses between $0.3\,\text{mGy}$ and $8\,\text{mGy}$. A single irradiation event, which can be assigned to a specific irradiation day and a specific dose, contains 30 TL-DOS detectors. Thus, only 30 detectors are irradiated simultaneously, as shown in Figure 4.5.

$$t_{\text{pre}} = [0, 2, 4, 8, 9, 10, 11, 15, 16, 17, 18, 22, 23, 25, 30, 31, 32, 40, 41, 42]\,\text{d}$$
$$D = [0.3, 0.5, 0.75, 1, 1.5, 2, 3, 4, 6, 8]\,\text{mGy}$$

Figure 4.9 shows the distribution of detectors per-irradiation time and the corresponding dose value. It can be seen that the distribution is not uniform as a function of time, which is connected with the feasibility of preparing the detectors for the measurement series. Due to the high number of detectors for this measurement project, there are difficulties in the regeneration process that affect the regeneration time. Since several read-out devices do not guarantee a parallelisation of the regeneration process, there are time differences of several hours up to one day per group of detectors assigned to the same pre-irradiation time. Despite this, care was taken to ensure that as many different irradiation doses represent each selected irradiation day as possible.

About 6050 detectors were irradiated and read out at 20 pre-irradiation times for this data set 2. Figure 4.10 shows examples of individual GCs at different pre-irradiation times and for different irradiation doses. Each colour is assigned to a specific pre-irradiation time. The GCs are normalised to their maximum and then smoothed with a Savitzky-Golay filter [51] to clarify the course of the individual GCs. It can be seen that the GCs of the same irradiation time have approximately the same shapes for the

different doses. The variation within the pre-irradiation times can be attributed to the signal-to-noise ratio, which depends on the number of photons detected during the read-out process. Thus, GCs irradiated with low doses below $1\,\mathrm{mGy}$ have high noise within the signal, making the shape of the GC more challenging to differentiate.
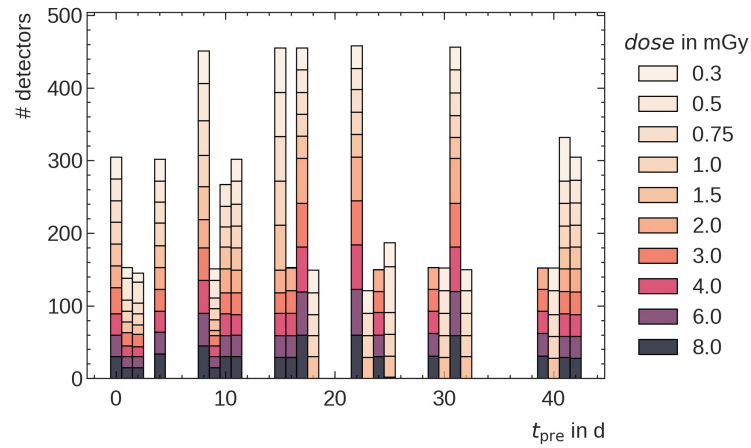

Figure 4.9: Detector distribution of data set 2 in dependency of the t_{pre} and the dose.
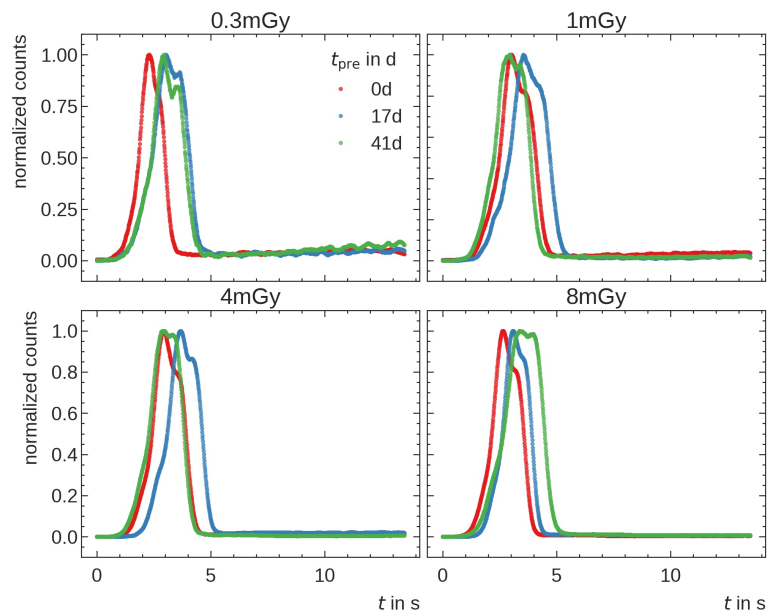

Figure 4.10: Exemplary normalised glow curves for different pre-irradiation times t_{pre} and doses from the data set 2.

4.4 Data pre-processing and Data augmentation

In order to successfully train a neural network, it is necessary to take a few steps to prepare the data. First, the data set is divided into 70% training and 30% test data. Care is taken to ensure that the parameter to be learned is equally distributed in both the training and test data sets. This prevents GCs for particular pre-irradiation times from being represented only in the training data set or only in the test data set, which can limit the generalisability of the model. The test data set only evaluates the final model and allows an unbiased neural network evaluation.

The training data set is again divided into an 80% training and 20% validation data set for the training process of the neural network and to enable an evaluation of the neural network during the training process. To evaluate the training independently of the division of the training and validation data set, a 5-fold cross-validation is performed. The entire training data set is divided into five folds with a ratio of 1/5 validation and 4/5 training data, see Figure 4.11. This division is used for one training run and iterated in the subsequent runs until the validation data set consists of each of the five folds. This form of validation allows us to ensure that the choice of training and validation data prevents over-fitting or under-fitting data to the model.
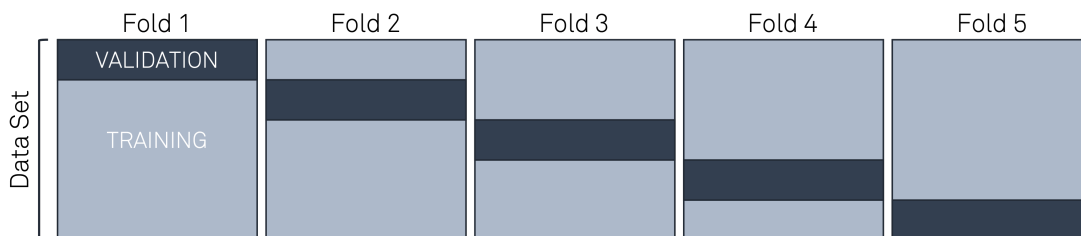

Figure 4.11: Schematic representation of the 5-fold-cross validation split.

Due to the limited statistics in the measured data set, data augmentation is performed on the training data in addition to pre-processing, which is intended to improve the robustness of the machine learner. The aim is to avoid the model being too sensitive to specific properties or details within the GCs, which reduces the probability that the model learns only these specific properties and instead creates a more generalised model that describes all data equally well.

Data augmentation is a synthetic extension of the data generated by a transformation of the existing data. Based on the specific application of the augmentation, there are different techniques, such as rotations, reflections, translations, scaling, the introduction of noise or even colour changes. In the following, the training data set of data sets 1 and 2 are extended to 20k GCs by randomly shifting and noising the GCs.

Due to the individual dose response of each TL-DOS detector caused by the fabrication conditions, each GC has a different intensity maximum. In order to avoid the influence of the intensity differences of the individual GCs and to be able to compare the GC shape more efficiently, it is first smoothed with a Savitzky-Golay filter to determine the relative maximum of the curve better. Figure 4.12 shows an example GC with the measured photon count, the smoothed GC and the resulting GC maximum.
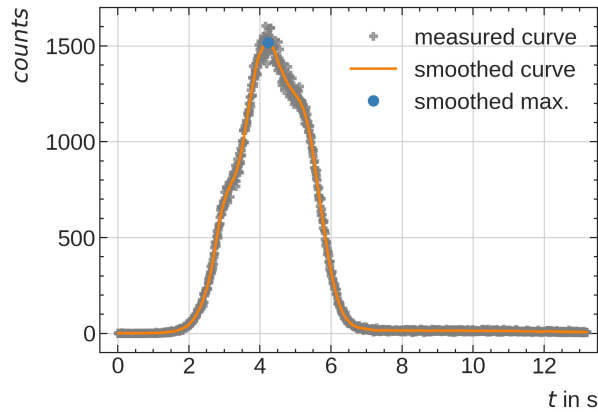

Figure 4.12: A smoothed glow curve using the Savitzky-Golay filter to determine the relative maximum of the curve.

The measured GC contains 1320 data points, and the shifts are performed on the smoothed GC. The position shifts to the left or right are made by randomly selecting a value according to a Gaussian distribution with a mean of 0 and a standard deviation of 10 entries. Depending on the shift, the first or last entries of the GC are removed and added to the other end to return to the original number of entries. The added entries correspond to the average of the neighbouring entries so that no information is lost. An illustration of the shift is shown in Figure 4.13. After the positional shift of the smoothed GC, additional random Gaussian noise with a mean of 1 and a standard deviation of $\sqrt{N_{\text{Photon},i}}$ is added to the individual GC data point i to recreate the noise of the original measured GC.

As a final pre-processing step before the GCs can be used as training or test data, all GCs are normalised to their respective smoothed maximum to reduce the impact of the dose-response of each detector. The high dimension of the GC is reduced by applying average pooling to the GC. The average value of the photon counts is calculated over a pool size of $k = 10$, resulting in a GC with 132 entries. This dimension reduction prevents the model from becoming sensitive to minor local variations within the GC, as the individual photon counts are as important as the overall shape of the GC. Furthermore, the complexity and robustness of the neural network can be increased without losing

relevant information from the GC. Figure 4.14 depicts an exemplary pre-processed GC. It can be seen that the dimension reduction does not cause any change in the course of the GC.
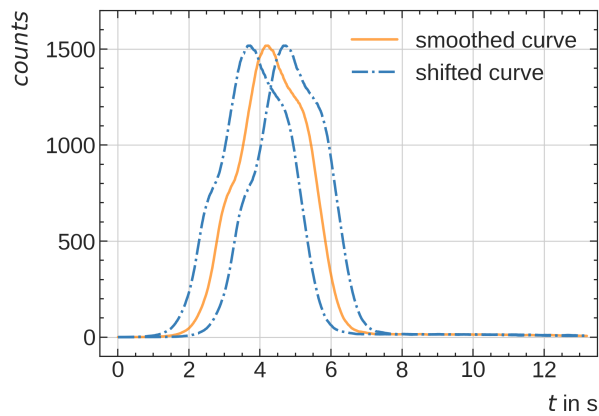
Figure 4.13: Exemplary smoothed glow curve (orange line) with shifted glow curves (blue dashed line).
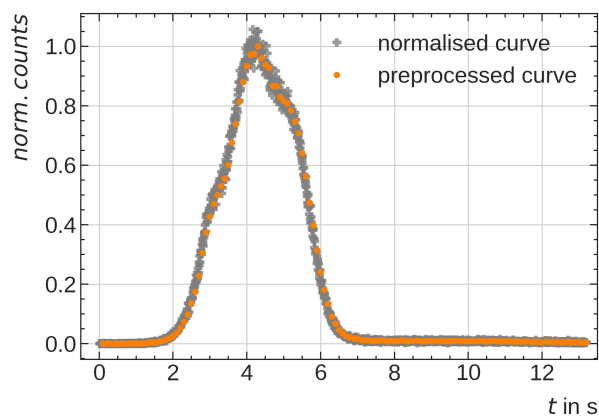
Figure 4.14: Normalised glow curve and the resulting average pooling with a pool size of 10.

In the past, the determination of an analytical model function to estimate the irradiation day has proven to be a complex problem. By describing the decay processes in the TL material, dependencies on the irradiation day can be drawn. However, modelling these processes depends on the material and the heating process, making it difficult to model a generalisable one. In addition, the decay process still cannot be fully explained, so many decay models exist and are still being researched [36, 42]. In this context, neural networks are used to parameterise a function based on measured GCs with different irradiation points to predict the irradiation time. In the following, two different ML approaches will be used, which allow for a prediction based on extracted physically relevant GC parameters with a fully-connected neural network and based on the raw GC shape using a convolutional neural network.

5.1 Machine Learning

ML represents a class of algorithms that recognise and model complex relationships, such as patterns or structures in the underlying data. Mathematical and statistical techniques form the basic framework that enables the algorithms to learn from the underlying patterns in the data. The learning process involves adjusting the parameters or weights of the model based on the observed data, allowing the model to improve its performance over time.

Different machine learning algorithms include supervised, unsupervised, and reinforcement learning. The prediction of a known quantity, in this case, the estimation of the irradiation day, is realised by supervised learning. The model is trained on labelled input data with a known desired output variable, and it learns to approximate a model function that can map the relationship of the input data to the output values. Unsupervised learning deals with unlabeled data, and the algorithms learn patterns or structures within the data. Reinforcement learning involves an agent learning to interact with an environment and maximise its rewards through trial and error. Since unsupervised and reinforcement learning is not part of this work, more details can be found, for example, in Ref. [52, 53, 54].

Supervised learning can be further divided into two subcategories: classification and regression. Each technique has its strengths and is suited for different types of problems

and data. Classification is the prediction of discrete target variables, including discrimination between different irradiation types. On the other hand, the estimation of the radiation day is a regression task since a target variable is predicted from a continuous distribution. Machine learning comes with its challenges. For example, it requires careful data pre-processing, model selection, hyperparameter tuning, and evaluation to ensure accurate and dependable results. Furthermore, overfitting, where the model performs well on training data but fails to generalise to new data, and underfitting, where the model fails to capture the underlying patterns, can occur.

5.1.1 Deep Learning

ML contains many subfields; one is Deep Learning, which focuses on training artificial neural networks with multiple layers to learn and make decisions or predictions. Neural networks are based on the structure and information transfer in the human brain. It creates complex models which are capable of capturing intricate patterns in data.

Deep learning is primarily founded on the fundamental framework of deep neural networks. These networks comprise interconnected layers of artificial neurons, known as nodes, that work together to process and transform input data. Each layer receives input from the previous layer, performs computations using learned parameters, and passes the output to the next layer, gradually building a hierarchy of representations. A single-layer perceptron can describe the simplest application of a neural network. It consists of an input layer directly connected to the output layer. A single-layer perception, see Figure 5.1, consists of the input neurons with the initials variables X_n with the corresponding weights w_n, representing the strength between the neurons. Higher weight values correspond to a higher influence on the neuron. The bias unit b allows changing the output of the activation function for the next neuron. The activation function $f(X)$ calculates the weighted sum and adds the bias value, which can result in neuron activation Y as an output value.

$$f(X) = \sum_{n=1}^{N}(X_\mathrm{n} \cdot w_\mathrm{n}) + b \tag{5.1}$$

For the single-layer perceptron, a one-dimensional output is shown in Figure 5.1. The dimensionality of the input and output depends on the problem and can therefore vary.

A single-layer perceptron can learn linear decision boundaries and solve simple classification problems. However, it cannot approximate complex functions or capture non-linear relationships in the data. Extending the single-layer perceptron by adding hidden layers between the input and output layers, where each neuron is connected to

each neuron in the following layer, creates a deep neural network (DNN), also referred to as a fully-connected feed-forward neural network, see Figure 5.1.
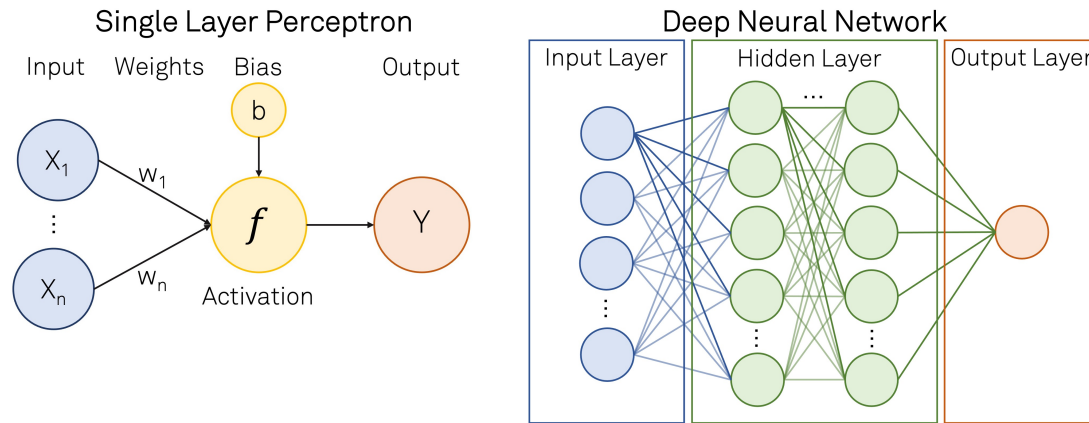
Figure 5.1: Representation of a single-layer perceptron consisting of input, weights, activation and output and a deep neural network consisting of input, hidden, and output layers.

DNNs can learn deep hierarchies of feature representations and approximate complex functions. In doing so, lower layers learn low-level features, e.g., edges or textures. On the other hand, the higher layers can extract and learn successively more abstract and complex features, which enables the networks to extract and understand increasingly sophisticated patterns and improve performance on complex tasks. The number of hidden layers and their dimensionality depends on the complexity of the task to be solved. The ability to model non-linear relationships makes DNNs extremely powerful in various tasks such as image or speech recognition.

Two main steps are involved when training a DNN — the feed-forward propagation and the backpropagation. First, the input data is fed into the network, and the calculations flow from the input layer to the output layer, resulting in predictions or outputs. Afterwards, the error between the predicted and desired outputs is calculated to adjust the network's weights and biases through an optimisation algorithm during the backpropagation, such as gradient descent. This process is regulated by the loss function, which quantifies the discrepancy between the predicted output of a model and the desired values in the training data. The loss function represents the model's performance, where a lower value indicates a better alignment between the true and predicted values. The loss function used in this work is calculated using the mean squared error (MSE). The square is formed from the difference between the true and the predicted values. After a training run, this value is transferred to the network, and the weights are readjusted. The goal is to minimise this discrepancy and provide a measure for the model's performance.

Such a training run, in which the entire training data set, divided into smaller subsets and called batches, has been propagated once, is called an epoch. The batch size refers to the number of training samples processed together in a single forward and backward pass during the model's training. The batch size can have a significant impact on the model's performance. Due to many iterations, smaller batch size results in more frequent weight updates. However, large batch sizes can reduce the noise in the parameter updates, but they also require more memory and computational resources, which can slow down the training process. This iterative process of forward and backward passes allows the network to learn from the data and improve performance.
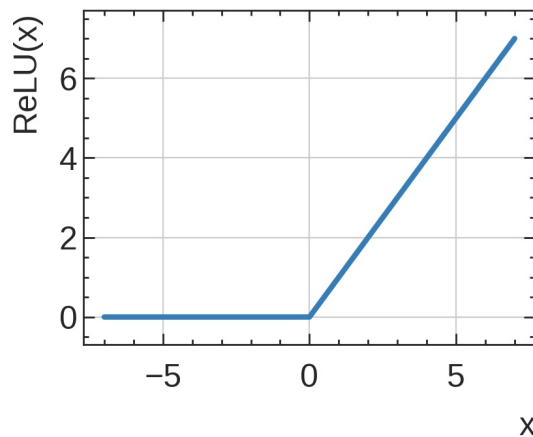
5.1.2 Activation Functions

DNNs are used to model non-linear functions. Therefore an activation function is crucial since it introduces the non-linearity to the network by performing a non-linear transformation to the weighted sum of the neuron's inputs. The choice of activation function depends on the problem to be solved and essentially determines the range of values for activating a single neuron and the functional form. The Rectified Linear Unit (ReLU) function [55] is the most commonly used activation function due to its simplicity and effectiveness.

$$\text{ReLU}(x) = max(0, x) \tag{5.2}$$

The range of values of these functions is shown in Figure 5.2. The x-axis shows the input values, and the y-axis the activation value. ReLU sets all negative input values to zero and leaves positive values unchanged. ReLU introduces non-linearity by allowing the positive components of the input to pass through while eliminating the negative elements, resulting in computational efficiency. It makes it faster to compute than other activation functions involving more complex mathematical operations, e.g. exponential calculations [56].

The primary advantage of ReLU is its ability to address the vanishing gradient problem. During backpropagation, the gradient indicates the direction and magnitude of the error used to update the model's weights. In traditional activation functions like sigmoid or tanh, the gradients can become extremely small for inputs far from zero, leading to slow convergence or no learning. ReLU, on the other hand, avoids this issue by maintaining a constant gradient for positive inputs, thus accelerating the loss function's minimisation, resulting in faster and more effective learning.

However, setting all negative input values to zero can also lead to the dying ReLU problem. In this case, neurons that always assume a negative value can be deactivated and thus no longer contribute to the training since the gradient that runs through these

Figure 5.2: ReLU activation function with the resulting output range for certain input values x.

neurons also becomes 0. These neurons are also referred to as "dead". Depending on how many neurons are inactive, the effectiveness of the neural network can be impaired. The learning rate can be reduced, or the ReLU function can be modified, e.g., to a Leaky-ReLU function (5.3) to counteract this effect [57]. Instead of setting all negative input values to zero, a limited linear component is added to the negative values, and the factor α determines the limitation.

$$\text{Leaky-ReLU}(x) = \max(\alpha x, x) \tag{5.3}$$

5.1.3 Deep Learning Approaches

In the context of this project, two deep learning approaches are used for irradiation day estimation: the fully-connected feed-forward neural network / Dense Neural Network (DNN) and the Convolutional Neural Network (CNN). DNNs can approximate complex non-linear functions between the input and the output of the model, which makes them suitable for various tasks, like regression or classification. They learn relevant features within the data by extracting meaningful patterns or representations. However, DNNs cannot learn any spatial structure of the model.

CNNs were developed and designed to process grid-based data, such as sequences or images, enabling them to detect patterns or objects or to perform classification or image segmentation. The data's spatial structure is used, making it suitable for computer vision tasks. Thus, CNNs are also suitable for predicting the irradiation day since the entire GC and its spatial features can be exploited.

The combination of convolutional, pooling and fully-connected layers results in a unique design of the CNN. The convolutional layer consists of filters, also called kernels, applied

to the input data performing a convolutional operation. The filter is a matrix of weights with various sizes, e.g. 3×3, 5×5 or even 7×7 pixels. It performs pixel-wise multiplications and summing, which results in a feature map afterwards. The convolution for an arbitrary filter matrix with a size of 3×3 pixels is shown in Figure 5.3. This operation preserves the spatial relationship of neighbouring pixels by capturing features within the input data. Since each convolutional layer consists not only of one filter but several filters, the convolution of all filters across the input generates multiple feature maps representing different learned features within the image. The individual values of the filters are learned during the training and are updated through backpropagation. The filters are optimised during the training to recognise more meaningful and complex features at higher layers.
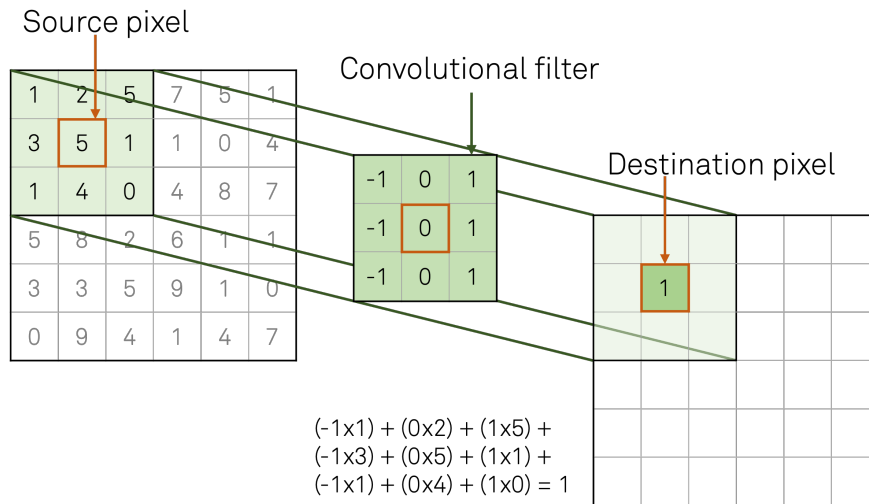

Figure 5.3: Illustration of the two-dimensional convolution operation.

In order to downsample the spatial dimension of the feature map, a pooling layer can be placed between two convolutional layers. This layer reduces the computational complexity, and therefore more meaningful features can be extracted. A typical application is Max-Pooling or Average-Pooling. As the name suggests, the neighbouring pixels' maximum or average values are transferred to the output image from a previously defined filter size. The pooling layer captures the most relevant and dominant features and simultaneously offers a certain translational invariance, preserved to the following layers. A CNN is typically terminated with dense layers to classify the extracted features from the convolutional layers.

There is a significant difference in comparing both approaches for irradiation day prediction. The DNN requires handcrafted features that may limit the representative capacity. In contrast, CNN learns hierarchical features within the data, which reduces

the manual feature engineering effort while automatically identifying relevant structures and features.

5.1.4 Model Training and Selection

During the training run, the model's generalisation is checked using a separate set of data, referred to as validation data and is a subset of the training data set. For this project, the validation data is 20 % of the full training data set. After each training epoch, the validation data set is used to estimate the performance and test the generalisation of the trained model on data that were not part of the training process. The validation provides information on whether the model has learned meaningful patterns or is overfitting to the training data.

Furthermore, the validation data set is used in hyperparameter optimisation and tuning. Hyperparameters control the model's learning process and architecture. However, the model does not learn them during training, e.g., the learning rate, the number of layers and neurons, or the regularisation strength. The learning rate describes how strongly the network adjusts the neurons' weights with regard to detected errors after each training epoch. By evaluating the model's performance on the validation data set for different hyperparameter configurations, the most appropriate values can be selected to optimise the model's performance. The validation data set is crucial in comparing different models and can be used to identify the model that achieves the best results.

Using techniques such as cross-validation or testing on an independent test data set allows further model fine-tuning. The hyperparameter choice can significantly impact the model's performance, generalisation, and training time. Therefore it requires much effort. The choice of hyperparameters can result in overfitting or underfitting of the data. The main aim of hyperparameter optimisation is to achieve the right balance and generalisation of the model. A systematic hyperparameter optimisation is performed to find the best model. Different variations of the hyperparameter sets are formed in this process, covering a wide range of parameter values. Different numbers of layers are defined with different numbers of neurons, as well as varying learning rates and batch sizes. Afterwards, these parameter combinations are iterated through with the help of a grid search to determine the best set.

A diagram in Figure 5.4 shows the hyperparameter optimisation process. First, the entire data set is divided into part training and part test data, as already described in Section 4.4. The test data set is used for testing the performance and the generalisation of the final chosen model. Then the grid search for the model selection is performed. For each set of hyperparameters, the model is trained using 5-fold cross-validation. After each fold, the 68 % percentile $\sigma_{t_{\mathrm{pre}}}$ of the absolute deviation Δt between the predicted
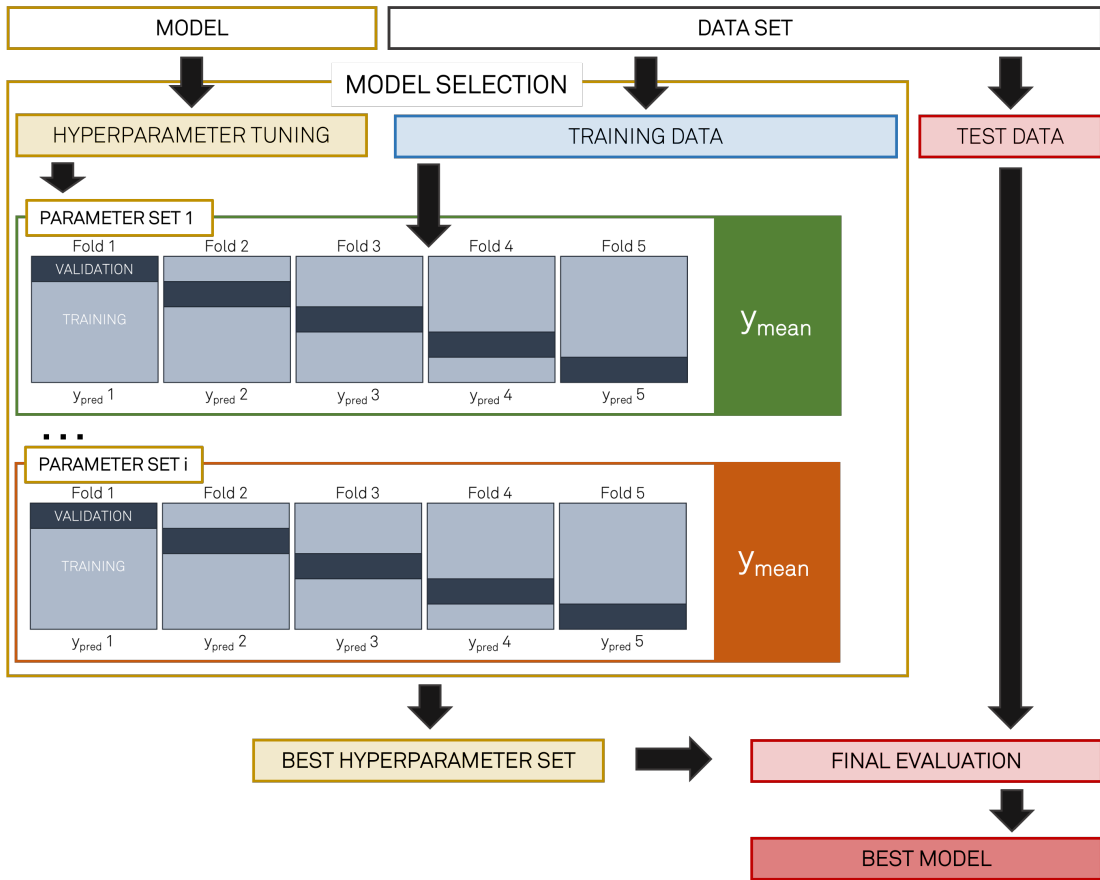
Figure 5.4: Schematic representation of the process for best model selection. Adapted from Ref. [13].

and the true value is calculated and afterwards averaged over all folds, resulting in the value y_{mean}.

$$\Delta t = |t_{\mathrm{pre}}^{\mathrm{pred}} - t_{\mathrm{pre}}^{\mathrm{true}}| \tag{5.4}$$

This measure is comparable to a normal distribution's 1σ standard deviation. After each set of parameters has been trained, the achieved predictions are compared, and the best model is selected according to the lowest deviation between the predicted and the true values. Finally, the model with the selected hyperparameters is tested and validated on an independent test dataset to assess its performance on unseen data by estimating the prediction for the test data set. This step ensures the model can generalise well and perform accurately on new unbiased data.

5.2 Irradiation Day Estimation on Non-Tempered Glow Curves

5.2.1 DNN Approach

The first approach for the estimation of the irradiation day is a Dense Neural Network (DNN) trained on 15 GC parameters derived from the 554 GCs in the time-space of the non-tempered data set, as presented in Section 4. The input data containing all GC parameters are scaled before the training using a robust standardisation by shifting the median value to zero and scaling the quantile range of $[25, 75]$ to variance 1. The target variable contains the true irradiation time and is normalised to the latest irradiation date resulting in a value range of $[0,1]$.

The hyperparameter optimisation shows the variation of the following hyperparameters:

- Number of hidden layers: [3, 4],

- Number of nodes per layer: [16, 32, 64, 128],

- Learning rate: $[0.001, 0.0001]$ and

- Batch size: [16, 32].

Each parameter range is pre-selected on the base of experience. The performance of the five best hyperparameter combinations is depicted in Figure 5.5. It can be seen, that all values generally agree with the uncertainties. The combination of hyperparameters that achieves the minimum averaged prediction uncertainty was therefore selected as the best, which is the fifth layer combination. It consists of four dense hidden layers with [64, 128, 32, 16] nodes having the minimised average prediction uncertainty of $\sigma_{t_{\mathrm{pre}}} = (3.7 \pm 0.5)\,\mathrm{d}$.

The connection weights of the DNN are optimised using the Adam optimiser, described in detail in Ref. [58], with a mean squared error loss and the best learning rate of $\alpha = 0.0001$. The best batch size for all these hyperparameter combinations is 32.
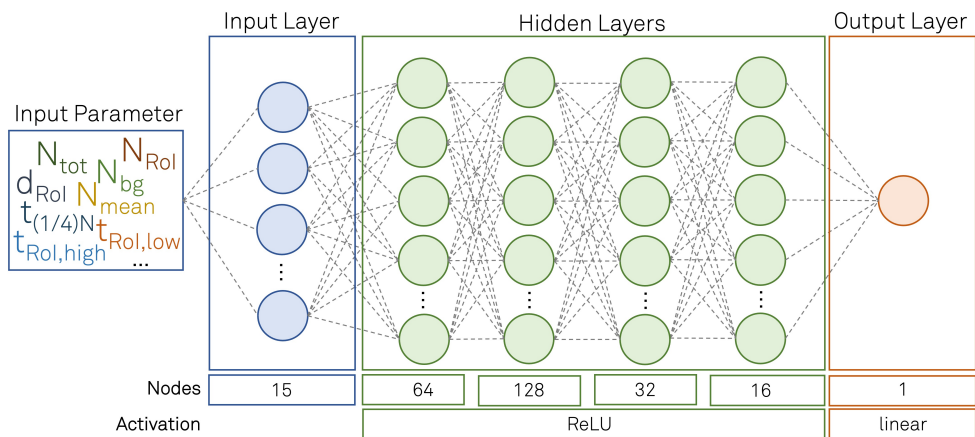
A schematic representation of the final DNN model is shown in Figure 5.6. All hidden layers are activated using the ReLU activation function, and the single-node output layer is linear activated. To reduce the effective capacity of the DNN and to prevent the DNN from overtraining, an additional L2-norm regularisation with a chosen strength of $\lambda = 0.0005$ is used for all hidden layers, see Equation (5.5).

$$LossFunction = \frac{1}{N}\sum_{i=1}^{N}(y_{\mathrm{pred}} - y)^2 + \lambda\sum_{i=1}^{N}\omega_i^2 \tag{5.5}$$

A penalty term is added to the loss function by the L2-norm regularisation, which penalises the model for high weights. The penalty term is calculated by taking the square of the L2-norm vector. The L2-norm regularisation is described in detail in Ref. [59]. The choice of the values for the batch size and the L2-norm regularisation results from the fine-tuning of the hyperparameters.
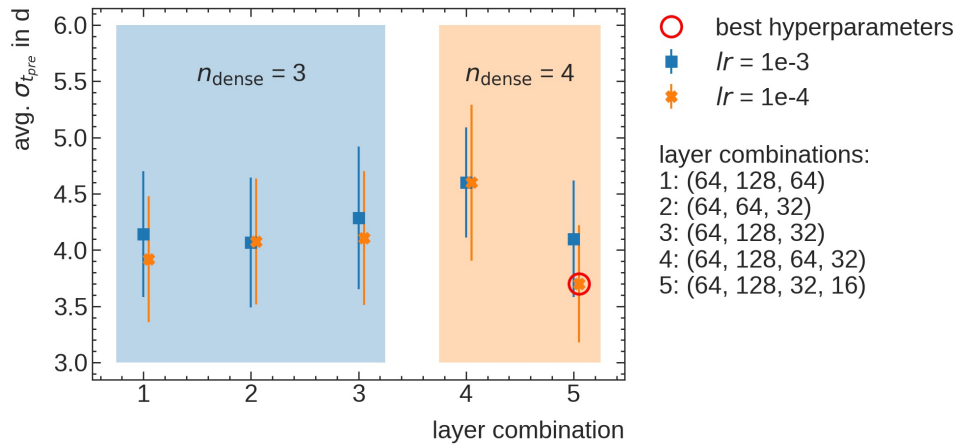

Figure 5.5: Exemplary result of the best model search using hyperparameter optimisation. The markers depict the best hyperparameter combinations with the corresponding averaged prediction uncertainty and the standard error. The number of dense layers, the number of nodes per layer, the learning rate and the batch size were varied. The best batch size for this search is found to be 32. The best hyperparameter combination is determined by the minimum average prediction uncertainty of the model.

Figure 5.6: Schematic representation of the final DNN architecture for the prediction of t_{pre}, consisting of an input layer, four hidden layers and a single-node output layer.

Irradiation Day Dependency of the Glow Curve Parameters

The dependence of the GC parameters on the irradiation day can provide information on the importance of a single parameter for the prediction process. For this purpose, the linear correlations of the GC parameters in the time-space and the day of irradiation are calculated using the Pearson Correlation coefficient. All correlations for five GC parameters with the highest correlation values are presented in percent and shown in Figure 5.7 (left). These parameters are the maximum count number N_{max} and the time that maximum occurs t_{max}, the background intercept c_{bg}, the lower limit of the RoI $t_{RoI, low}$ and the duration of the RoI d_{RoI} in addition to the pre-irradiation time t_{pre}.
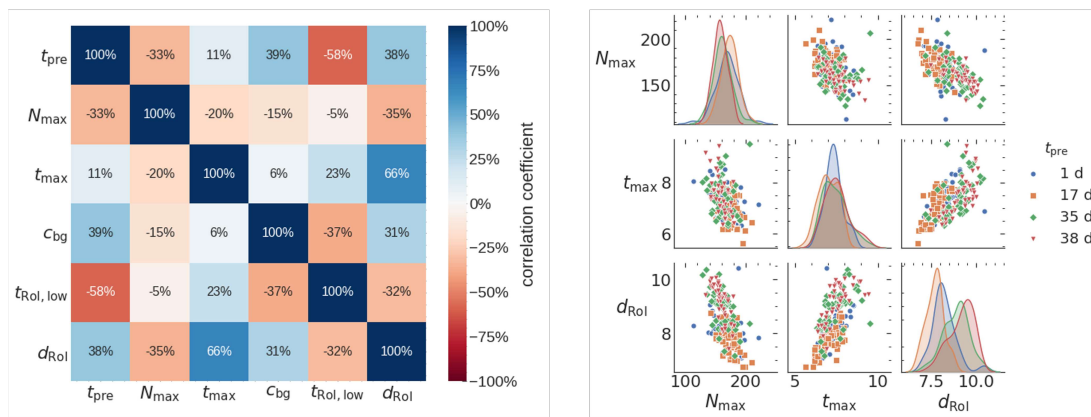
Figure 5.7: Left: Pearson correlation coefficients in percentage between five glow curve parameters with the highest correlations towards the pre-irradiation time t_{pre}; Right: In the non-diagonal, the two-dimensional inter-correlations of three selected glow curve parameters are shown in a scatter plot for various pre-irradiation times of $t_{pre} = [1, 17, 35, 38]\,$d. The diagonal plots show distribution estimations for the individual parameter for the different pre-irradiation times using the kernel density method [60], which depicts the differences in the distribution of the parameter in dependency of the different pre-irradiation storage times. [17]

It is shown that all of these GC parameters have relatively high (anti-)correlations to the pre-irradiation day with a value range between ($|\rho| = 10\,\% - 60\,\%$). Furthermore, relatively high correlations exist between the GC parameters with varying coefficient values from $|\rho| = 5\,\%$ up to $|\rho| = 66\,\%$.

The lower limit of the RoI shows the highest correlation with the pre-irradiation time with $|\rho| = 58\,\%$, which indicates that this parameter can greatly influence the prediction of the irradiation day. The correlation between the individual GC parameters can be traced back to calculating the parameters. For example, the duration of the RoI is always dependent on the determination of the lower and upper limits of the RoI. However, the high statistical variance of the GC shape influences the strength of the correlation. The individuality of each detector results in differences in the GC shape during the read-out process, making the GCs individual in some respects but still comparable to

other detectors irradiated and stored under the same conditions, which also results in a somewhat lower correlation between the time at which the maximum of a GC occurs and the day of irradiation.

Generally, the GCs can hardly be distinguished in their values depending on the day of irradiation, as shown exemplarily for three GC parameters in Figure 5.7 (right). The Figure shows scatter plots for these GC parameter correlations for different pre-irradiation times of $t_{\mathrm{pre}} = [1, 17, 35, 38]\,\mathrm{d}$ in the non-diagonal. The diagonal depicts the parameter distribution for the different pre-irradiation times. The kernel density method shows the differences in the parameter distributions in dependency on the pre-irradiation time; see Ref. [60] for a detailed explanation. The duration of the RoI d_{RoI} shows the best discrimination of the distributions for the different pre-irradiation times. However, there is no linear dependency on the pre-irradiation time.

The high scatter of the parameters and the independence of many parameters from the irradiation day illustrate the complexity of the problem and, thus, the difficulty of predicting the irradiation day. In order to solve this problem, correlations of higher order can be explored by the use of deep neural networks with non-linear activation functions.
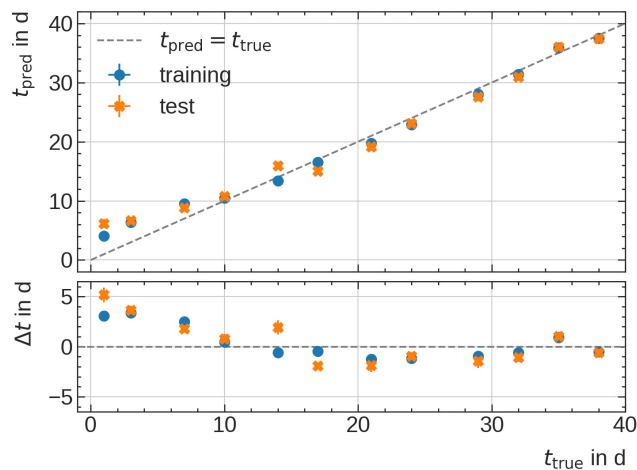
Irradiation Day Estimation

After a successful model selection, the final model is evaluated for its generalisability with the help of the independent test data set. After a training run of about 2650 epochs, the training process is stopped because no significant improvement of the loss function could be achieved in the past 150 epochs. The progression of the loss curve in Figure 5.8 indicates that the training data were not overfitted during the training process.
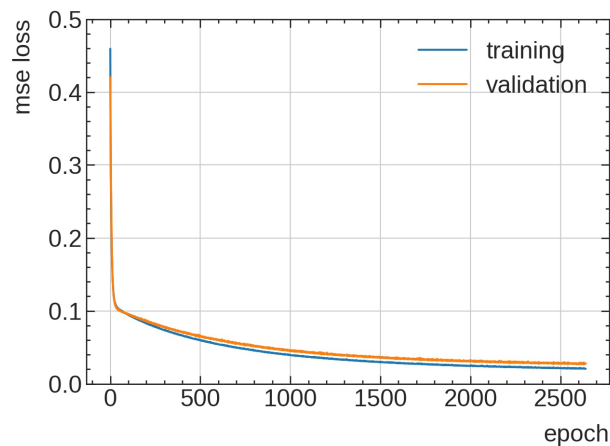
Figure 5.8: Progression of the MSE loss function for training (blue) and validation (orange) data as a function of the training epoch.

Figure 5.9 shows the averaged predictions with the standard error per irradiation day as a function of the true pre-irradiation day. In addition, the relative deviation of the predicted time from the true time is plotted. It can be seen that the training and test data agree within uncertainty on almost all irradiation days. Isolated points in time, such as at $t_{\mathrm{pre}} = [1, 14, 17]\,\mathrm{d}$, show slight deviations between training and test data. The maximum deviation of the predicted values from the true irradiation day is five days. The first week after the detectors' preparation is realistically used to transport the dosimeter to the customer, so this time is not yet considered a monitoring period. After this period, the deviation of the prediction is reduced to a maximum of 3 days. The agreement of the training and test data indicates a good generalisability of the chosen model. The model can predict independent data points comparatively well without memorising the training data.

Figure 5.9: Averaged predicted t_{pre} for each irradiation day with its standard error as a function of the true t_{pre} for the training (blue) and test (orange) data set of the non-tempered glow curve is shown using the DNN model. The bottom plot displays the deviation between the predicted and the true t_{pre}. The uncertainty of the x-axis refers to the averaging of t_{true}.

5.2.2 CNN Approach

The extraction of knowledge-based features from a signal implies a dimensionality reduction and, thus, the loss of information in the raw data. The time-dependent TL signal is passed to a Convolutional Neural Network (CNN) in its raw form to counteract this effect. By training the convolutional filters, features within the signal can be detected without passing them on to the neural network.

In this course, Florian Mentzel modelled a CNN to supplement this study, enabling the

prediction of the irradiation day based on 1-dimensional convolutional filters. The CNN thus makes it possible to identify signal features directly dependent on the irradiation day specifically. However, these features are not directly comparable to the GC parameters that can be extracted from the time-resolved GC as described in Section 2.3.3. The GC parameters are physically motivated and, therefore, easy to understand and interpret. However, it can be seen from the prediction accuracy of the DNN that these parameters are not necessarily best suited as training parameters for a neural network, especially since most of these parameters have no irradiation day dependence. There may be structures within the signal that are neglected by the GC parameters extraction, thus reducing the overall information content.

For training the CNN, the measured training data set was extended to 3000 GCs, as described in Section 4.4, to make the model less sensitive to specific details of isolated GCs in the training data set. Furthermore, the data extension helps to reduce the overfitting of the data and to find a generalised model that describes all GCs equally well. Then, after a dimensional reduction from 2920 to 73 data points with an average pooling, the pre-processing of the training data is finished. Within the model selection framework, the following number of convolutional blocks and convolutional filters, d dropout rate as the regularisation learning rate and batch size was varied during hyperparameter optimisation.

CNN architecture

The final CNN model is shown in Figure 5.10. It consists of two convolutional blocks followed by an average-pooling layer. The convolutional blocks are responsible for the feature encoding of the GCs. Both convolutional blocks consist of two convolutional layers. The number of filters per convolutional layer for the first block is 64 and 32, and for the second block, 32 and 16, with a filter size of 7 per layer. Each convolutional layer is activated using the ReLU function. The second convolutional block is followed by a flattening layer to transform the output from the convolution into a one-dimensional array, which is then passed to one fully-connected dense layer with 256 nodes and a ReLU activation function, which predicts the pre-irradiation day. The output layer is a single-node dense layer with a linear activation, similar to the DNN approach.

To overcome the overfitting of the model, a regularisation using dropout [61] is applied after the flattening and dense layer. A specific number of neurons in the respective layer is deactivated and no longer considered in the subsequent layer. Thus, dropout regularisation forces the network to recognise and learn robust features. The best model performance was achieved using a dropout rate of $r = 0.4$ for the flattening and the dense layer. For the final CNN model, a learning rate of $\alpha = 0.0001$ and a batch size of

4 were chosen by hyperparameter optimisation. Ref. [17] describes the detailed choice of hyperparameters.
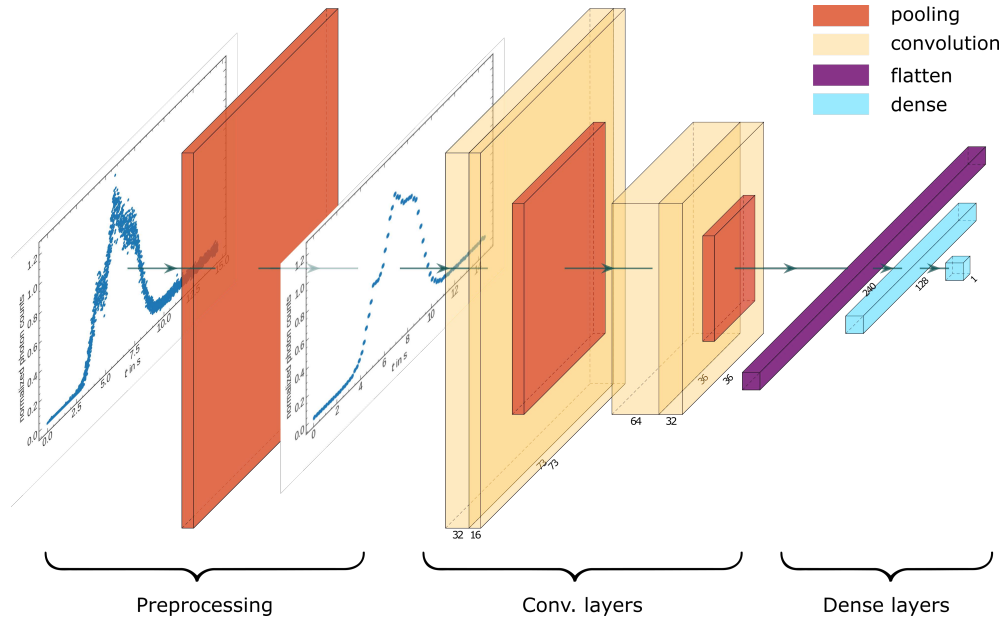
Figure 5.10: Schematic of final 1D CNN model comprising of pooling layers (red), convolutional layers (yellow), a flatten layer (purple) and two dense layers (blue). The input glow curve is shown on the left, the pre-processed glow curve after the first pooling layer. [17]

Irradiation Day Estimation

In assessing the generalisability of the final CNN model, the same test data set is used as for the DNN model, the only difference being that for the DNN, glow curve parameters were extracted from these test data. These GCs are left in their pure form for the CNN, as they were for the training.

Figure 5.11 shows the averaged predictions with the standard errors per irradiation day for the training and test data set as a function of the true irradiation day. It can be seen that the predicted values show a maximum deviation of 2 days from the true irradiation day; only at $t_{\mathrm{pre}} = 4\,\mathrm{d}$, a slightly higher deviation of 3 days can be seen. Furthermore, the predictions for the training and test data set are mostly compatible except for $t_{\mathrm{pre}} = 4\,\mathrm{d}$. There are slight deviations at $t_{\mathrm{pre}} = 4\,\mathrm{d}$ between the training and test data sets. This deviation can be traced back to three outlier GCs in the test data set, which were predicted with high error. The deviations at $t_{\mathrm{pre}} = 15\,\mathrm{d}$ can be attributed to the low number of GCs for this particular irradiation day. Apart from the small deviations, the model shows good agreement between the training and test data within their uncertainties and is thus generalised.
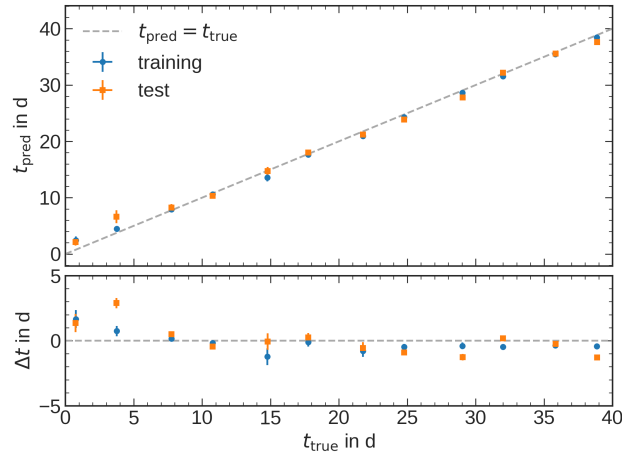
Figure 5.11: Averaged predicted t_{pre} for each irradiation day with its standard error as a function of the true t_{pre} for the training (blue) and test (orange) data set of the non-tempered glow curve is shown using the CNN model. The bottom plot displays the deviation between the predicted and the true t_{pre}. The uncertainty of the x-axis refers to the averaging of t_{true}. [17]

### 5.2.3 Comparison of the DNN and CNN Approach

Let us compare the prediction accuracies of the two applications with each other. The CNN can make a more accurate prediction with a maximum uncertainty of 3 days for all irradiation days within the data set. However, based on the knowledge-based features corresponding to the extracted GCs, the DNN cannot guarantee equal deviations from the true irradiation days for all irradiation times. Especially for early time points, such as $t_{pre} = [1, 3]$ d, the information of the GCs does not provide sufficient capacity to distinguish these days better. The relative deviations from the true irradiation day also do not show any tendency in which periods the prediction of the irradiation day is overestimated or underestimated. Nevertheless, both models, especially the CNN, show that an exposure time estimation of up to 3 days is possible using non-tempered GCs.

Comparing these results with a previously published study that showed that by transforming the GC into the temperature space and extracting relevant GC parameters, a prediction of the exposure day is possible using a univariate approach (GCD) and a DNN approach (GCD+DNN). The univariate approach is represented by a one-dimensional fit function, described by different GC parameters in the temperature space. However, this approach is very limited due to temperature reconstruction. The temperature reconstruction is modelled by an idealised heating curve, which does not represent the individuality of the detectors and their heating behaviour, which results in further uncertainties that must be considered when evaluating the estimated irradiation day. To

improve the univariate estimation, the GC parameters in the temperature space are now used as input parameters for a DNN utilising a multivariate approach. Nevertheless, the prediction is still limited by temperature reconstruction.

All approaches are compared in Figure 5.12. All models' prediction uncertainties are compared, resulting from the 68 % percentile of the absolute deviation between predicted and true values. The lower plot of the Figure shows the improvement of the prediction uncertainty compared to the univariate approach, which represents the origin of the irradiation day prediction. The prediction accuracy of the new DNN approach shows an improvement over the univariate approach of up to 30 % for individual irradiation days. In contrast, the new DNN approach shows no improvement in prediction accuracy compared to the DNN approach based on temperature-reconstructed GC parameters. This can be attributed to the fact that the temperature-reconstructed GC parameters have a greater physical meaning than the parameters in the time-space, which means that they have a greater influence on the determination of the irradiation day.
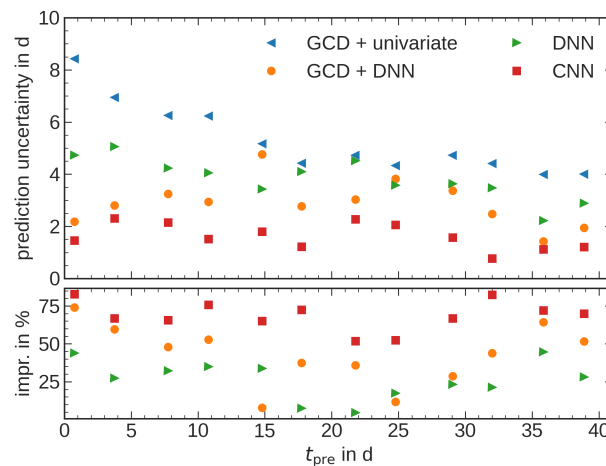
Figure 5.12: Comparison of prediction uncertainties for t_{pre} of the new DNN trained with features derived from the time-resolved glow curve (green triangles pointing right) and the convolutional network model red squares) with the previously presented models: univariate analysis of features from glow curve analysis in temperature space (blue triangles pointing left, reproduced from Ref. [16]), DNN trained with features from glow curve analysis in temperature space(orange circles, reproduced from Ref. [16]). The plot below shows the respective improvement compared to the univariate baseline model in percent. [17]

The choice of knowledge-based features is thus of central importance, according to which the GC parameters in time-space do not contain sufficient information and thus cannot be learned by a DNN alone. Learning the significant features through CNN shows that the prediction accuracy can be improved by up to 70 % compared to the

univariate approach. The mean prediction uncertainty is reduced from $(5.3 \pm 1.3)\,\mathrm{d}$ for the univariate approach and $(2.8 \pm 0.8)\,\mathrm{d}$ for the GCD+DNN approach to $(1.6 \pm 0.1)\,\mathrm{d}$ for the CNN approach.

The two new approaches show that a temperature transformation of the GC is unnecessary to predict the irradiation day; in particular, the CNN can detect features that knowledge-based features could not describe. By omitting the temperature transformation, the complexity of the problem is reduced by neglecting the model-biased uncertainties that arise from the transformation. The independence of a modelled GC model also makes it possible to extend the problem and consider a wide variety of irradiation scenarios, such as multiple irradiations or irradiation with different radiation types.

Even though the CNN could significantly reduce the prediction uncertainty, the selected model is still subject to some limitations resulting from the low statistics in the training data set. The extension of the data set by further measurements or a more optimised data augmentation should not be disregarded. The current model was strongly regularised to prevent the model from memorising the training data too much.

Furthermore, this data set does not represent the GCs measured in the routine operation of the TL-DOS project. This proposed study first shows the proof-of-concept with very successful and promising results. In the following, two measured data sets measured under routine operating conditions are used as the basis for the prediction. However, a further challenge arises here, as the pre-heating step in the read-out deletes additional time-dependent signals, which can impact the prediction of the irradiation day.

5.3 Irradiation Day Estimation on Pre-Tempered Glow Curves

The transfer of the proof-of-concept study to a real-world application performed under the conditions of routine operation leads to a significant limitation of the time dependency of the TL signal. The reason for this is the pre-heating of the detectors during the read-out process. On the one hand, this step makes the dose estimate more robust for the time between the preparation of the dosimeters and the usage by the client. Still, it is precisely this property that is essential for a good irradiation day estimate.

Nevertheless, in the following, the prediction of the irradiation day is learned again using the same Machine Learning (ML) approach (DNN and CNN) based on these pre-heated GCs. First, we study the influence of pre-heating on the prediction accuracy of both approaches for data set 1. Like the non-tempered GC data set, this data set contains single-dose irradiation of $D = 10\,\mathrm{mGy}$. However, to compensate for the loss of

information over time, the number of GCs and irradiation days is greatly increased to obtain larger statistics.

Furthermore, an algorithm for the interpretability of machine learners is presented, which allows insight into the feature importance of a prediction. The interpretability of the model is investigated by using *Shapley values* [62] to estimate the feature significance of the derived GC parameters for the DNN model and the GC features selected by the CNN model for each prediction.

Lastly, the final models are tested on data set 2 to check whether the determination day prediction depends on the irradiated dose.

5.3.1 Irradiation Day Dependency of the Glow Curve Parameters

Before using the extracted GC parameters as input for training the DNN, they are examined for dependencies on the day of irradiation. Figure 5.13 (left) shows a correlation matrix of five exemplary GC parameters with the highest correlations to the irradiation day. It can be seen that there is only a very low correlation between the irradiation day and the GC parameters, with a maximum correlation of $|\rho| = 22\%$ for the mean count. The remaining GCs show no dependence on the day of irradiation and only high correlations of up to $|\rho| = 100\%$ can be seen between the GC parameters. This correlation matrix illustrates the complexity of the problem, as the pre-heating step eliminates the time dependency. It is, therefore, a great challenge for the neural network to establish links between the GC parameters and the irradiation day.
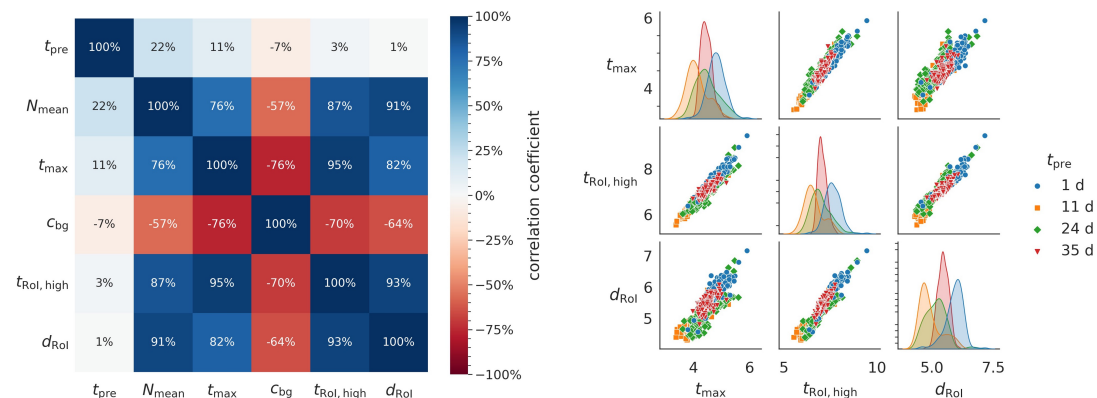
Figure 5.13: Left: Pearson correlation coefficients in percentage between five glow curve parameters of data set 1 with the highest correlations towards the pre-irradiation time t_{pre}; Right: In the non-diagonal, the two-dimensional inter-correlations of three selected glow curve parameters are shown in a scatter plot for various pre-irradiation times of $t_{\mathrm{pre}} = [1, 11, 24, 35]$ d. The diagonal plots show distribution estimations for the individual parameter for the different pre-irradiation times using the kernel density method [60].

Figure 5.13 (right) shows an example of individual GC parameter values distribution for different irradiation days. The kernel densities of the respective parameters are shown on the diagonal. Differences in the distributions as a function of the irradiation day can be seen, but these changes do not follow any recognisable structure. The same applies to the plots of the non-diagonal values. The individual values that can be assigned to individual days of irradiation can be partially differentiated from one another, but here too, no tendency can be recognised; rather, it appears very random.

5.3.2 Fully connected DNN

The extracted parameters for this new data set are also normalised with a robust scaler to reduce the DNN's computational effort. The target vector with the values of the irradiation days is normalised to the latest irradiation day, whereby the values are scaled in a range of [0, 1].

Targeted hyperparameter optimisation is performed based on the previously presented DNN in Section 5.2.1. The architecture remains the same for now; only the batch size, the learning rate and the L2 regularisation are varied. The reason for this is the increased statistics of the data set.

The following hyperparameters were chosen after optimising the final DNN model. The DNN consists of four hidden layers with [64, 128, 32, 16] nodes activated using a ReLU function. The single-node output layer remains the same, which has a linear activation. The batch size is maintained at 32. The learning rate and the L2 regularisation are updated to a value of $\alpha = 0.0005$ and $\lambda = 0.0007$.

During training, the weights were adjusted using the Adam optimiser by minimising the mean squared error loss function. The progression of the loss curve in Figure 5.14 shows no over-fitting of the training data during the training process. A minimisation is achieved for both the training and validation data set. After a training run of about 680 epochs, the training process is stopped because no significant improvement of the loss function could be achieved in the past 150 epochs.

The performance and generalisation of the final model are evaluated on the unbiased test data set from data set 1. The average prediction with its standard error for the training and test data is depicted in Figure 5.15 in dependency of the mean true pre-irradiation day. The predictions for the training and test data sets are in good agreement, confirming that the model can be generalised to an independent data set. The prediction for the training and the test data has a maximum deviation from the true pre-irradiation day of 5 days.
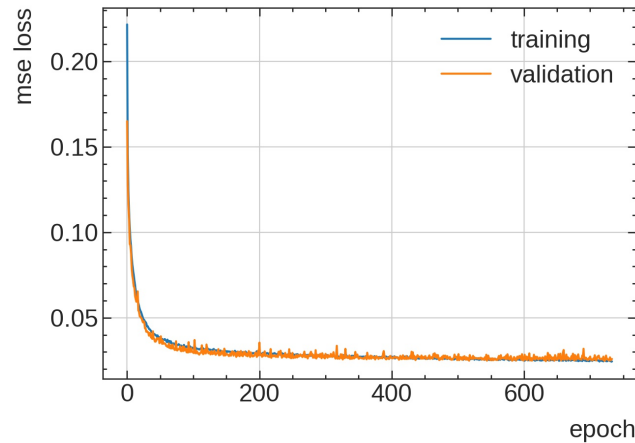
Figure 5.14: Progression of the MSE loss function for training (blue) and validation (orange) data as a function of the training epoch of the DNN using the data set 1. No overfitting of the data can be detected.

In addition, it can be seen that predictions up to a pre-irradiation day of $t_{\text{pre}} = 20\,\text{d}$ are increasingly overestimated, whereas predictions from $t_{\text{pre}} = 20\,\text{d}$ onwards tend to be underestimated. This behaviour was not previously seen in the non-tempered data set. One possible explanation is the complex differentiation of the GCs at different pre-irradiation times—the loss of time information due to the pre-heating leads to the GCs having very similar shapes. Due to the choice of GC parameters, insufficient information is transferred to the DNN to represent the detailed differences in the GCs. As a result, GCs at very early and very late pre-irradiation times show the greatest deviations from the true irradiation day.

Let us compare the prediction uncertainties σ between the DNN trained on non-tempered GC parameters and the pre-tempered ones; see Figure 5.16. We can see that the spread of the uncertainty differs greatly. The mean uncertainty of the DNN pre-tempered is $\overline{\sigma}_{\text{pre-temp}} = (4.9 \pm 1.4)\,\text{d}$, whereas the DNN non-tempered has a lower mean uncertainty of $\overline{\sigma}_{\text{non-temp}} = (3.9 \pm 0.7)\,\text{d}$. Even though both data sets do not show completely identical irradiation times, a tendency of uncertainties can be recognised. The irradiation days $t_{\text{pre}} = [1, 17, 22, 29, 36]\,\text{d}$ the uncertainties of both models are very similar. Nevertheless, the influence of the pre-heating of the detectors during the read-out process can be seen from the uncertainties. It is impossible to estimate the irradiation day for all points in time with the same uncertainty based on the extracted GC parameters alone.

In order to check the influence of the selected GC parameters on the prediction of the pre-irradiation day, an algorithm is presented below that makes it possible to decode the contribution of each GC parameter to the prediction using Shapley values. Based on these values, the selection of GCs for the training process can be evaluated and adjusted.
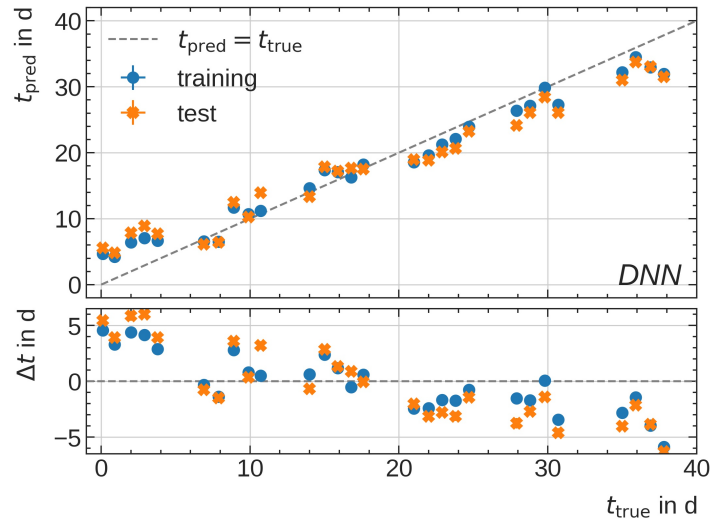
Figure 5.15: Averaged predicted t_{pre} for each irradiation day with its standard error as a function of the true t_{pre} for the training (blue) and test (orange) data set of data set 1 is shown using the DNN model. The bottom plot displays the deviation between the predicted and the true t_{pre}. The uncertainty of the x-axis refers to the averaging of t_{true}.
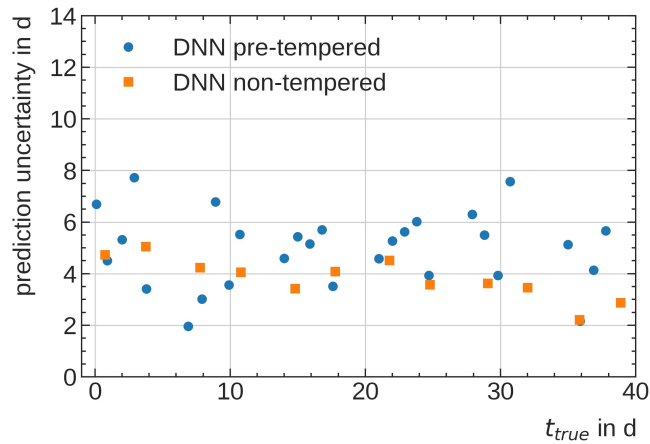
Figure 5.16: Comparison of prediction uncertainties for t_{pre} of the DNN trained with features derived from the time-resolved pre-tempered glow curve (blue) and the previously presented DNN trained with glow curve features from the non-tempered glow curve (orange).

5.3.3 Shapley values for feature interpretation

More and more research areas are being opened that are dedicated to methods of the interpretability of ML to allow more transparency in the reasoning of the prediction choice [63, 64, 65]. These include using Shapley values to understand better and explain the models' predictions. Shapley values make it possible to quantify the contributions of each input parameter to a prediction. Nowadays, it is no longer sufficient to evaluate a

model based on its performance; it is increasingly crucial to ensure the quality of the model and, thus, its explainability.

The origin of the use of Shapley values is in cooperative game theory, which Lloyd Shapley developed in the 1950s [62]. This method is now used in various fields, including political science, economics, computer science, statistics and ML. Examples of the use of Shapley values for the assessment of feature importance are shown in the following References [65, 66, 67, 68]. This method's basic idea is to assign the contributions of individual players who achieve a goal in a cooperative game by forming coalitions. In this way, the contribution of each player in the coalition's gain is determined and, thus, the importance of the player in this game. This principle can thus be applied to the evaluation of input parameters that lead to a prediction of a ML algorithm. Each input parameter thus represents a player, and the prediction is the game's win.

The Shapley value is unique because it satisfies several principles desirable for such an attribution strategy. The most important are highlighted below, and the evidence for each principle is presented in Ref. [69]. If a feature does not contribute to the payout, no payout amount may be assigned to it in the evaluation, corresponding to a value of zero. If features contribute equally to the disbursement, they are assigned an equal contribution. If feature A always contributes more to the payout than feature B, the Shapley value of this feature A must never be lower than that of feature B. To calculate the Shapley value, permutations of the features are considered in every possible order, and then a value is calculated for each permutation that represents the contribution to the payout. The Shapley value is thus the average value of the contributions of a feature over all permutations. Consequently, the Shapley value can be used to show the influence of a feature on the prediction when combined with other features in different feature combinations. This enables the understanding of the prediction and the evaluation of the selected features used for training.

Since there are different implementations of the Shapley values calculation, this study focuses on the **SH**apley **A**dditive exPlanations (SHAP) [65] method. The SHAP library by Lundberg and Lee is used for this; see Ref. [70]. The Shapley values are calculated after successfully training the DNN. Afterwards, the feature's importance can be displayed differently, which will be discussed in more detail below. A major advantage of SHAP is that both a global interpretation of the features and individual interpretations of individual GCs can be sampled.

Global Feature Interpretation

Looking at Figure 5.17 (left), one can see the global importance of the individual GC parameters for the entire data set. Three of the 15 parameters stand out in their

influence; these are $t_{2/4\mathrm{N}}$, d_{RoI} and $t_{\mathrm{RoI,high}}$. The following seven parameters seem to influence the global prediction similarly. The last three parameters, especially $N_{\max}$, seem to have a very small influence on the prediction of the irradiation day.
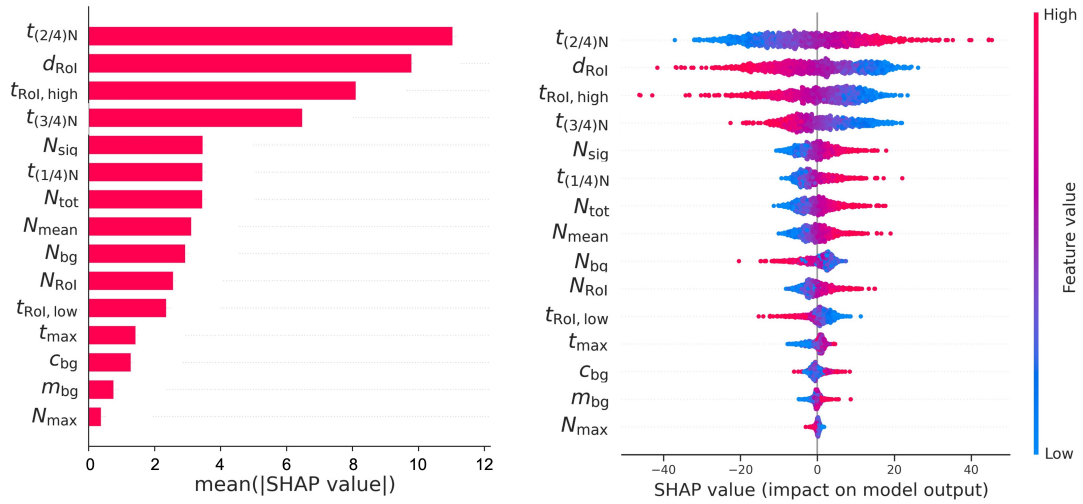

Figure 5.17: Left: The global SHAP feature importance as a bar function of the averaged absolute Shapley values of each glow curve parameter over all given samples. The parameters are sorted according to the average Shapley value, thus the importance of the feature. Right: Summary SHAP plot with all glow curve parameters and their corresponding Shapley value in dependency of their feature value.

The bar plot can also be broken down into individual samples, resulting in the summary plot of SHAP; see Figure 5.17 (right). The summary plot shows all Shapley values for all samples from the data set. The individual feature value for the respective parameter is symbolised with a dot in a certain colour representing the value. Blue dots represent low feature values, and red dots represent high ones. The order of the parameters corresponds to that of the bar plot, which indicates the importance of the parameter. Using this representation, it is now possible to read off the influence of each parameter value on determining the irradiation day. The sign of the Shapley value indicates the direction in which the prediction of the irradiation day is influenced. Positive Shapley values shift the prediction towards later times, and negative values vice versa. The width of the distribution of the Shapley values per GC parameter shows that even small changes in the feature values influence the determination of the irradiation time. In contrast, for parameters $N_{\max}$ or m_{bg}, the feature values hardly influence the prediction. This representation now allows parameters to be evaluated and, if necessary, adjusted or even completely removed from the training process, as they have little influence on the prediction.

Local Feature interpretation

Apart from the global interpretability of the model, Shapley values allow the evaluation of features for individual samples, which is unique compared to other methods of feature interpretation, such as permutation feature importance [71]. Thus, for any set of GC parameters of a single GC, the composition of the prediction can be determined based on the respective influences of the GC parameters. This influence can be visualised in different ways. Figure 5.18 shows an example of the resulting prediction for a GC with the corresponding parameters in the form of a SHAP waterfall plot. The assignment of the Shapley values of each GC parameter shifts the prediction towards earlier or later irradiation times based on the global mean irradiation day prediction, represented by $E[f(x)] = 19.44\,$d. The colour representation simplifies the assignment of whether a feature shifts the forecast in a positive (red) or negative (blue) direction. The final prediction value for the exemplary GC is represented by $f(x) = 3.64\,$d.
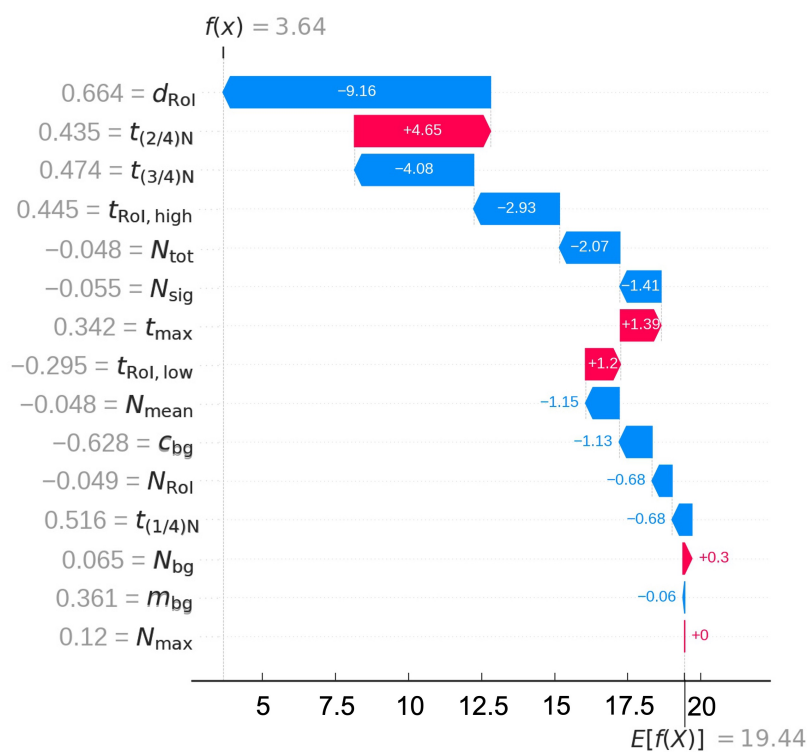
Figure 5.18: Local feature interpretation of the glow curve parameters of one exemplary glow curve with the corresponding contribution to the prediction of t_{pre} as $f(x)$, calculated using the SHAP library. The grey values next to the features represent the feature values for this glow curve sample.

The grey values next to the parameters represent the respective GC feature values as they are transferred to the DNN. These feature values are scaled and must be scaled

back for clarity, which is a limitation of this method. Suppose the feature values are scaled back to the original dimension before the Shapley values are calculated. In that case, the calculation is no longer possible because the values are not comparable with the training dimensions, a limitation that cannot be neglected. Furthermore, it cannot be assumed that if one of the features is removed from the training process, the prediction will be corrected exactly by the difference of the removed feature. When calculating the Shapley values, all features are considered in a coalition, and the prediction is fairly distributed.

Furthermore, it is possible to visualise the composition of the feature importance by utilising a SHAP force plot, see Figure 5.19. This plot also shows the influences of the individual features for a specific GC sample in the same way as the SHAP waterfall plot. Here, too, the prediction is shifted from the overall mean value $E[f(x)] = 19.44\,\mathrm{d}$ based on the Shapley values of each parameter. The final prediction for this sample of GC parameters is $f(x) = 21.60\,\mathrm{d}$. The colour selection is equivalent to the SHAP waterfall plot. Therefore, the choice of representation for interpreting a local forecast is not decisive here but depends on the user's preference.
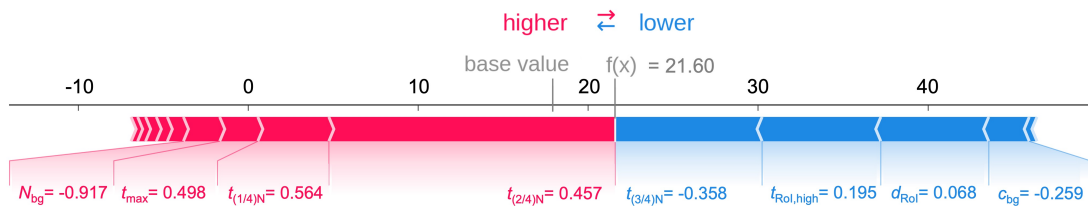

Figure 5.19: Local feature interpretation of the glow curve parameters of one exemplary glow curve with the corresponding contribution to the prediction of t_{pre} as $f(x)$, calculated using the SHAP library. Not all 15 glow curve parameters are depicted due to the lack of space. The values next to the glow curve parameters represent the actual feature value for that specific glow curve.

Both plots clearly show which parameters significantly contribute to the prediction and which do not. For both displayed prediction interpretations, it can be seen that, for example, the GC's quartiles $t_{2/4\mathrm{N}}$ and $t_{3/4\mathrm{N}}$ strongly influence the prediction, regardless of the irradiation day of prediction. These parameters directly measure the relative heights of the individual GC peaks that make up the shape, suggesting that the shape of the GC itself is a very important component for the prediction. In contrast, the maximum number of counts N_{max} and the parameters m_{bg} and c_{bg} characterising the background are almost negligible. This observation is thus consistent with the feature importance of global representation.

5.3.4 Adjustment of the Glow Curve parameter for Training

The consideration of the Shapley values has shown that some parameters, such as N_{max} and m_{bg} have only a small influence on the prediction of the irradiation day, which leads to the question of whether training also influences the DNN if these parameters are not added to the training process. In the following, the DNN is trained with the known architecture and the known hyperparameters for three input parameter sets by removing the parameters N_{max}, m_{bg} and c_{bg} from the 15 input parameters sequentially. Thus, the DNN is trained on 14, 13 and 12 input parameters and the performance of the individual prediction accuracies is compared. Figure 5.20 shows the prediction uncertainties of the individual training runs as a function of the true irradiation day for the different numbers of parameters. The lower plot shows the difference in the uncertainty of the reduced number of parameters compared to the original number of 15.
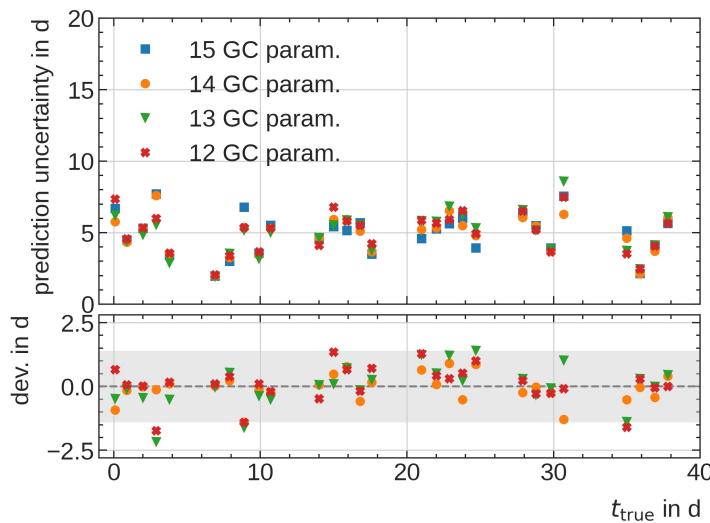
Figure 5.20: Comparison of the prediction uncertainties for t_{pre} of the DNN trained on various numbers of glow curve parameters (GC param.). The lower plot shows the deviation of the prediction uncertainties of the reduced parameters to the original parameter set. The grey area represents the uncertainty band of the standard error of the total averaged prediction uncertainty of the DNN trained on 15 glow curve parameters.

The prediction uncertainty of the training with the reduced number of input parameters deviates by a maximum of $2.4\,\mathrm{d}$. A comparison of the mean values of the absolute deviations also shows that the deviations between the different trainings with different parameter sets agree well within uncertainties.

$$\overline{\sigma}_{15\ \mathrm{param.}} = (4.9 \pm 1.4)\,\mathrm{d}$$

$$\overline{\sigma}_{14\ \mathrm{param.}} = (4.9 \pm 1.3)\,\mathrm{d}$$

$$\overline{\sigma}_{13 \text{ param.}} = (4.9 \pm 1.4)\,\mathrm{d}$$

$$\overline{\sigma}_{12 \text{ param.}} = (4.9 \pm 1.4)\,\mathrm{d}$$

This comparison shows that the reduction of GC parameters does not influence the training performance by removing input parameters within the uncertainties of the DNN and, thus, on the prediction accuracy of the irradiation day. These parameters can thus be kept out of the training process without any consequences in the prediction accuracy. The final DNN model will only be trained on 12 GC parameters in the following.

5.3.5 Feature Importance using 2D-CNN

The DNN with the pre-tempered data set also has strong limitations in prediction accuracy. Considering the feature importance shows that a prediction with a small uncertainty of the irradiation day is not possible based only on the extracted GC parameters. In order to investigate which part of the GC is important for the prediction when using the previously described CNN approach, which predicts the irradiation day based on non-knowledge-based features from the GC. The described study was published in Ref. [18]. To depict these features, the GC must first go through an additional pre-processing step. The previous application of CNN learns GC features in one dimension. The representation of the Shapley values in 1D space is insufficient since the GC is always displayed as a 2D image in routine operation.

Glow Curve Pre-processing

First, the GC is transformed from a 1D array into a 2D matrix. The original 1D GC is normalised to a value range of $[0, 100]$. Then a matrix is created in which an array with 100 entries is created for each measurement point, and the index corresponding to the normalised photon count number is set to the value 1. The remaining entries of the array are set to 0. This results in a GC matrix of the size of 100×1320 pixels, which is shown in Figure 5.21 (left).

As already described in Section 5.2.2, the prediction of the irradiation day does not require the use of all GC bins. Therefore, the GC matrix is reduced to a final size of 25×66 pixels by an average polling with a pool size of $[4, 20]$ before being passed to the CNN. The reduced matrix is shown in Figure 5.21 (right).
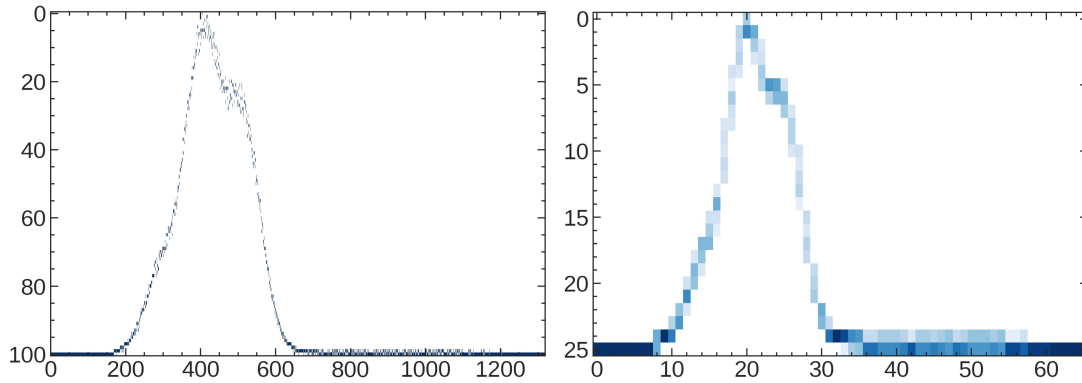
Figure 5.21: Representation of the 2D-transformed glow curve. Left: Originally measured glow curve with 100×1320 pixels. Right: Reduced glow curve using an average pooling with a pool size of (4, 20) pixels and a final glow curve size of 25×66 pixels

2D-CNN Architecture

Following the architecture of the 1D-CNN in Section 5.2.2, a 2D-CNN is now modelled and optimised, providing the best possible prediction accuracy. The final architecture is shown in Figure 5.22. This CNN also consists of two convolutional blocks, two dense layers, and a single-node output layer. Each convolutional block consists of two layers with [64, 32] filters for the first and [32, 16] for the second block. All convolutional layers are activated using the ReLU function and have a kernel size of [3, 3] pixels. After the second layer of each block, a Max-pooling layer is applied to reduce the dimension of the matrix. A spatial-dropout [61] function with a dropping rate of $r_{\mathrm{spatial}} = 0.15$ is included to regularise the model's effective capacity in such a way that the model generalises well to unknown data. A flattening layer flattens the output matrix of the second convolutional block to a 1D array, which is then provided to the dense layers responsible for the irradiation day prediction. The dense layers comprise 64 and 32 nodes and are activated using the ReLU function. Each dense layer dropout with a rate of $r = 0.2$. The output layer is a single-node layer with a linear activation. The Adam optimiser optimises the weights between the nodes by minimising the MSE loss function with a $\alpha = 0.0001$ learning rate and a batch size 16.

Feature Interpretation

The evaluation of the final 2D-CNN is depicted in Figure 5.23. As for the models before, the mean prediction and the standard error of the training and test data are plotted against the true irradiation day t_{true}. The bottom plot shows the deviation from the true irradiation day t_{pre}. It can be seen that the generalisation of the model is ensured, as the prediction for training and test data agree with each other. Most of the predictions per
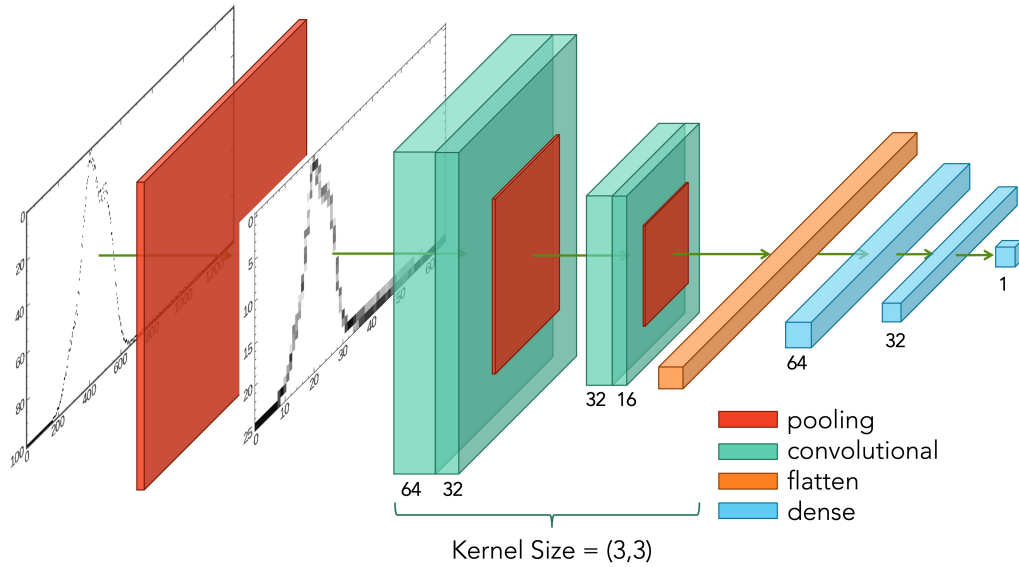
Figure 5.22: Schematic of the final 2D-CNN architecture, including the glow curve pre-processing step, adapted from [18]

irradiation day have a deviation from the true value of up to three days. However, the greatest deviations can also be seen for early irradiation days, which can amount to up to five days for the test data set. These deviations can be attributed to the lower number of samples in the test data set and the high variation of the GCs per irradiation day compared to the training data. This behaviour is also consistent with the observations of Ref. [17]. Also, for the prediction of the 2D-CNN, a tendency can be seen that irradiation days up to $t_{\mathrm{pre}} = 20\,\mathrm{d}$ tend to be overestimated. Above that, they tend to be underestimated. Only a few times deviate from this behaviour, which can be attributed to the variation of the GCs within the irradiation day.

Overall, the CNN approach trained on the pre-tempered and non-tempered data sets shows a significantly better prediction accuracy than the DNN approach. Thus, it supports the assumption that the knowledge-based features do not possess sufficient information to be used alone to predict the irradiation day. Thus, using the 2D-CNN approach, the prediction is no longer limited by the choice of knowledge-based features.

Looking at the prediction uncertainties for the DNN and 2D-CNN approaches in Figure 5.24; the uncertainty was improved with the 2D-CNN for all irradiation days. With a mean total uncertainty of $\overline{\sigma}_{\mathrm{2D\text{-}CNN}} = (3.3 \pm 0.8)\,\mathrm{d}$ for the CNN approach, it is possible to improve the prediction accuracy by $34\,\%$ compared to the DNN with $\overline{\sigma}_{\mathrm{DNN,12\ params}} = (4.9 \pm 1.4)\,\mathrm{d}$. Nevertheless, the accuracy limitations are also clearly noticeable here due to the pre-heating step in the read-out of the detectors. The loss of information over time due to the pre-heating process has a major impact on the differentiability
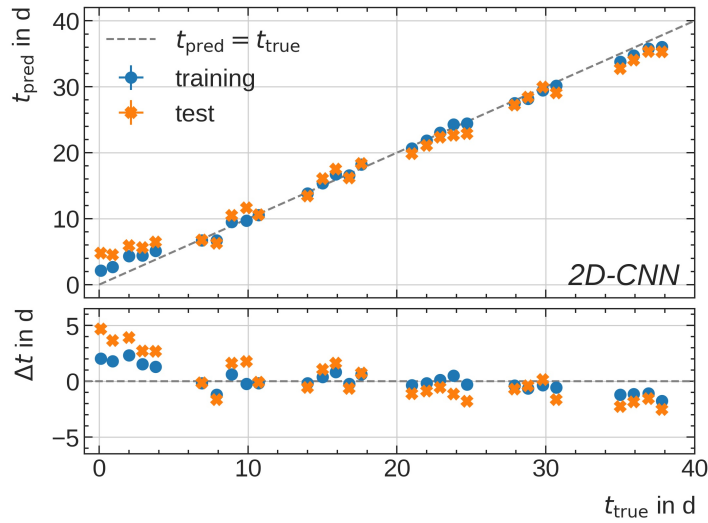
Figure 5.23: Averaged predicted t_{pre} for each irradiation day with its standard error as a function of the true t_{pre} for the training (blue) and test (orange) data set of the data set 1 is shown using the 2D-CNN model. The bottom plot displays the deviation between the predicted and the true t_{pre}. The uncertainty of the x-axis refers to the averaging of t_{true}. Adapted from Ref. [18]

of the GC, which cannot be compensated for by any other measures. Nonetheless, an approximation of the period in which irradiation exposure has taken place with an average accuracy of up to 3 days is a very good result, which can contribute to improving the radiation protection programme of occupationally exposed persons or, in the case of actual exposure, to reconstruct the course and the resulting incorrect actions.
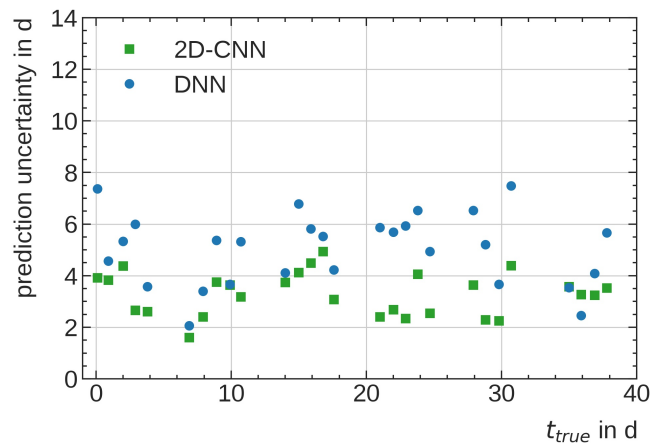
Figure 5.24: Comparison of prediction uncertainties for t_{pre} of the DNN trained with features derived from the time-resolved pre-tempered glow curve (blue) and the 2D-CNN (green).

In order to gain a better understanding of the predictions generated by 2D-CNN, Shapley values were computed using the DeepExplainer function of the SHAP library [70]. For

more detail, see Ref. [65]. Each pixel in the two-dimensional (2D) GC was assigned a Shapley value, which represents the contribution of that pixel to the prediction of the irradiation day t_{pre}. Figure 5.25 displays the Shapley values for two exemplary GC, one for $t_{pre} = 10\,d$ and $t_{pre} = 30\,d$. The choice of colour scale is comparable to the representation of the feature importance for the DNN. The red values correspond to an increase in the prediction value (later within the monitoring period). In contrast, blue values correspond to a decrease in the prediction value (earlier within the monitoring period). The most important pixels correspond to the most relevant features for the DNN prediction. Specifically, the pixels around (15, 15) and (5, 25) correspond to the values of the parameters $t_{(1/4)}$ and $t_{(3/4)}$, which are highly relevant for the DNN model prediction.
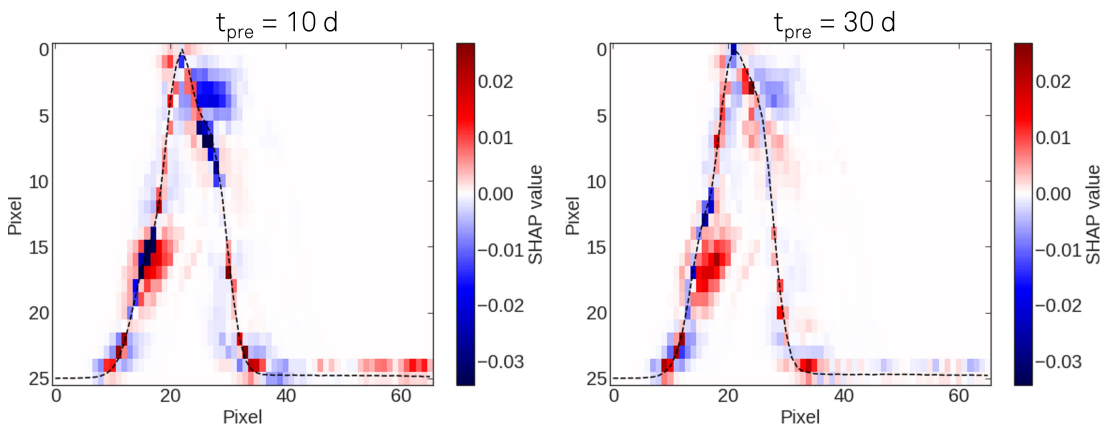
Figure 5.25: Two exemplary pre-processed glow curves at $t_{pre} = 10\,d$ and $30\,d$ with coloured pixels according to the individual pixel Shapley value. The black dashed line represents the glow curve progression. [18]

Also confirmed is the low influence of the data points within the GC, which is described by the GC parameters m_{bg} and c_{bg}. On the other hand, the position of the GC maximum, which corresponds to the parameter t_{max}, seems to have a large influence, as the pixels at and around the GC maximum show high negative Shapley values.

The relative heights of the GC peaks enormously influence the prediction. Since the GC per irradiation day can also vary and be shifted slightly to the left or right, the position and the course of the peak are decisive for the prediction. Considering the colouring of the GC slope, which still indicates GC peak 3, it becomes clear that the prediction would change considerably as soon as the GC shifts to the right. This means that the area around pixels (15, 15) is very dominant. Comparing the GCs shown, these tendencies are present for all irradiation days. For example, the area around (5, 25) for $t_{pre} = 10\,d$ is very strongly coloured blue, which indicates a shift of the prediction towards earlier

irradiation days. In contrast, the same area at $t_{\mathrm{pre}} = 30\,\mathrm{d}$ is only slightly coloured blue, which means that the prediction for this GC is not pushed as much towards earlier irradiation days.

In general, it can be seen that the shape of the GC within the RoI has the most significant influence on the prediction. In conclusion, the coloured areas within the 2D GC can be partially assigned to the knowledge-based parameters but not fully. The 2D-CNN approach can extract relevant features from the GC and predict the irradiation day with an uncertainty of up to 3 days.

5.3.6 Irradiation Day Prediction using 1D-CNN

As shown for the non-tempered data set, using the pure GC in its one-dimensional form as the basis for a CNN is well suited for predicting the irradiation day. By transforming the GC from the 1D space into the 2D space, additional features arise in the GC due to the dimensional extensions, leading to uncertainties in the prediction without significance. Therefore, the 1D-CNN is also investigated for the pre-tempered data set as a potential final model for prediction. For this purpose, the CNN architecture from Section 5.2.2 is used based on the prediction for the non-tempered data set.

Figure 5.26 shows the averaged prediction with the standard error for successfully training the 1d-CNN model on data set 1. The model generalises well; the training and test data predictions agree reasonably. It can be seen that the deviations of the predictions from the true value over the entire time interval amount to a maximum of $\Delta t = 3\,\mathrm{d}$, with the largest deviations for only very early irradiation days, which can be explained by the high variation of the GC in this time range. Even the late irradiation times are very well represented by the 1D-CNN approach, which was not completely possible for the other two DNN and the 2D-CNN approaches. The increased deviations on the early irradiation days are acceptable since these days are usually used for shipping the dosimeters to the customer. Exposure during this period is generally very unlikely.

The comparison of the uncertainties of all presented approaches (see Figure 5.27) shows that the prediction performance of the 1D-CNN corresponds to the one of the 2d-CNN in some irradiation days but offers a lower prediction uncertainty over the entire period. The mean overall uncertainty for the 1D-CNN is $\overline{\sigma}_{\mathrm{1D\text{-}CNN}} = (2.5 \pm 0.6)\,\mathrm{d}$, which is a very good result. However, training a deep neural network on a limited data set can affect the model's robustness. The model cannot sufficiently learn to approximate the relevant features and thus limits the model's prediction accuracy. As a rule, such a deep learning model requires a very large data basis. The main goal of using larger training data sets is to reduce the model's sensitivity towards specific details and features of
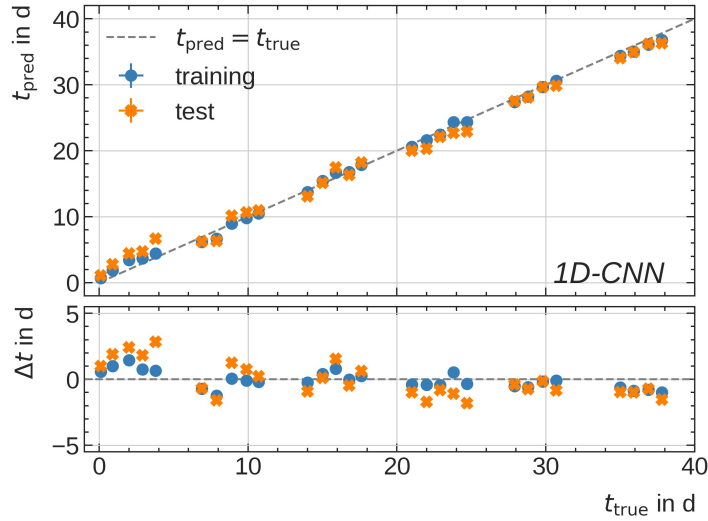
Figure 5.26: Averaged predicted t_pre for each irradiation day with its standard error as a function of the true t_pre for the training (blue) and test (orange) data set of data set 1 is shown using the 1D-CNN model. The bottom plot displays the deviation between the predicted and the true t_pre. The uncertainty of the x-axis refers to the averaging of t_true.

individual training samples and provide a model that can find a generalised model to describe the data equally well without just memorising the existing data.

Since experimental measurement series of a much higher order of magnitude cannot be realised, the measured data set is artificially augmented by shifting the GC, as described in Section 4.4. This artificially augments the training data set to 20k GC. Afterwards, the augmented GCs are only used as training data for the 1D-CNN model. It should be mentioned that the test data set remains untouched to evaluate the generalisation of the model fairly.

The data augmentation reduced the predictive uncertainty of the 1D-CNN, see Figure 5.27 and results in a mean overall uncertainty of $\overline{\sigma}_\text{1D-CNN, augm.} = (1.6 \pm 0.5)\,\text{d}$. This uncertainty is comparable to that of the CNN trained on the non-tempered data set, which is a very good result. Considering that the pre-tempered GC have a very weak irradiation day dependency, it is even more remarkable that the 1D-CNN manages to model the relevant features, allowing such an accurate reconstruction of the irradiation day.

The bottom plot in Figure 5.27 shows the improvement of the prediction uncertainty of all approaches compared to the DNN. The 1D-CNN approach shows by far the largest improvement of 46 % on average. If a data augmentation extends the training data basis, the uncertainty can be reduced by up to 65 % on average.
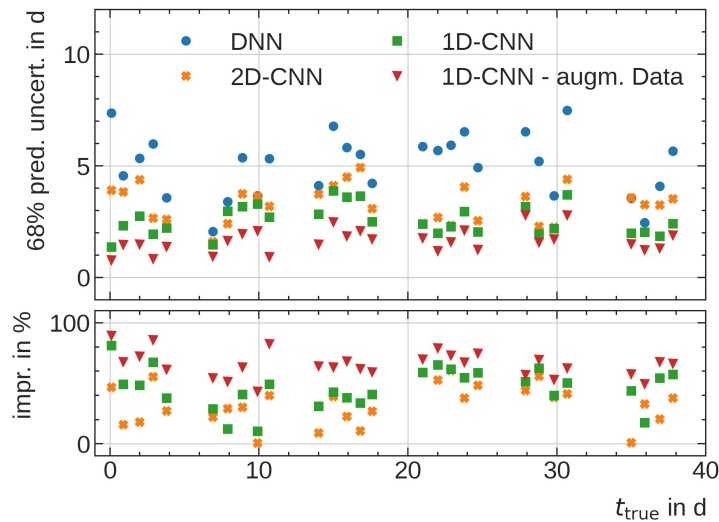
Figure 5.27: Comparison of prediction uncertainties for t_{pre} of all ML approaches trained on the pre-tempered glow curves from data set 1.

5.4 Model Testing on Various Dose Irradiation

So far, the performance of ML applications for irradiation day prediction has been tested on idealised data sets containing TL signals corresponding to an irradiation dose of $D = 10\,\mathrm{mGy}$. However, such a high dose is very unlikely for an occupationally exposed person in a routine dosimetry operation. This high dose was initially chosen to achieve a high signal yield, thus reducing the signal-to-noise ratio and achieving a distinct GC. In order to move a step closer to the real-world application and to test whether the selected models can also be applied to it, data set 2, which contains GCs irradiated with different doses, is used (see Section 4.3). As for the previous data sets, this data set contains GCs irradiated on different days. In addition, the detectors were also irradiated with different doses for each irradiation day in a range of $D = [0.3 - 8]\,\mathrm{mGy}$. The aim is to check how well the ML models can be generalised to GCs of different doses and whether there are any limitations in the prediction accuracy of the models, as was the case for data set 1.

For both approaches, the final models from the previous section are used. No further hyperparameter optimisation is performed, as the aim is now to check whether the existing model can be generalised to a new extended data set. However, as additional information from data set 2 is now included, the respective models are retrained on the new data set to recognise and learn possible new information. In the following, the model evaluation results are described and discussed.

5.4.1 Irradiation Day Prediction using DNN

The averaged predictions after complete retraining are shown in Figure 5.28. The left figure shows the predictions for all GC averaged with the standard error per irradiation day. The right figure shows the predictions additionally divided into the averaged predictions with standard error per irradiation dose and irradiation day, whereby each dose is assigned a certain colour.
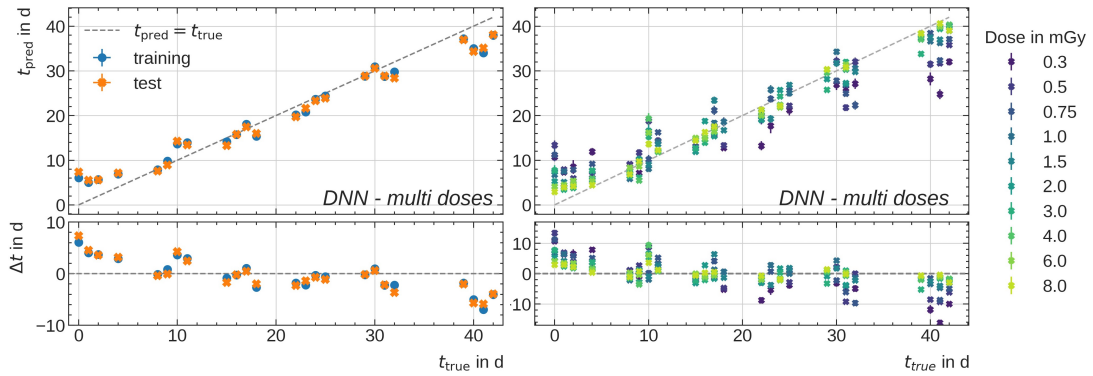

Figure 5.28: Left: Total averaged predicted t_{pre} for each irradiation day with its standard error as a function of the true t_{pre} for the training (blue) and test (orange) data set of the glow curves from data set 2 is shown using the DNN model. Right: Averaged predicted t_{pre} per irradiation dose for each irradiation day with its standard error as a function of the true t_{pre} for the test data set of the data set 2; The bottom plots display the deviation between the predicted and the true t_{pre}. The uncertainty of the x-axis refers to the averaging of t_{true}.

Based on the averaged total prediction, it can be seen that, as with data set 1, the largest deviation of up to $\Delta t = 8\,\mathrm{d}$ from the true irradiation day is also due to very short and very late irradiation days. The deviation within the interval $t_{\mathrm{pre}} = [7, 32]\,\mathrm{d}$ is reduced to a maximum of $\Delta t = 4\,\mathrm{d}$. In order to understand the composition of the averaged prediction value for the individual irradiation days, these are additionally presented as a function of dose. Table 5.1 shows that there is an irradiation dose dependence on the prediction uncertainty. Low doses such as $D = [0.3, 0.5, 0.74]\,\mathrm{mGy}$ show the largest deviations from the true irradiation day over almost all irradiation days, with a maximum deviation of $|\Delta t| = 16\,\mathrm{d}$.

The high deviations can be attributed to the TL signal for low doses. Due to the low signal yield of low dose irradiations, the resulting measured signal is very noisy due to the signal-to-noise ratio. This leads to a difficult distinction of the GC shape depending on the irradiation days. Therefore, the extracted GC parameters are insufficient for a more accurate prediction. Also, the behaviour of underestimating the irradiation day for irradiation days higher than $t_{\mathrm{pre}} = 20\,\mathrm{d}$ is shown, which agrees with the previous observations using data set 1. On the other hand, GCs with higher irradiation doses,

such as $D = [6, 8]\,\text{mGy}$, show small deviations from the true irradiation day with a maximum deviation of $\Delta t = 4\,\text{d}$.

Comparing the uncertainties of the DNNs for data set 1 (single-dose) and data set 2 (multi-doses); see Figure 5.29 (left). In that case, it is shown that the scatter of the uncertainties agrees over the entire interval. A mean uncertainty of $\overline{\sigma}_{\text{DNN, multi-dose}} = (5.0 \pm 1.7)\,\text{d}$ is achieved, a deviation of only $2\,\%$ compared to the single-dose prediction. The averaged prediction uncertainty per radiation day can be divided into individual doses; see Figure 5.29 (right). The dependence of the uncertainty on the irradiation dose is shown. Low irradiation doses show the greatest uncertainties up to $\sigma = 16\,\text{d}$.
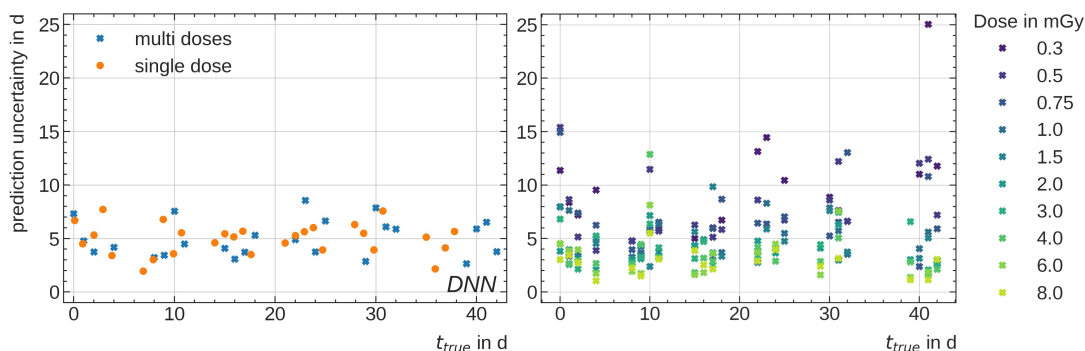
Figure 5.29: Left: Comparison of prediction uncertainties for t_{pre} of the DNN trained with features derived from the time-resolved pre-tempered single dose glow curves (orange) and multi-doses glow curves (blue). Right: Irradiation day prediction uncertainties in dependence of the irradiation dose.

There is an outlier at a dose of $D = 0.3\,\text{mGy}$ and a $t_{\text{pre}} = 41\,\text{d}$ with an uncertainty of $\sigma = 25\,\text{d}$, which can be attributed to the low statistic in the test data set, where only 6 GC per irradiation dose and irradiation day are used, in addition to the very complex differentiation of the GC. With increasing irradiation dose, the uncertainties tend to decrease; see Table 5.1 for all averaged prediction uncertainties per irradiation dose. For high doses of $D = [4, 6, 8]\,\text{mGy}$, uncertainties in the range of $\sigma = [2, 5]\,\text{d}$ are shown in Figure 5.29 (right). However, there are also isolated outliers for some irradiation days, such as $t_{\text{pre}} = 10\,\text{d}$ or $t_{\text{pre}} = 17\,\text{d}$, which can also be attributed to the and high variance of the GC shapes.

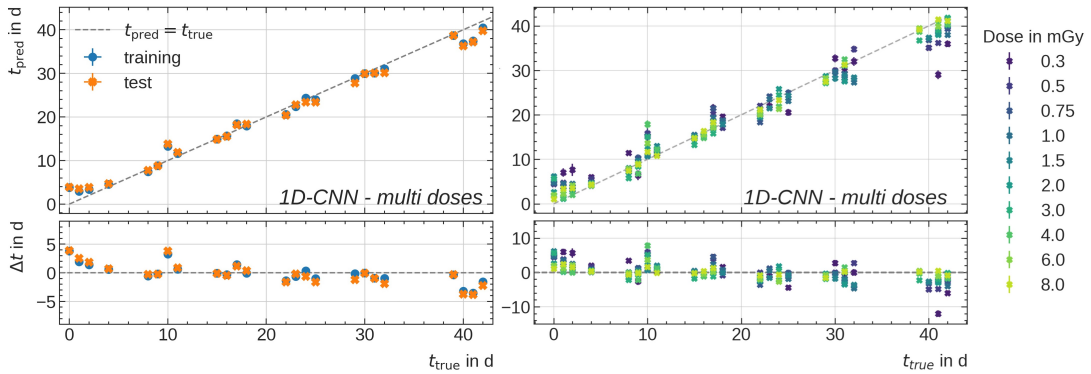### 5.4.2 Irradiation Day Prediction using 1D-CNN

The 1D-CNN is also retrained on GC from data set 2, and the resulting predictions are shown in Figure 5.30. As for the DNN, the left plot shows the total averaged prediction with the standard error over all GC per irradiation day. The right plot shows the split averaged predictions per irradiation dose and day. The average predictions in Figure

Table 5.1: Averaged prediction uncertainties with the standard error per irradiation dose for the DNN and 1D-CNN approach.

| Dose in mGy	avg. prediction uncertainty in d	
	DNN	1D-CNN
0.3	9.3 ± 4.7	7.8 ± 4.3
0.5	8.0 ± 3.2	5.4 ± 2.3
0.75	6.7 ± 3.0	4.7 ± 1.6
1	5.1 ± 1.7	4.1 ± 1.4
1.5	4.5 ± 1.9	3.8 ± 1.4
2	3.8 ± 1.3	3.2 ± 1.9
3	4.1 ± 1.7	3.4 ± 1.6
4	3.6 ± 2.4	3.1 ± 1.6
6	3.3 ± 2.0	2.7 ± 1.0
8	2.7 ± 1.0	2.7 ± 1.1

5.30 show an improvement in the prediction accuracy as expected. Even the deviations for short and later irradiation days show a maximum deviation of $\Delta t = 4$ d. and the predictions for the remaining days are very close to the true value. An improvement in the prediction accuracy compared to the DNN is also shown when considering individual irradiation doses. The low irradiation doses show a reduced deviation of up to $\Delta t = 12$ d, in particular for $D = 0.3$ mGy. The remaining irradiation doses show average deviations up to $\Delta t = 8$ d. The high doses $D = [4, 6, 8]$ mGy show small deviations up to $\Delta t = 3$ d.

Figure 5.30: Left: Total averaged predicted t_{pre} for each irradiation day with its standard error as a function of the true t_{pre} for the training (blue) and test (orange) data set of the glow curves from data set 2 is shown using the 1D-CNN model. Right: Averaged predicted t_{pre} per irradiation dose for each irradiation day with its standard error as a function of the true t_{pre} for the test data set of the data set 2; The bottom plots display the deviation between the predicted and the true t_{pre}. The uncertainty of the x-axis refers to the averaging of t_{true}.

The prediction uncertainties in Figure 5.31 shows no significant change in prediction accuracy compared to the training on data set 1. The overall averaged prediction

uncertainty for the 1D-CNN based on data set 2 is $\overline{\sigma}_{\text{1D-CNN, multi-dose}} = (3.5 \pm 1.2)\,\text{d}$, corresponding to a deviation of $25\,\%$ compared to data set 1. However, this deviation does not mean that the performance of the 1D-CNN is worse compared to the data set 1; it is only limited by the prediction uncertainties resulting from the GC with low irradiation doses.
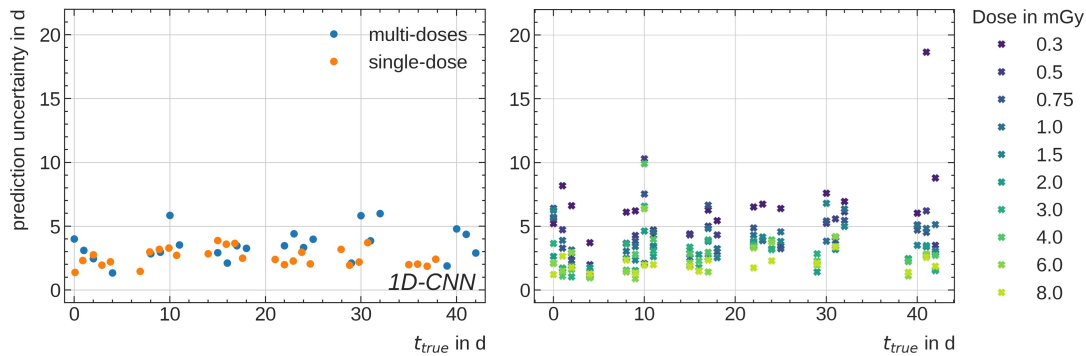
Figure 5.31: Left: Comparison of prediction uncertainties for t_{pre} of the 1D-CNN trained on the time-resolved pre-tempered single dose glow curves (orange) and multi-doses glow curves (blue). Right: Irradiation day prediction uncertainties in dependence of the irradiation dose.

In the right plot of Figure 5.31, it is clear that GC with low irradiation doses can only be predicted inaccurately due to the high signal-to-noise ratio within the GC and the additional dimension reduction by rebinning the raw measurement signal within the pre-processing of the GC. Because it is difficult to differentiate the TL signal shape from the raw measurement signal, it is difficult to distinguish between the different irradiation days. Due to the dimension reduction during the pre-processing of the GC, relevant features can become blurred, making them more difficult to distinguish depending on the day of irradiation. To be able to predict better, the measurement procedure of the signal would first have to be optimised in order to create a reduced signal-to-noise ratio. Again, the trend that the higher the doses, the lower the prediction uncertainty is shown in Table 5.1. Comparable outliers are shown, which can be attributed to the variation of the GC in the respective data set.

5.5 Conclusion

Previous studies, such as Ref. [13, 16], have already shown that the irradiation day can be reconstructed based on knowledge-based features within the GC. For this purpose, a univariate method was first used, which models an adjustment function based on the temperature-reconstructed GC, which describes the course and composition of the GC. A second approach, a multivariate method, uses the GC parameters resulting of the

model function from the univariate approach as training parameters for a neural network to model correlations of the GC parameters on the irradiation day and thus predict it. However, the temperature reconstruction is subject to some limitations that make it difficult to transfer the application of the prediction to arbitrary irradiation scenarios. The temperature profile regulates the model function of the GC in temperature space during the read-out process. It is also dependent on the material of the detector, which introduces additional uncertainties in the determination of the GC parameters since an idealised heating process cannot be reproduced due to the individuality of the individual detectors.

In order to counteract these limitations and uncertainties, GCs in time-space were considered in this study as a basis for a possible prediction—the loss of temperature reconstruction results in the loss of physically relevant information that characterises the GC. Nevertheless, GC parameters can also be extracted from the GC in time-space, which can adequately characterise the GC shape. The presented study shows the successful implementation of a proof-of-concept for reconstructing the irradiation day using ML approaches. The averaged prediction uncertainties are summarised in Table 5.2.

Table 5.2: Averaged prediction uncertainty per considered data set and respective ML approach.

Data Set	DNN Approach	CNN Approach
non-tempered	$(3.8 \pm 0.7)\,\mathrm{d}$	$(1.6 \pm 0.1)\,\mathrm{d}$
pre-tempered single-dose	$(4.9 \pm 1.4)\,\mathrm{d}$	$(2.5 \pm 0.6)\,\mathrm{d}$
pre-tempered single-dose + data augmentation	-	$(1.6 \pm 0.5)\,\mathrm{d}$
pre-tempered multi-doses	$(5.0 \pm 1.7)\,\mathrm{d}$	$(3.5 \pm 1.2)\,\mathrm{d}$

First, the investigation starts with a highly idealised view of the GC. The TL-DOS detectors are irradiated with a $D = 10\,\mathrm{mGy}$ for 12 irradiation days and stored using regulated climatic conditions. Subsequently, the detectors are read out, whereby the pre-temperature step is omitted from the read-out process not to eliminate additional time-dependent information within the GC.

Using a fully connected DNN trained on the extracted GC parameters in time-space can determine the irradiation day with an average uncertainty of $\overline{\sigma}_{\mathrm{DNN,\ non\text{-}temp.}} = (3.8 \pm 0.7)\,\mathrm{d}$. The consideration of the GC parameters as a function of the irradiation time indicates that the choice of the GC parameters for the training is insufficient to describe the differences in the GC on different irradiation days. In order to extend this reduced parameter space, a CNN model is exploited to detect features within the entire GC using convolution filters. These filters extract features within the GC, which further accelerates the pre-processing of the data and thus avoids possible uncertainties

arising from GC modelling. The uncertainty of the irradiation day prediction can be reduced to $\overline{\sigma}_{\text{CNN, non-temp.}} = (1.6 \pm 0.1)\,\text{d}$ using CNN. The CNN approach shows that using knowledge-based features is unnecessary to predict the radiation day accurately.

Since this preliminary study contains GCs that are easier to differentiate from each other due to the neglect of the pre-tempering step and are therefore not comparable with GCs from routine dosimetry operation, the second step of the data basis is replaced by pre-tempered GCs that correspond to the read-out conditions of routine operation. Upon visual inspection, these GC show hardly any dependencies on the irradiation day, which is also the intention of the pre-heating. This makes it much harder for the DNN or CNN to extract relevant correlations to predict the irradiation day accurately. Nevertheless, a DNN and a CNN approach are modelled and trained on this new pre-tempered data set.

The prediction uncertainty of the DNN trained on the extracted GC parameters shows an average uncertainty of $\overline{\sigma}_{\text{DNN, pre-temp.}} = (4.9 \pm 1.4)\,\text{d}$. The prediction accuracy is expected to be worse than the non-tempered GC due to the loss of information. However, since the individual GC parameters do not show significant time dependence either, which GC parameters have the greatest influence on the prediction to possibly adjust the GC parameters in the training process is checked. Furthermore, this offers the possibility to evaluate the model's trustworthiness. In this course, Shapley values [62] are calculated using the SHAP library [70], which provides an interpretability of the models. It becomes apparent that some GC parameters, such as the maximal count number or parameters that characterise the background signal, only contribute slightly to the prediction of the irradiation day and can therefore be excluded from the training process without changing the model's prediction accuracy.

However, the extracted GC parameters are insufficient for a more accurate prediction for the non-tempered data set. Therefore, the CNN approach is applied to the measured GC. To take the application a step further and to highlight the feature importance within the GC itself, which is useful for a future routine operation, the GC is passed to the CNN as an image (2D-GC). This also enables the SHAP library to colour relevant areas in the 2D-GC and, thus, to obtain an interpretation of the model. The representation of the feature importance in 2D space shows that the knowledge-based features are well represented, but these alone are not sufficient to achieve an accurate irradiation day prediction. The 2D feature importance map shows that the entire GC shape is crucial for the assignment to an irradiation day.

The transformation of the GC into 2D space provides uncertainties due to the dimensional expansion caused by creating features without significance. The transformation is only beneficial for representing the GC feature importance and does not improve the prediction accuracy of the irradiation day. Therefore, a 1D-CNN is chosen as the final approach

to provide the irradiation day prediction with an average prediction uncertainty of $\overline{\sigma}_{\text{1D-CNN, pre-temp.}} = (2.5 \pm 0.6)\,\text{d}$, which is worse by one day compared to the non-tempered data set, but still a very good result due to the complexity of the problem under consideration. Such a prediction makes it possible, in the case of an exposure, to narrow down the period of an incident considerably and thus identify and reconstruct the possible cause. In this way, occupational radiation protection can be optimised.

The measured data set is extended again by not only considering a dose of $D = 10\,\text{mGy}$, which is very untypical for routine monitoring, but also by considering GC for more realistic dose contributions, such as $D = 0.3\,\text{mGy}$ up to $D = 8\,\text{mGy}$. It is shown that the irradiation dose influences the prediction uncertainty for both the DNN and CNN approach (see Table 5.1). The higher the irradiation dose, the less the prediction uncertainty. Nevertheless, the prediction uncertainty $\overline{\sigma}_{\text{DNN, multi-dose}} = (5.0 \pm 1.7)\,\text{d}$ for the DNN using the extended data set is comparable to the single-dose approach. The prediction uncertainty of the 1D-CNN $\overline{\sigma}_{\text{1D-CNN, multi-dose}} = (3.5 \pm 1.2)\,\text{d}$ increases by one day, which can be attributed to the increased prediction uncertainties for low doses. Due to the higher signal-to-noise ratio within the TL signal towards lower irradiation doses, it becomes more difficult to estimate the actual GC shape, despite the pre-processing of the GC by using pooling to reduce the noise within the GC.

Using an augmented data set shows a performance improvement of the 1D-CNN and a reduction of the prediction uncertainty to $\overline{\sigma}_{\text{1D-CNN, augm.}} = (1.6 \pm 0.5)\,\text{d}$. The use of a larger data set increases the robustness of the model. Training on additional augmented or noisy GCs reduces the model's overfitting probability. Instead, it is able to find a more generalised model which describes the data well.

The planning and performing of large measurements takes a lot of time, and the number of measurements is limited by the time it takes to readout a detector. Increasing the statistics using positional shifts of the GCs enormously impacts the model performance. In the following, the question is answered whether augmenting the measured data with artificially generated GCs using generative ML approaches, such as the generative adversarial neural networks (GANs), also positively impacts prediction accuracy. The generative approach presented in the following Chapter exploits the existing measured GC parameter space. It generates GCs based on interpolation in the parameter space that increases the amount of information for training. In this way, existing measured data sets can be extended by adding generated GCs to irradiation times that were not considered during the measurement. Furthermore, this approach can potentially be applied to expanding the measurements of various irradiation scenarios.

6   Glow Curve Generation using GAN

The following chapter describes the implementation of a Generative Adversarial Network approach [72] for generating GCs that will be used to expand the data basis for predicting the irradiation day and possible further irradiation scenarios. First, the architecture of the chosen model is presented. Then, the generated GC are analysed and evaluated as training data.

6.1 Wasserstein GAN Architecture

The principle of a GAN is based on the interplay between two neural networks, a *generator* trained to generate artificial GCs and a *discriminator* trained to distinguish the generated GCs from the true measured GCs. GCs from data set 1 4.3 are the ground truth for the discriminator, first extended by a data augmentation to provide the discriminator with a high degree of statics for learning the GC features. In the training process, the generator tries to generate GC from a noise input vector.

For this study, a conditional *Wasserstein GAN* [73, 74] is trained, which allows GC to be generated for the respective condition based on additional requirements, in this case, different irradiation days. With the help of the Wasserstein distance [75], the discriminator is trained to distinguish measured GCs from ones created by the generator. Subsequently, the Wasserstein distance is passed on to the generator to adjust its weights and thus optimise the generation process and make the generated GC more similar to the true ones. After a successful training process, the goal is that the generator can generate GCs that are indistinguishable from the measured ones.

The 1D-CNN approach provides the best results for the irradiation day estimation by learning relevant features within the GC. Therefore, it is chosen as the underlying model for the GAN's generator and discriminator. Since the training process of a GAN is very computationally intensive and hyperparameter optimisation, as previously performed, is not possible due to the two networks training against each other, the choice of hyperparameters and, thus, the final structure is based on empirical arguments.

The final architecture of the conditional WGANs is shown in Figure 6.1. The generator consists of an input layer to which a noise vector of size 364 is passed. The input layer is followed by four convolutional layers with additional upsampling of the GC to the

desired GC size. The filter size of the convolutional layers is composed of (128, 128, 128, 64) filters with the size of (2, 3, 5, 5) per layer. Each convolutional layer is activated by a ReLU function and normalised using batch-normalisation with a momentum of 0.8 [76]. After each convolutional layer, a dropout function is also included with a dropout rate of 0.05 to regulate the training progress. A fifth convolutional layer with one filter and a size of 9 combines the most important features from the previous layers. Since the size of the generated GC after the last convolutional layer is 142 and thus does not correspond to the size of the measured pre-processed GC, it is then shortened to 132 entries.

The discriminator has an input layer containing the GC in a size of 132 entries, followed by three convolutional layers with (64, 64, 128) filters with the size of (7, 5, 3) per layer, activated using the ReLU function. Then the output of the last convolutional layer is flattened and passed to the single node dense putout layer, which discriminates the GC.

The training process of the GAN is performed batch-wise, whereby the discriminator is first trained on several batches compared to the generator before the generator is further trained. This ensures the feedback from the discriminator is of strong quality. In addition to the input, the generator and the discriminator receive an additional conditional input, providing information about the irradiation day. This condition allows the discriminator to learn to distinguish between true and false GCs and assign them to an irradiation day.

After each training batch run of the generator, the generated GCs are passed to the discriminator, which then evaluates the quality of the GC using the Wasserstein distance. The calculated Wasserstein distance is afterwards passed back to the generator via backpropagation. The weights of the GAN are referred to as gradients and are regulated with the help of the *Gradient Penalty (GP)* [77], which is a regularisation technique used specifically in the context of WGANs. This technique improves the stability and convergence of the GAN training. The GP regulates the gradients, which are increasingly weighted during training. This effect is called *Exploding Gradients* [78]. The steady increase in gradients has the consequence that the GAN becomes unstable and the performance of the GAN decreases, as some features are given far too high weight.

Typically, these gradients are limited by *weight clipping* [79], whereby gradients that exceed a certain value are reset to the limit value. Weight clipping regulates the stability of the GAN but not its final performance. However, choosing suitable clipping values leads to further problems explained in detail in Ref. [77]. GP adds a regularisation term to the loss function to normalise the gradients of the discriminator to a value of 1. If gradients deviate from this value, the network is penalised, and gradient optimisation occurs. This form of regulation increases the complexity of the GAN, which makes the
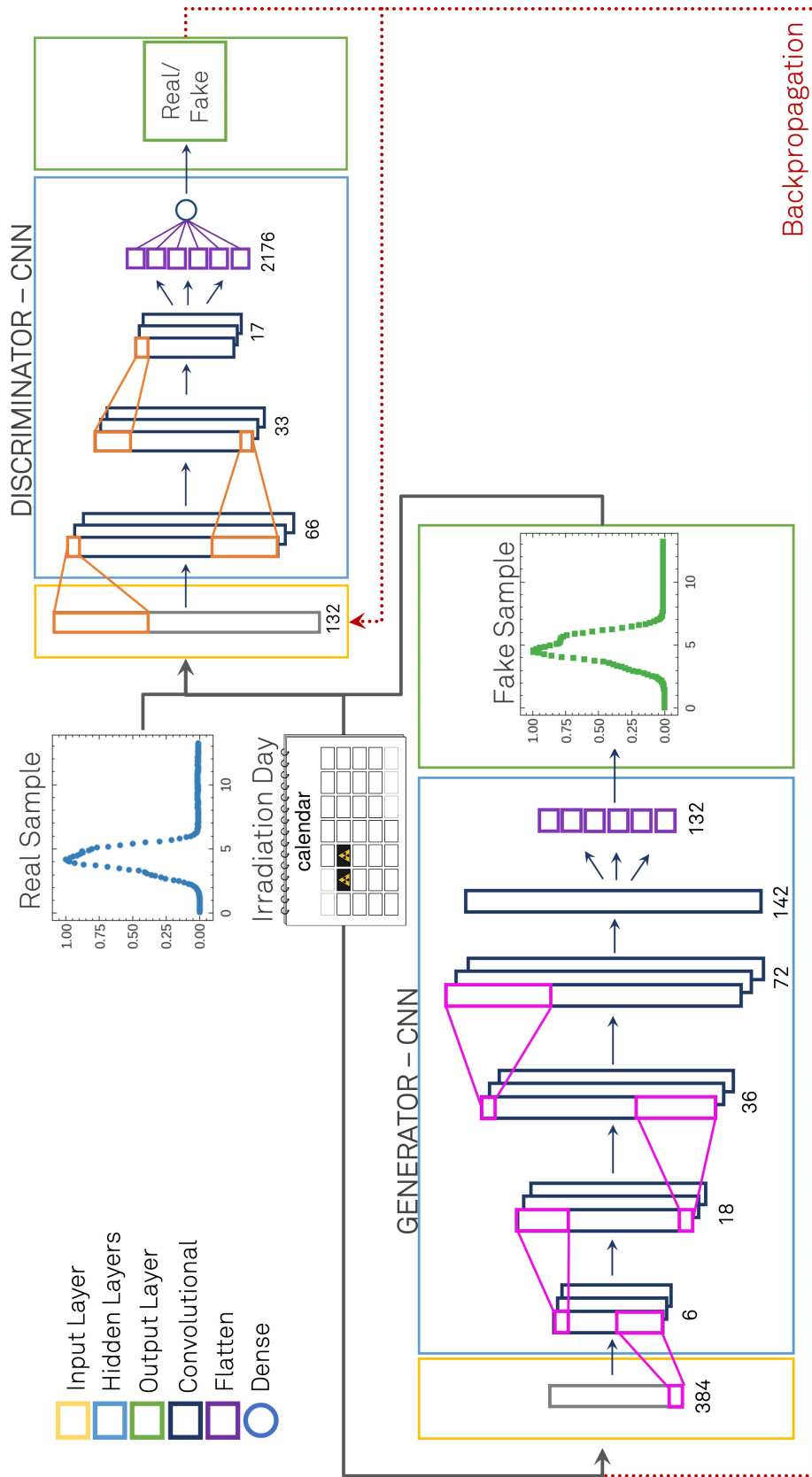
Figure 6.1: Schematic GAN architecture consisting of a generator and a discriminator.

network more stable, but also increases the duration of the training per batch. The GAN is trained as long as the discriminator can distinguish between the generated and true GCs so that no specific training duration can be set.

6.2 Training and Evaluation of the GAN

Since the training process of a GAN is not comparable with that of another regression or classification algorithm, the subsequent performance evaluation requires more effort due to the two opposing networks being trained [80, 81]. First of all, no general statement can be made about the duration of the training. The goal is to achieve the so-called *Nash equilibrium* for the interaction of the two networks. Nash equilibrium describes a state where each network makes the best decision, considering the other network's decision. Therefore, the generator and discriminator must be coordinated so that both continue to achieve the maximum profit through their chosen strategy. This means that the generator can generate GCs that deceive the discriminator. Still, simultaneously, the discriminator has found a strategy to detect fake GCs. Achieving this balance is not always easy, as problems such as *Mode Collapse* or model instability can occur due to the complexity of the individual networks. [82, 83, 84] Mode Collapse occurs when the generator can no longer generate GCs that differ from each other, which means that after each training run, the same GCs are generated by the generator repeatedly. This problem is regulated at this point by the Wasserstein Distance. In order to prevent instability, the respective networks were designed in a very simplified way since the amount of training data is limited.

Observing the loss function is insufficient for the performance evaluation of the GAN. Therefore the accuracy of the discriminator is analysed in addition to the Wasserstein distance. Furthermore, a metric is introduced to evaluate the generated GC using the 1D-CNN from Section 5.3.6 to show whether the generated GC can be assigned to the true irradiation day. It is expected that the accuracy of the discriminator will saturate around 50% during the training process, as it should become increasingly difficult for the discriminator to distinguish between real and fake GC. The GAN is trained for 1000 epochs, where one epoch is the iteration of all data points from the data set at least once through the model.

In preparation for the training data for the GAN, the statistical variation of the individual GC per irradiation day is considered first. For example, all GCs for four different irradiation days are shown in Figure 6.2. It is immediately noticeable that the GCs per irradiation day vary greatly. On the one hand, the GC's width and the GC's RoI start

and end point vary greatly. At the same time, differences in the GC shape are very small or hardly noticeable.
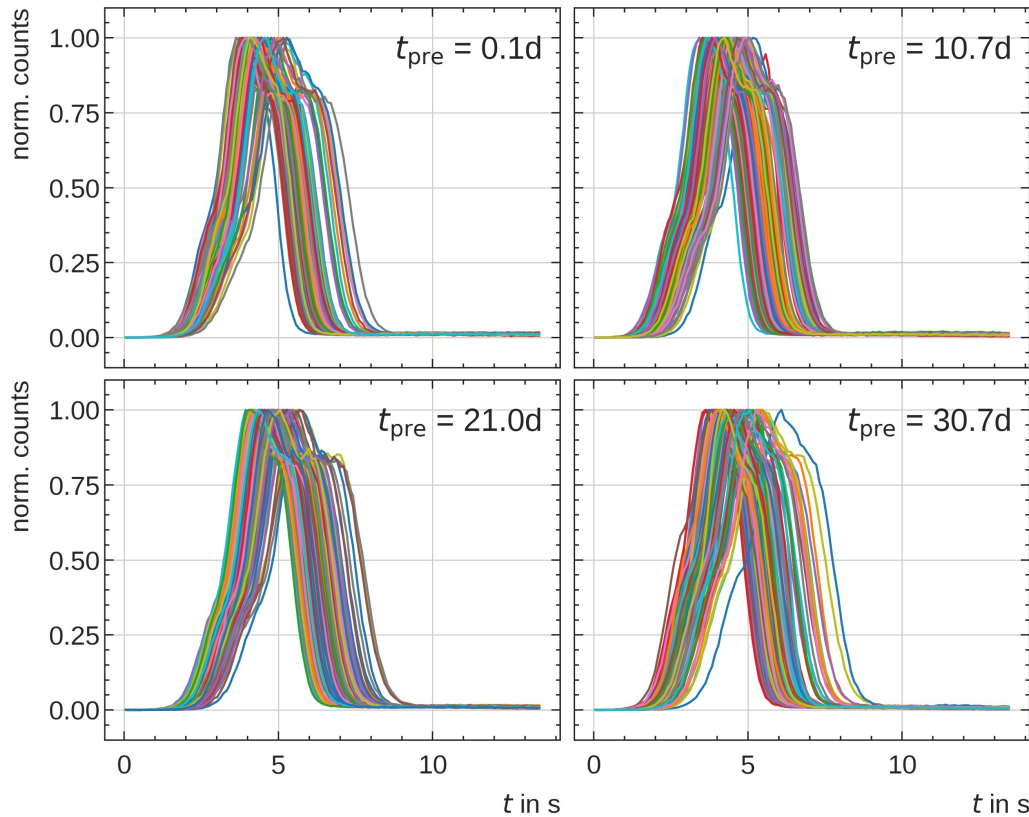
Figure 6.2: Depicted are glow curves of the data set 1 corresponding to the irradiation days $t_{\mathrm{pre}} = [0.1, 10.7, 21.0, 30.7]\,\mathrm{d}$. 150 measured glow curves are plotted for each t_{pre}.

Due to the limited data basis for the training of the GAN, the training data are first augmented to a total of 20k GC, as described in Section 4.4. Then the GAN is trained for 1000 epochs. Figure 6.3 shows the course of the Wasserstein loss for the generator and discriminator. It can be seen that both the generator and the discriminator run into saturation in the course of the training. The accuracy of the discriminator first settles around a value of $60\,\%$ but starts decreasing again towards later epochs, which suggests that the discriminator is possibly not yet fully trained. However, due to the high computing time, the training was limited to 1000 epochs for the time being, which can be increased at any time. However, if the training is too long, there is a risk that both the generator and the discriminator will diverge, and it is uncertain whether the GAN will stabilise again during the training.

Since it is not obvious from the loss function which training epoch will generate the best GC, a metric using the 1D-CNN trained on augmented data, as presented in Section 5.3.6,
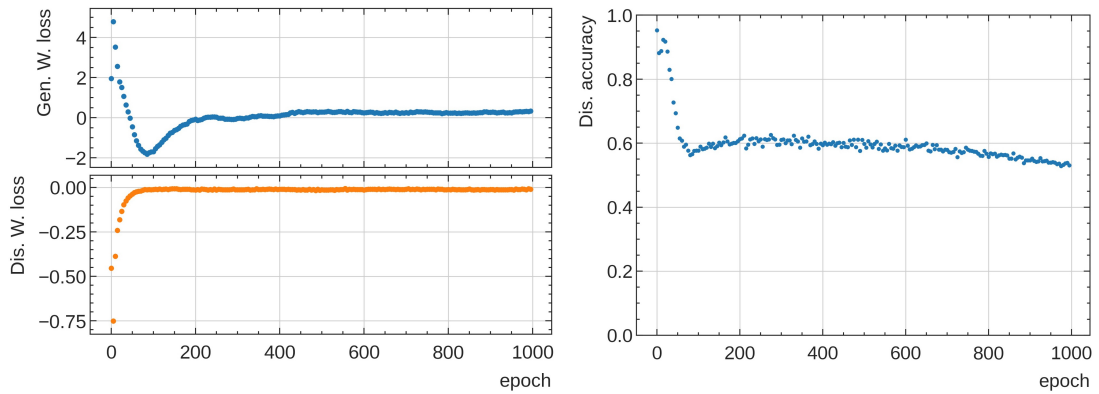
Figure 6.3: Training process of the GAN. Left: The course of the Wasserstein loss function for the generator and discriminator is shown. The discriminator shows rapid saturation around 0, whereas the generator requires more training epochs to converge. Right: The curve of the discriminator accuracy is shown as a function of the training epoch with saturation around 60 %.

is used to predict the irradiation day. This model is trained to assign the glow curve and its characteristics to an irradiation day with a resulting mean prediction uncertainty of $\overline{\sigma}_{\text{1D-CNN, augm.}} = (1.6 \pm 0.5)\,\text{d}$. It is, therefore, very suitable for evaluating the generated GC. Since each irradiation day has a slightly different prediction uncertainty, this is also considered in evaluating the generated GC. For this purpose, 150 glow curves are generated for every tenth training epoch, whose irradiation day is determined by the 1D-CNN.

The aim is to identify a training epoch that allows GCs of the same quality to be generated for each day of irradiation. This means that the predicted irradiation day of the generated GCs using the 1D-CNN should deviate as little as possible from the true irradiation day. For this purpose, the Mean Absolute Error (MAE) of the differences between the predicted and true irradiation day is first calculated over all irradiation days and displayed as a function of the training epoch, see Figure 6.4. This metric now allows filtering for the epochs that assume a minimum value. The five best epochs are marked with red circles in Figure 6.4. It can be seen that these are distributed over the entire training course. This behaviour reinforces the assumption that the training process of a GAN is not directly comparable to a simple ML approach using a single neural network. The MAE values also fluctuate strongly over the entire training, which indicates that it is very difficult for the GAN to achieve stability in the generation, which raises the question of whether the selected best five epochs can generate high-quality GC or whether only random GCs are generated that are identified as acceptable GCs by the 1D-CNN.
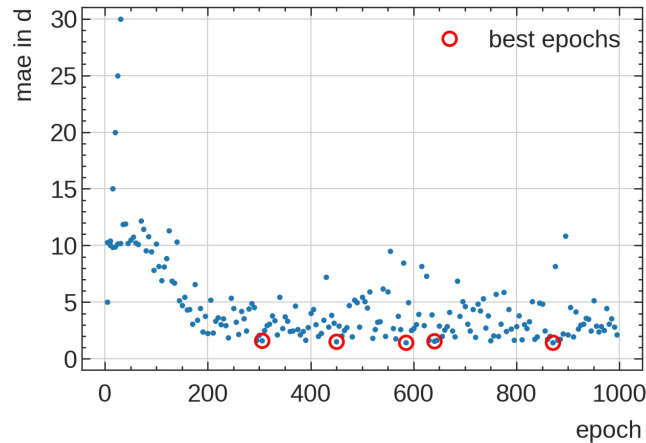
Figure 6.4: Shown is the MAE, calculated from the difference between the predicted and the actual irradiation day of the generated GC of all irradiation days per epoch. The five epochs with the minimum MAE values are marked with red circles.

Figure 6.5 shows the averaged predictions with their 68% confidence interval as a function of the true irradiation time t_{true} for the two best training epochs (585 and 870). Each averaged prediction results from the prediction of 150 generated GCs for each irradiation day. The light grey area depicts the uncertainty band of the 1D-CNN. Both epochs show that for early irradiation days ($t_{\text{pre}} = 0 - 5\,\text{d}$), the prediction deviates most strongly from the true value and even partly no longer agrees within the uncertainty band of the 1D-CNN. Irradiation days between $t_{\text{pre}} = 8 - 31\,\text{d}$ show the smallest deviations from the true irradiation day, but slight scattering depending on the irradiation day can also be seen here. The prediction seems to become less stable for late irradiation days ($t_{\text{pre}} = 35 - 38\,\text{d}$), as indicated by the differences of the predictions between epochs.
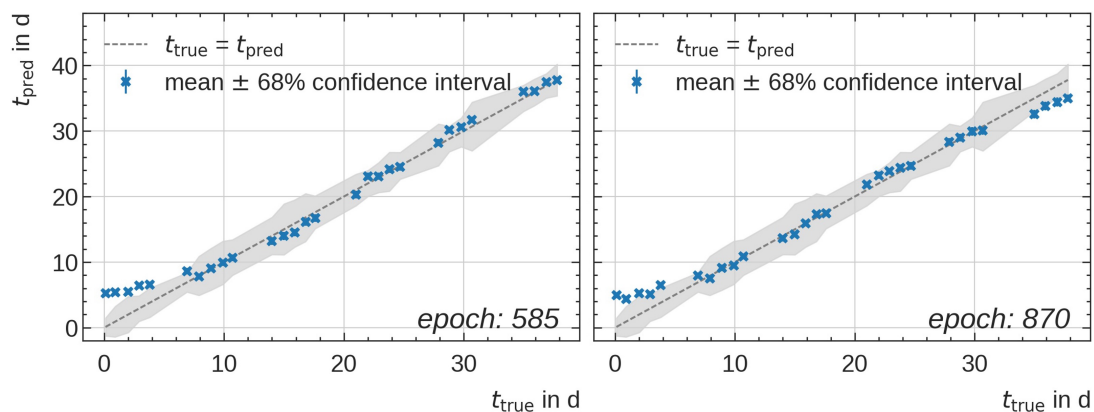
Figure 6.5: Averaged predicted t_{pre} for each irradiation day with its standard error as a function of the true t_{pre} for the generated glow curves of training epoch 585 (left) and 870 (right) are shown using the 1D-CNN model.

These variations in the prediction values depending on the best epochs make it difficult to select the final epoch for the GC generation. The MAE value alone does not show any difference in the epoch's performance, nor do the individual predictions per irradiation day and epoch simplify the choice. No matter the final epoch choice, GC cannot be generated with the same quality for all irradiation days using the same training epoch. In particular, generating good GC for the early irradiation days is generally not realisable because the GC basis has very high variations in the GC shape per irradiation day, resulting in a highly dimensioned parameter space that the GAN cannot cover in this form.

Comparing the generated GCs of epoch 585 and the measured GCs, it would be expected that the averaged GCs of both groups for the individual irradiation days would be very similar, as the 1D-CNN also identified them as such. However, this assumption does not agree with the comparison observation; see Figure 6.6. For $t_{\text{pre}} = 2\,\text{d}$, the averaged GC agree rather well, although the irradiation day predicted by the 1D-CNN deviates strongly from the true value. In contrast, at $t_{\text{pre}} = 14\,\text{d}$, where a small deviation in the prediction was achieved, the two GCs are not very similar. It seems that the distributions are only compatible for $t_{\text{pre}} = 22\,\text{d}$, even though here, too, only the course of the GC is comparable, while the uncertainty bands differ more strongly again. The same is true for $t_{\text{pre}} = 30.7\,\text{d}$, similarities can be seen in the course of the GC, but here too, the uncertainties show clear differences.

This observation thus casts doubt on the credibility of the generated GC. Due to the high variation of the measured GC, there is currently no other way to check the quality of the generated GC. It is assumed that although GCs are generated, they are not credible enough to be considered as training data for further studies. The GAN cannot generate credible GC due to the high-dimensioned parameter space and the additional condition. The question arises whether the approach of a generative model is suitable for describing such a highly complex problem. To reduce the GC generation's complexity and test whether a GAN can generate GCs, a separate GAN is trained for each irradiation day.

6.3 Single GANs

Since in data set 1, each irradiation day has only 150 GC, and this training data is insufficient to train a GAN, the number of GC per irradiation day is extended to 6000 GCs by the positional shifting of the GC as described in Section 4.4. This number is nevertheless comparatively very low but sufficient for the first test purposes. The GAN architecture remains the same for each of the 28 individual GANs.

After every GAN has been trained for 1000 epochs, the generated GC are checked
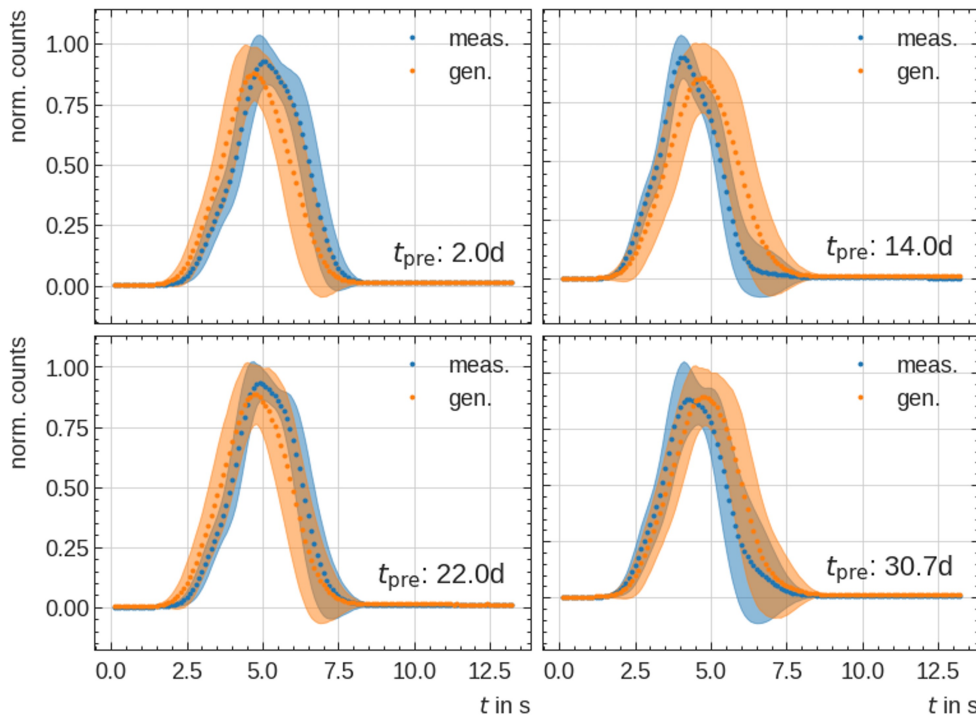
Figure 6.6: Comparison between averaged measured (blue) and generated (orange) glow curves with associated uncertainty band at different irradiation days $t_{\mathrm{pre}} = [2, 14, 22, 30.7]\,\mathrm{d}$. The glow curves are generated using the best epoch 585 of the GAN.

for quality. Figure 6.7 (left) shows an example of the training process for one of the GANs using the Wasserstein loss function for the generator and discriminator. The figure shows that both networks stabilise and converge during the training, and the discriminator converges comparatively quickly, whereas the generator takes somewhat longer to stabilise. As previously suspected, the discriminator accuracy also shows in Figure 6.7 (right) that the accuracy saturates comparatively quickly, not at $50\,\%$ but on average at $60\,\%$, which indicates that the discriminator cannot yet be completely deceived.
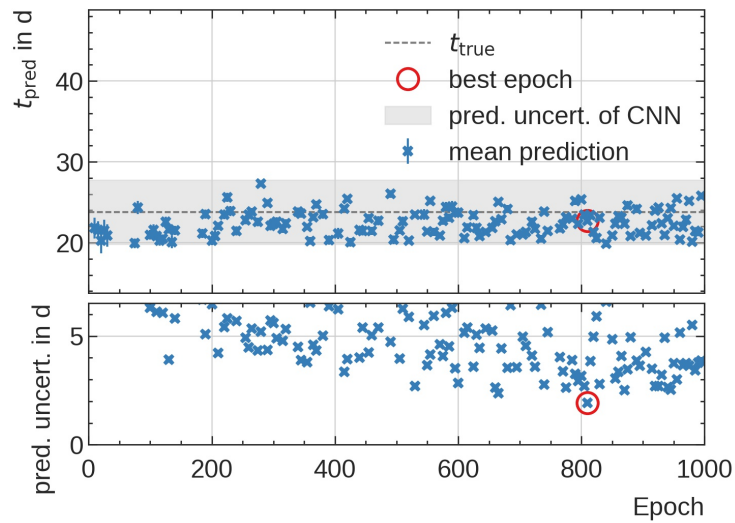
Again, the best training epoch is selected using the 1D-CNN. Since each irradiation day has a slightly different prediction uncertainty, this is also considered in evaluating the generated GC. For this purpose, 150 glow curves are generated for every tenth training epoch from each GAN, whose irradiation day is then determined by the 1D-CNN.

Figure 6.8 shows the mean predicted irradiation day and the uncertainty on the prediction as a function of the training epoch, exemplarily for the irradiation day $t_{\mathrm{pre}} = 23.8\,\mathrm{d}$. In addition, the uncertainty band of the 1D-CNN for this irradiation day is shown in grey. Predictions that exceed this error band are neglected for further consideration. The lower plot of the figure shows the $68\,\%$ interval of the difference between the true
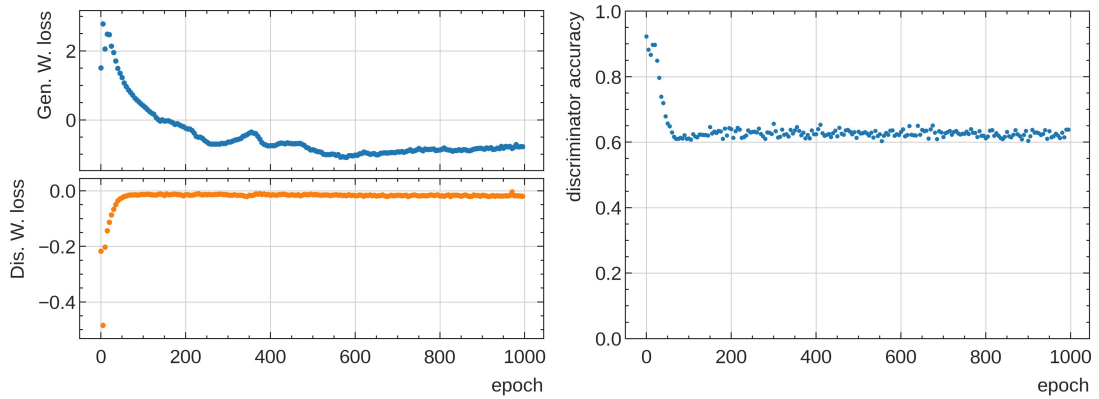
Figure 6.7: Example of the training process for the GAN to generate glow curves at the irradiation time T = 23d. Left: The course of the Wasserstein loss function for the generator and discriminator is shown. The discriminator shows rapid saturation around 0, whereas the generator requires more training epochs to converge. Right: The curve of the discriminator accuracy is shown as a function of the training epoch with saturation around 60 %.

and the predicted irradiation day, as already shown in the evaluation of the 1D-CNN for the irradiation day prediction. It can be seen that the uncertainties are in a range between 2 and 6 days.

Figure 6.8: Selection of the best training epoch using the MAE of the difference between the predicted value and the true irradiation day for all training epochs, exemplified for the generation of GC at irradiation day $t_{\mathrm{pre}} = 23.8\,\mathrm{d}$. The lower plot shows the 68 % uncertainty on the prediction deviation from the true value. A red circle marks the best epoch at 810.

In order to determine the best epoch, five epochs with the smallest deviation between the prediction and the true irradiation day are selected. Then the epoch with the smallest prediction uncertainty is selected from these epochs. This epoch is marked with a red

circle in Figure 6.8. This procedure is performed for all GANs to determine the best training epoch.

The best epoch for the GAN at the irradiation day $t_{pre} = 23.8\,\mathrm{d}$ is 810. Figure 6.9 (left) shows 50 generated GC for this epoch. Since a comparison with individual measured GCs is not meaningful due to the high variations in the measured GCs, the averaged GCs with their error band are compared instead, shown in Figure 6.9 (right). The averaged curve and the error bands of the generated GC agree well with the measured ones. Thus, the generated glow curves reproduce the measured ones well and can be used in the next step as training data for the irradiation day prediction.
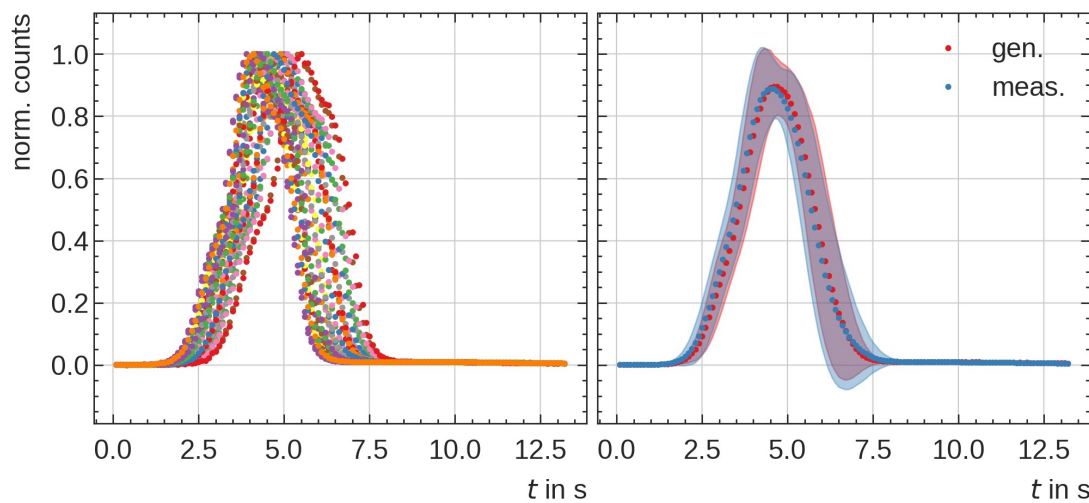
Figure 6.9: Representation of the generated GC for $t_{pre} = 23.8\,\mathrm{d}$ using the best training epoch 810. Left: 50 generated glow curves. Right: Comparison between the generated (red) average glow curve and the measured (blue) average glow curve. Both distributions show a very good agreement of the shape of the GC itself and the uncertainty bands.

Figure 6.10 shows the final evaluation of the generated GCs of the individual GANs for the best epoch in each case. The mean irradiation day predictions of the 1D-CNN with the prediction uncertainty are shown in each case. An epoch could be determined for each GAN that generates GCs corresponding to the respective irradiation day with low uncertainty. All mean values are within the error band of the 1D-CNN. However, individual irradiation days have slightly higher uncertainties than the error band, which can be attributed to the statistical variation within the measured and generated GC.

Comparing the predictions of the 1D-CNN of the generation utilising the individual GAN, a considerable improvement towards early and late irradiation days can be seen. This proves that the complexity of the problem is a major obstacle for a single GAN. However, if the problem is now split up, generating GC using a generative approach is quite possible.
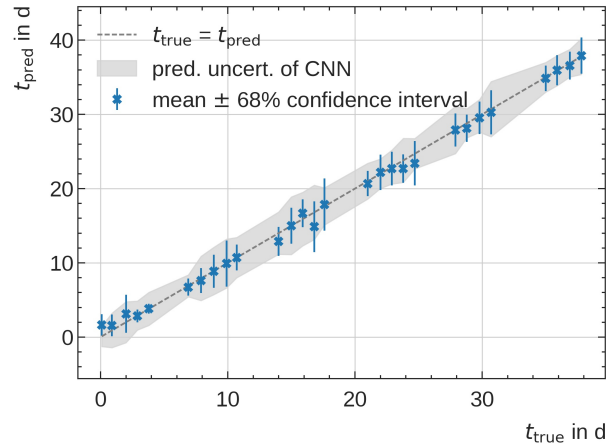
Figure 6.10: Averaged predicted t_{pre} for each irradiation day with its standard error as a function of the true t_{pre} of each GAN is shown using the 1D-CNN model.
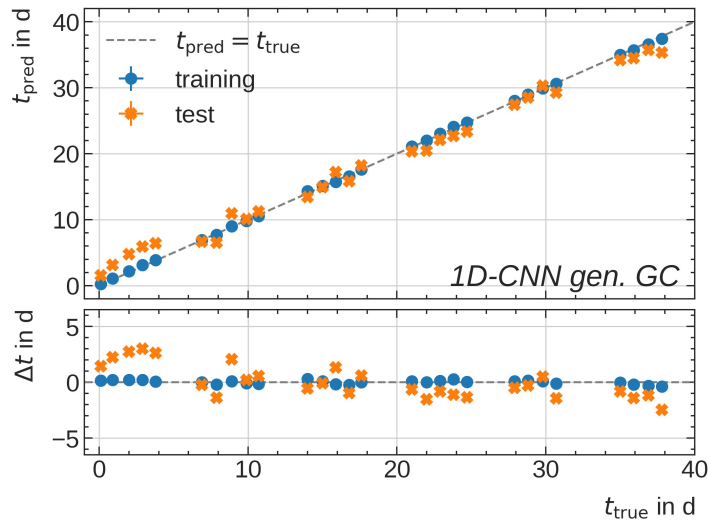
6.4 Testing Generated Glow Curves as Training Data for 1D-CNN

Since we can now generate representative GCs, these are tested for their usability as training data for the 1D-CNN. It has already been shown in Section 5.3.6 that the use of augmented data has a considerable influence on the prediction accuracy of the 1D-CNN. The measured training data are augmented with generated GC to 20k GC to reproduce this condition. The 1D-CNN then undergoes a training process on this training data and is finally evaluated with the help of the independent test data set, including only measured GCs.

Figure 6.11 shows the averaged predictions on the training and test data set. It can be seen that the predictions of the training data agree very well with the true values; there are hardly any deviations. Considering the generalisation using the independent test data, deviations in the prediction to the true irradiation days can be seen, especially for early irradiation days. Over the entire irradiation interval, not all predictions between training and test data agree. Discrepancies of up to three days for the test data set indicate that the 1D-CNN may be somewhat over-trained on the training data and, thus, not fully generalisable to independent data. Nevertheless, the generated data set does not affect the prediction accuracy.

Comparing the prediction uncertainties of all the training data considered for the 1D-CNN, it is shown that the prediction uncertainty does not improve using the generated GC and the measured data set, see Figure 6.12. It is shown that the improvement compared to training only on the measured training data set varies on average by 5 % for all irradiation days. For individual irradiation days, an improvement of about $10 - 20$ %

is achieved, but this is not sufficient to speak of a general improvement, as for some irradiation days, the prediction accuracy even seems to deteriorate up to 30 %.

Figure 6.11: Averaged predicted t_{pre} for each irradiation day with its standard error as a function of the true t_{pre} for the training (blue) and test (orange) data set using generated glow curves as training data is shown using the 1D-CNN model. The bottom plot displays the deviation between the predicted and the true t_{pre}.
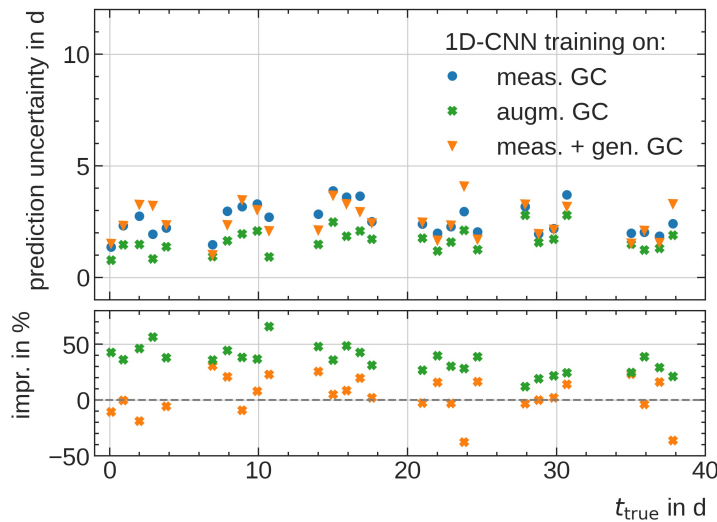
Figure 6.12: Comparison of prediction uncertainties for t_{pre} of the 1D-CNN approach trained on the measured, augmented and generated training data.

This finding indicates that the application of a conditional GAN allows for the generation of GCs. However, a single GAN cannot generate GCs corresponding to different irradiation days due to the significant variation observed among GCs for each specific

irradiation day. This high variation prevents effective learning by a single GAN model. By employing separate GAN models for individual irradiation days, successful generation of GCs representative of each irradiation day is achieved. The 1D-CNN can assign the generated GCs to their respective irradiation days within the uncertainty range of the 1D-CNN.

Nevertheless, using the generated GCs as additional training data for the 1D-CNN does not enhance the prediction accuracy compared to training solely on measured data. Consequently, the generated GCs do not provide any supplementary information that improves the performance of the 1D-CNN. Thus, while the GAN can map relevant features from the measured GCs, it does not interpolate additional features within the GC parameter space that are beneficial for irradiation day prediction.

Summary & Outlook

This work implements deep learning techniques like DNN and CNN to estimate the irradiation day of TL dosimeters. It focuses on single-dose irradiations with a Cs-137 source within a 40-day monitoring interval. The first proof-of-concept study uses 554 non-tempered GCs with an irradiation dose of $10\,\mathrm{mGy}$ as training data. The DNN-based approach using extracted GC parameters achieves a prediction uncertainty of $\overline{\sigma}_{\mathrm{DNN,\ non\text{-}temp.}} = (3.8 \pm 0.7)\,\mathrm{d}$. Using the entire GC shape as input for a CNN reduces the prediction uncertainty to $\overline{\sigma}_{\mathrm{CNN,\ non\text{-}temp.}} = (1.6 \pm 0.1)\,\mathrm{d}$.

Next, 4200 pre-tempered GCs replace the training data set. These GCs experience the complete readout process, including pre-heating to eliminate thermal fading. This step is essential in the routine dosimetry operation of the MPA NRW to ensure an accurate dose estimate for all monitored persons. The extracted GC parameters of pre-tempered GCs show little dependence on the irradiation day. However, the DNN trained on these GC parameters achieves a predictive uncertainty of $\overline{\sigma}_{\mathrm{DNN,\ pre\text{-}temp.}} = (4.9 \pm 1.4)\,\mathrm{d}$, representing a one-day deterioration compared to non-tempered data set.

Using Shapley values [62] enables the description of feature importance and, consequently, the model's relevance in predicting the irradiation day. The feature interpretation reveals that certain extracted GC parameters do not substantially impact the ultimate irradiation day prediction. As a result, they can be eliminated from the training data set without compromising the model's performance.

The CNN trained on non-tempered data shows that knowledge-based feature extraction is unnecessary for accurate irradiation day prediction. Shapley values identify relevant regions within a two-dimensional GC for irradiation day prediction. The chosen colours represent the importance and the direction in which the irradiation day prediction is guided (blue: shift towards earlier irradiation days, red: shift towards later irradiation days). The significance of the GC areas depicted in the two-dimensional GC aligns with the importance of the extracted GC parameters. This finding substantiates that the CNN can acquire relevant features within the GC, rendering extracted knowledge-based features unnecessary for predicting the irradiation day. The CNN achieves a prediction uncertainty of $\overline{\sigma}_{\mathrm{1D\text{-}CNN,\ pre\text{-}temp.}} = (2.5 \pm 0.6)\,\mathrm{d}$, considering the high variation of GC shapes.

CNN's performance improves with augmented data, highlighting the importance of a

large data set for training deep learning models. Training the CNN on 20k augmented GC data set yields a prediction uncertainty of $\overline{\sigma}_{\text{1D-CNN, augm.}} = (1.6 \pm 0.5)\,\text{d}$, comparable to the non-tempered data set. The ability to narrow down the incident period and reconstruct its cause enhances radiation protection measures and safety for monitored individuals. The DNN and CNN approaches are also tested on a data set with different irradiation doses $(0.3 - 8\,\text{mGy})$. This reveals a dose-dependent prediction uncertainty due to the signal-to-noise ratio towards lower doses. GC pre-processing techniques need to be studied and adjusted to improve the irradiation day prediction for irradiation with low doses. Smoothing filters like the Savitzky-Golay [51] filter can enhance GC shape extraction. Future integration of dose information during training can enable dose estimation alongside irradiation day prediction.

The successful implementation of the CNN for irradiation day prediction presents new opportunities for various applications, including distinguishing between single and multiple irradiations. Moreover, future investigations can explore the capability of CNN in discerning different types of radiation, such as differentiating the proportion of photons and alpha particles for neutron dosimetry. Currently, neutron dosimetry requires using two detectors to assess the neutron dose. Achieving neutron measurement with a single detector would represent a significant breakthrough in this field.

In the final section of this work, a conditional WGAN incorporating a gradient penalty was employed to generate GCs for various irradiation days based on measured GCs. However, a single GAN was insufficient to capture the wide variation of GCs within each irradiation day. Consequently, individual GAN models were trained for each specific irradiation day, successfully generating GCs representative of the respective irradiation day. Integrating these generated GCs into the CNN training data set did not improve the irradiation day prediction accuracy, as they mainly reflected the learned features from the measured GCs.

Future research can focus on expanding the GAN model in terms of architecture and hyperparameters to enable the generation of GCs for various irradiation days using a single GAN. This would also facilitate the generation of GCs for irradiation days not represented within the measured data set. However, such implementation necessitates a significantly larger data set to represent the GC parameter space better. Additional measurement campaigns are therefore required to achieve this objective. Furthermore, the conditional input of the GAN can be extended beyond irradiation day to incorporate other factors, such as irradiation dose, enabling the generation of GCs for different irradiation doses as well.

Bibliography

[1]   Barbara Marinacci. **Linus Pauling in His Own Words: Selections from His Writings, Speeches and Interviews**. Touchstone, 1995.

[2]   Bundesministerium der Justiz. **Gesetz zum Schutz vor der schädlichen Wirkung ionisierender Strahlung**. 2022. URL: https://www.gesetze-im-internet.de/strlschg/ (visited on 03/11/2023).

[3]   E. Fantuzzi, J. G. Alves, P. Ambrosi, H. Janzekovic, and E. Vartiainen. **Implementation of standards for individual monitoring in Europe**. *Radiation Protection Dosimetry* 112:1 (2004), 3–44.

[4]   EUROPEAN COMMISSION, FOOD, AGRICULTURE ORGANIZATION OF THE UNITED NATIONS, INTERNATIONAL ATOMIC ENERGY AGENCY, INTERNATIONAL LABOUR ORGANIZATION, OECD NUCLEAR ENERGY AGENCY, PAN AMERICAN HEALTH ORGANIZATION, UNITED NATIONS ENVIRONMENT PROGRAMME, and WORLD HEALTH ORGANIZATION. **Radiation Protection and Safety of Radiation Sources: International Basic Safety Standards**. General Safety Requirements GSR Part 3. INTERNATIONAL ATOMIC ENERGY AGENCY, 2014.

[5]   D.T. Bartlett (INVITED). **Electronic Dosemeters: Use in Personal Dosimetry**. *Radiation Protection Dosimetry* 47:1-4 (1993), 335–339. DOI: 10.1093/oxfordjournals.rpd.a081763.

[6]   Naturschutz und Reaktorsicherheit Bundesministerium für Umwelt. **Messung der Personendosis mit elektronischen Personendosimetern in gepulsten Feldern - Rundschreiben des BMU vom 06.10.2008 - RS II 3 – 15530/2**. 2022. URL: https://www.verwaltungsvorschriften-im-internet.de/bsvwvbund_06102008_RSII3155302.htm (visited on 06/01/2023).

[7]   INTERNATIONAL ATOMIC ENERGY AGENCY. **Occupational Radiation Protection**. General Safety Guides GSG-7. INTERNATIONAL ATOMIC ENERGY AGENCY, 2018.

[8]   F. Mihai, S. Bercea, A. Stochioiu, A. Celarel, E. Udup, and I. Tudor. **Low and high dose measurement by Agfa personal monitoring film and FD-III-B badge dosimeter system**. *Applied Radiation and Isotopes* 68:4 (2010), 614–616.

[9]   E. G. Yukihara and S. W. S. McKeever. **Optically stimulated luminescence (OSL) dosimetry in medicine**. *Physics in Medicine & Biology* 53:20 (2008), R351. DOI: 10.1088/0031-9155/53/20/R01.

[10]   T. Kron, P. Lonski, and E. G. Yukihara. **THERMOLUMINESCENCE DOSIMETRY (TLD) IN MEDICINE: FIVE 'W'S AND ONE HOW**. *Radiation Protection Dosimetry* 192:2 (2021), 139–151. DOI: 10.1093/rpd/ncaa212.

[11]   J. T. Randall and M. H. F. Wilkins. **Phosphorescence and Electron Traps. I. The Study of Trap Distributions**. *Proceedings of the Royal Society of London. Series A, Mathematical and Physical Sciences* 184, No. 999 (1945), 365–389.

[12]   Materialprüfungsamt Nordrhein-Westfalen. **Dosimeter und Auswertung**. 2023. URL: https://www.mpanrw.de/dienstleistungen/strahlenschutz/dosimetrie-angebot (visited on 06/01/2023).

[13]   R. Theinert. **Estimation of fading time and irradiation dose in thermoluminescence dosimetry using uni- and multivariate analysis techniques**. Dissertation. TU Dortmund University, 2018. DOI: 10.17877/DE290R-19345.

[14]   R. Theinert, K. Kröninger, A. Lütfring, and J. Walbersloh. **Computational analysis of thermoluminescence glow curves from thin layer dosemeters**. *Radiation Measurements* 106 (2017), 252–256. DOI: 10.1016/j.radmeas.2017.05.002.

[15]   R. Theinert, K. Kröninger, A. Lütfring, S. Mender, F. Mentzel, and J. Walbersloh. **Fading time and irradiation dose estimation from thermoluminescent dosemeters using glow curve deconvolution**. *Radiation Measurements* 108 (2018), 20–25. DOI: 10.1016/j.radmeas.2017.11.002.

[16]   F. Mentzel, K. Kröninger, L. Röhrig, L. Speicher, M-L. Steil, R. Theinert, and J. Walbersloh. **Extending information relevant for personal dose monitoring obtained from glow curves of thermoluminescence dosimeters using artificial neural networks**. *Radiat. Meas.* 136:106375 (2020). DOI: 10.1016/j.radmeas.2020.106375.

[17]   F. Mentzel, E. Derugin, H. Jansen, K. Kröninger, O. Nackenhorst, J. Walbersloh, and J. Weingarten. **No more glowing in the dark: how deep learning improves exposure date estimation in thermoluminescence dosimetry**. *Journal of Radiological Protection* 41:4 (2021), S506. DOI: 10.1088/1361-6498/ac20ae.

[18]   E. Derugin, K. Kröninger, F. Mentzel, O. Nackenhorst, J. Walbersloh, and J. Weingarten. **Deep TL: progress of a machine learning aided personal dose monitoring system**. *Radiation Protection Dosimetry* 199:8-9 (2023), 767–774. DOI: 10.1093/rpd/ncad078.

[19]   Bundesamt für Strahlenschutz. **Beruflicher Strahlenschutz**. URL: https://www.bfs.de/DE/themen/ion/strahlenschutz/beruf/beruf_node.html (visited on 03/11/2023).

[20]   A. F. McKlinley. **Thermoluminescence dosimetry**. Medical Physics Handbooks 5. Adam Hilger Ltd., 1981.

[21]   Materialprüfungsamt Nordrhein-Westfalen. **Strahlenschutz**. URL: https://www.mpanrw.de/dienstleistungen/strahlenschutz (visited on 03/11/2023).

[22]   Bundesministerium der Justiz. **Verordnung zum Schutz vor der schädlichen Wirkung ionisierender Strahlung**. 2021. URL: http://www.gesetze-im-internet.de/strlschv_2018/ (visited on 03/01/2023).

[23]   J. E. Martin. **Physics for Radiation Protection, Third Edition**. Wiley-VCH Verlag GmbH & Co. KGaA, 2013. DOI: 10.1002/9783527667062.

[24]   R. D. Evans. **Atomic Nucleus**. Krieger, 1982.

[25]   M.J. Berger et. al. **XCOM: Photon Cross Sections Database Share**. URL: https://www.nist.gov/pml/xcom-photon-cross-sections-database (visited on 03/11/2023).

[26]   International Commission on Radiation Units Measurements (ICRU). **ICRU Report 51, Quantities and Units in Radiation Protection Dosimetry**. ICRU, 1993.

[27]   International Commission on Radiological Protection (ICRP). **The 2007 Recommendations of the International Commission on Radiological Protection**. ICRP, 2007.

[28]   F. Daniels, C. A. Boyd, and D. F. Saunders. **Thermoluminescence as a Research Tool**. *Science* 117:3040 (1953), 343–349. DOI: 10.1126/science.117.3040.343.

[29]   S. W. S. McKeever. **Thermoluminescence of Solids**. Cambridge Solid State Science Series. Cambridge University Press, 1985.

[30]   S. Samarin, O.M. Artamonov, A.A. Suvorova, A.D. Sergeant, and J.F. Williams. **Measurements of insulator band parameters using combination of single-electron and two-electron spectroscopy**. *Solid State Communications* 129:6 (2004), 389–393. DOI: 10.1016/j.ssc.2003.11.008.

[31]   J. Walbersloh and F. Busch. **A THIN-LAYER LIF THERMOLUMINESCENCE DOSEMETER SYSTEM WITH FAST READOUT FOR THE USE IN PERSONAL DOSIMETRY SERVICES**. *Radiation Protection Dosimetry* 170:1-4 (2016), 191–194. ISSN: 0144-8420. DOI: 10.1093/rpd/ncv478.

[32]   Materialprüfungsamt NRW. **Personendosimeter MPA TL-DOS GD 01 - Technisches Datenblatt—Stand 01.12.2022**. URL: https://www.mpanrw.de/downloads/informationsportal-der-personendosis-messstelle (visited on 03/11/2023).

[33]   Y. Lee, Y. Won, and K. Kang. **A method to minimise the fading effects of LiF:Mg,Ti (TLD-600 and TLD-700) using a pre-heat technique**. *Radiation protection dosimetry* 164:3 (2015), 449–455. DOI: 10.1093/rpd/ncu302.

[34]   F. Mentzel. **Empirical Simulation of Glowcurves for Multivariate Analysis in the TL-DOS Project**. Master Thesis. TU Dortmund University, 2018.

[35]   H. Jansen. **Studies on irradiation date estimation using measured and simulated high-statistics glow curve data sets**. Master Thesis. TU Dortmund University, 2020.

[36]   G. Kitis, J.. M Gomez-Ros, and J. W. N. Tuyn. **Thermoluminescence glow-curve deconvolution functions for first, second and general orders of kinetics**. *Journal of Physics D: Applied Physics* 31:19 (1998), 2636. DOI: 10.1088/0022-3727/31/19/037.

[37]   George C. Furettaand G. Kitis. **Models in thermoluminescence**. *Journal of Materials Science* 39 (2004), 2277–2294. DOI: 10.1023/B:JMSC.0000019989.60268.d7.

[38]   S. Druzhyna, I. Eliyahu, L. Oster, Y. S. Horowitz, S. Biderman, G. Reshes, and I. Orion. **Investigation of the optical absorption dose response of LiF:Mg,Ti (TLD-100) and the role of V centers in F center (5.08 eV) bleaching**. *Radiation Measurements* 90 (2016). DOI: 10.1016/j.radmeas.2016.02.003.

[39] I. Eliyahu, Y. S. Horowitz, L. Oster, S. Druzhyna, S. Biderman, D. Ginzburg, and G. Reshes. **Kinetic simulation of the optical absorption dose response of LiF:Mg,Ti (TLD-100) incorporating spatially correlated electron and hole trapping centers**. *Nuclear Instruments and Methods in Physics Research B* 407 (Sept. 2017), 282–290. DOI: 10.1016/j.nimb.2017.07.018.

[40] R. Chen, V. Pagonis, and J.L. Lawless. **Evaluated thermoluminescence trapping parameters–What do they really mean?** *Radiation Measurements* 91 (2016), 21–27. ISSN: 1350-4487. DOI: 10.1016/j.radmeas.2016.04.006.

[41] L. Strauss. **Review of methods for the determination of the kinetic parameters of thermoluminescence dosimeters Project thesis by L .** In: 2007.

[42] I. Eliyahu, Y.S. Horowitz, L. Oster, and I. Mardor. **A kinetic model incorporating both localized and delocalized recombination: Application to the dependence of the TL dose response on photon energy**. *Journal of Luminescence* 145 (2014), 600–607. DOI: https://doi.org/10.1016/j.jlumin.2013.08.033.

[43] T. A. J. Schneider. **Glowcurve simulation using rate equations**. Master Thesis. TU Dortmund University, 2021.

[44] M. Rempe. **Glowcurve simulation using conditional generative adversarial networks**. Bachelor Thesis. TU Dortmund University, 2020.

[45] LNHB. **Nucléide - Lara**. 2023. URL: http://www.lnhb.fr/Laraweb/index.php (visited on 03/01/2023).

[46] M. Özdemir. **Studie zur Kalibrierung von TL-DOS Detektoren im Auslesemagazin**. Bachelor Thesis. TU Dortmund University, 2022.

[47] J. Egert. **Charakterisierung des optimierten optischen Messkopfes eines Auswerteautomaten für Dünnschicht- Thermolumineszenzdosimeter**. Bachelor Thesis. TU Dortmund University, 2014.

[48] A. Lütfring. **Charakterisierung des Aufheizverhaltens und glühkurvenbasierte Rekonstruktion der Detektortemperatur eines Dünnschicht-Thermolumineszenzdosimeters**. Master Thesis. TU Dortmund University, 2016.

[49] O. Lynnyk. **Untersuchung der Temperaturabhängigkeit von Pre- und Post-Irradiation-Fading bei Thermolumineszenzdosimetern**. Bachelor Thesis. TU Dortmund University, 2018.

[50] H. Rotgeri. **Auswirkungen des Ausheizprofils auf die Glühkurvenform von Thermolumineszenzdosimetern**. Bachelor Thesis. TU Dortmund University, 2019.

[51] A. Savitzky and M. J. E. Golay. **Smoothing and Differentiation of Data by Simplified Least Squares Procedures**. *Anal. Chem.* 36:8 (1964), 1627–1639. DOI: 10.1021/ac60214a047.

[52] C. M. Bishop. **Pattern Recognition and Machine Learning (Information Science and Statistics)**. Springer-Verlag, 2006.

[53] T. Hastie, R. Tibshirani, and J. Friedman. **The Elements of Statistical Learning - Data Mining, Inference, and Prediction, Second Edition**. Springer Series in Statistics Springer, 2009.

[54] M. Kubat. **An Introduction to Machine Learning**. Springer International Publishing, 2017.

[55] A. F. Agarap. **Deep Learning using Rectified Linear Units (ReLU)**. 2019. arXiv: 1803.08375 `[cs.NE]`.

[56] X. Glorot, A. Bordes, and Y. Bengio. **Deep Sparse Rectifier Neural Networks**. In: *Proceedings of the Fourteenth International Conference on Artificial Intelligence and Statistics*. Ed. by Geoffrey Gordon, David Dunson, and Miroslav Dudík. Vol. 15. Proceedings of Machine Learning Research. PMLR, 2011, 315–323.

[57] B. Xu, N. Wang, T. Chen, and M. Li. **Empirical Evaluation of Rectified Activations in Convolutional Network**. 2015. arXiv: 1505.00853 `[cs.LG]`.

[58] D. P. Kingma and J. Ba. **Adam: A Method for Stochastic Optimization**. 2017. arXiv: 1412.6980 `[cs.LG]`.

[59] A. Y. Ng. **Feature Selection, L1 vs. L2 Regularization, and Rotational Invariance**. In: *Proceedings of the Twenty-First International Conference on Machine Learning*. ICML '04. Association for Computing Machinery, 2004, 78. DOI: 10.1145/1015330.1015435.

[60] B. W. Silverman. **Density Estimation for Statistics and Data Analysis**. Chapman & Hall, 1986.

[61] N. Srivastava, G. Hinton, A. Krizhevsky, I. Sutskever, and R. Salakhutdinov. **Dropout: A Simple Way to Prevent Neural Networks from Overfitting**. *Journal of Machine Learning Research* 15:56 (2014), 1929–1958.

[62] L. Shapley, 69–79. In: *Classics in Game Theory*. Ed. by Harold William Kuhn. Princeton University Press, 1997. DOI: 10.1515/9781400829156-012.

[63] C. Rudin. **Stop explaining black box machine learning models for high stakes decisions and use interpretable models instead**. *Nature Machine Intelligence* 1:5 (2019), 206–215. DOI: 10.1038/s42256-019-0048-x.

[64] D. Slack, S. A. Friedler, C. Scheidegger, and C. Dutta Roy. **Assessing the Local Interpretability of Machine Learning Models**. 2019. arXiv: 1902.03501 `[cs.LG]`.

[65] S. M. Lundberg and S-I. Lee. **A Unified Approach to Interpreting Model Predictions**. In: *Advances in Neural Information Processing Systems*. Ed. by I. Guyon, U. Von Luxburg, S. Bengio, H. Wallach, R. Fergus, S. Vishwanathan, and R. Garnett. Vol. 30. Curran Associates, Inc., 2017.

[66] E. Štrumbelj and I. Kononenko. **Explaining prediction models and individual predictions with feature contributions**. *Knowledge and Information Systems* 41:3 (2014), 647–665. DOI: 10.1007/s10115-013-0679-x.

[67] S. M. Lundberg, G. G. Erion, and S-I. Lee. **Consistent Individualized Feature Attribution for Tree Ensembles**. 2019. arXiv: 1802.03888 `[cs.LG]`.

[68]   M. Ancona, C. Öztireli, and M. Gross. **Explaining Deep Neural Networks with a Polynomial Time Algorithm for Shapley Values Approximation**. 2019. arXiv: 1903.10992 [cs.LG].

[69]   H. P. Young. **Monotonic solutions of cooperative games**. *International Journal of Game Theory* 14:2 (1985), 65–72. DOI: 10.1007/BF01769885.

[70]   S. M. Lundberg. **SHAP**. 45b85c18. 2018. URL: https://shap.readthedocs.io/en/latest/.

[71]   L. Breiman. **Random Forests**. *Machine Learning* 45:1 (2001), 5–32. DOI: 10.1023/A: 1010933404324.

[72]   I. Goodfellow, J. Pouget-Abadie, M. Mirza, B. Xu, D. Warde-Farley, S. Ozair, A. Courville, and Y. Bengio. **Generative Adversarial Nets**. In: *Advances in Neural Information Processing Systems*. Ed. by Z. Ghahramani, M. Welling, C. Cortes, N. Lawrence, and K.Q. Weinberger. Vol. 27. Curran Associates, Inc., 2014.

[73]   M. Mirza and S. Osindero. **Conditional Generative Adversarial Nets**. 2014. arXiv: 1411. 1784 [cs.LG].

[74]   M. Arjovsky, S. Chintala, and L. Bottou. **Wasserstein GAN**. 2017. arXiv: 1701.07875 [stat.ML].

[75]   R. L. Dobrushin. **Prescribing a System of Random Variables by Conditional Distributions**. *Theory of Probability & Its Applications* 15:3 (1970), 458–486. DOI: 10.1137/1115049.

[76]   S. Ioffe and C. Szegedy. **Batch Normalization: Accelerating Deep Network Training by Reducing Internal Covariate Shift**. 2015. arXiv: 1502.03167 [cs.LG].

[77]   I. Gulrajani, F. Ahmed, M. Arjovsky, V. Dumoulin, and A. Courville. **Improved Training of Wasserstein GANs**. 2017. arXiv: 1704.00028 [cs.LG].

[78]   S. Amari, N. Murata, K.-R. Muller, M. Finke, and H.H. Yang. **Asymptotic statistical theory of overtraining and cross-validation**. *IEEE Transactions on Neural Networks* 8:5 (1997), 985–996. DOI: 10.1109/72.623200.

[79]   Z. Zhou, J. Liang, Y. Song, L. Yu, H. Wang, W. Zhang, Y. Yu, and Z. Zhang. **Lipschitz Generative Adversarial Nets**. 2019. arXiv: 1902.05687 [cs.LG].

[80]   M. Arjovsky, S. Chintala, and L. Bottou. **Wasserstein Generative Adversarial Networks**. In: *Proceedings of the 34th International Conference on Machine Learning*. Vol. 70. Proceedings of Machine Learning Research. PMLR, 2017, 214–223.

[81]   M. Arjovsky and L. Bottou. **Towards Principled Methods for Training Generative Adversarial Networks**. 2017. arXiv: 1701.04862 [stat.ML].

[82]   F. Farnia and A. Ozdaglar. **GANs May Have No Nash Equilibria**. 2020. arXiv: 2002.09124 [cs.LG].

[83]   W. Fedus, M. Rosca, B. Lakshminarayanan, A. M. Dai, S. Mohamed, and I. Goodfellow. **Many Paths to Equilibrium: GANs Do Not Need to Decrease a Divergence At Every Step**. 2018. arXiv: 1710.08446 [stat.ML].

[84]   F. A. Oliehoek, R. Savani, J. Gallego, E. van der Pol, and R. Groß. **Beyond Local Nash Equilibria for Adversarial Networks**. In: *Artificial Intelligence*. Ed. by Martin Atzmueller and Wouter Duivesteijn. Cham: Springer International Publishing, 2019, 73–89.

Danksagung

An dieser Stelle möchte ich mich bei allen Personen bedanken, die mich in den vergangenen drei Jahren bei der Erstellung dieser Dissertation begleitet und unterstütz haben.

Großer Dank geht an Prof. Dr. Kevin Kröninger, der mir die Möglichkeit gegeben hat an diesem Projekt zu arbeiten und diese Arbeit zu verfassen. Ebenfalls geht großer Dank an Prof. Dr. Carsten Westphal für das Lesen und Bewerten meiner Arbeit.

Vielen Dank an die Deutsche Forschungsgemeinschaft (DFG) für die Förderung meiner Arbeit im Rahmen des Projektes Nr. KR 4060/10-1.

Meinen Betreuern Jens, Flo und Olaf möchte ich meinen aufrichtigsten Dank aussprechen. Durch euer Engagement und Vertrauen habt ihr mich stets inspiriert und motiviert, mein Bestes zu geben und dabei auch meine persönliche und berufliche Entwicklung gefördert. Ich bin unendlich dankbar für jede Diskussion und konstruktive Kritik, die meine Arbeit stets verbessert hat.

Ich möchte dem gesamten TL-DOS Team und insbesondere Jörg danken für den Zugang zu Messdaten und für das Durchführen der vielen Messungen. Danke, dass ich ein Teil von TL-DOS sein konnte.

Vielen Dank e4 eV! Man hätte sich keine bessere Arbeitsgruppe wünschen können. Viele witzige Erlebnisse werden immer in meiner Erinerung bleiben, besonders die zahlreichen Kuchen und Gespräche mit Andrea werden mir fehlen.

Ich möchte meinen tiefsten Dank an meine zwei Herzensmenschen Isabelle und Alina aussprechen. Eure Freundschaft hat mir in dieser Zeit enorm viel Kraft und Zuflucht gegeben.

Zuletzt danke ich meiner Familie, durch eure bedingungslose Unterstützung und Liebe seid ihr mein Rückhalt und meine größte Motivation. Ohne Euch wäre ich nicht so weit gekommen.

Danke Alex, dass du mich auf jeder Reise begleitest.